University of Rome Tor Vergata

FACULTY OF MATHEMATICAL PHYSICAL AND NATURAL SCIENCES
Department of Physics

University of Rome Sapienza

FACULTY OF MATHEMATICAL PHYSICAL AND NATURAL SCIENCES
Department of Physics

PHD IN ASTRONOMY, ASTROPHYSICS AND SPACE SCIENCE

Halo Model for Cosmic Shear Predictions

PHD Candidate:

Sandra Di Meo

Supervisors:

Prof. Pasquale Mazzotta
Prof. Massimo Meneghetti
Dott. Carlo Giocoli

Coordinator:

Prof. Pasquale Mazzotta

a.y. 2015/2016

XXVIII cicle

Headmaster: *All right, settle down, settle down. [He puts his papers down.] Now before I begin the lesson will those of you who are playing in the match this afternoon move your clothes down on to the lower peg immediately after lunch before you write your letter home, if you're not getting your hair cut, unless you've got a younger brother who is going out this weekend as the guest of another boy, in which case collect his note before lunch, put it in your letter after you've had your hair cut, and make sure he moves your clothes down onto the lower peg for you. Now...*

Wymer: *Sir?*

Headmaster: *Yes, Wymer?*

Wymer: *My younger brother's going out with Dibble this weekend, sir, but I'm not having my hair cut today sir, so do I move my clothes down or...*

Headmaster: *I do wish you'd listen, Wymer, it's perfectly simple. If you're not getting your hair cut, you don't have to move your brother's clothes down to the lower peg, you simply collect his note before lunch after you've done your scripture prep when you've written your letter home before rest, move your own clothes on to the lower peg, greet the visitors, and report to Mr Viney that you've had your chit signed.*

Monty Python - The meaning of life

Contents

Abstract

The thesis we present is a numerical study of the lensing properties of the large scale structures.

The current theory of structure formation assumes that it forms via gravitational instability from initial perturbations in the density field. As the Universe cooled, clumps of dark matter began to condense. Gas and dark matter were gravitationally attracted to the higher density areas and formed the seeds for the primordial celestial objects. This scenario is called top-bottom or hierarchical scenario, because the smaller objects are the first to be assembled, then they merge to give origin to the large scale structure, (Coles and Lucchin, 2002).

At present time the LSS shows up in a cosmic web, in which galaxy clusters occupy the nodes and are connected by filaments of matter, and in between there are the voids, (Einasto, 2012; Coil, 2013). Being the most bound and latest forming structures, clusters can be used as an ideal laboratory to test the prediction of the ΛCDM model, (Davis et al., 1985; Hung et al., 2016). In particular, since clusters are dominated by dark matter, we can use them to investigate the properties of dark matter too (Kunz et al., 2016).

Because the dark matter interacts only with gravity, it is not possible to trace it directly, as we can do when we observe the hot gas bremsstrahlung emission in X-ray band (Bahcall and Sarazin, 1977; Sarazin, 1986) and the light coming from galaxies in the optical band (Zwicky, 1937; Munari et al., 2013). To detect dark matter we need to recognize its gravitational effects on the images of background galaxies, (Bacon et al., 2000; Refregier, 2003).

In fact the gravitational field produced by massive objects extends far into the space-time and, deforming it, it is able to bend light rays passing close to the objects and to refocus them somewhere else. This produces a pattern of distortions in size and shape of the images. The effect of deflection of light

by gravity is called gravitational lensing and the objects responsible of it are called gravitational lenses, (Narayan and Bartelmann, 1996).
In the near future several new large scale surveys, like the Large Synoptic Survey Telescope (LSST, LSST Science Collaboration et al., 2009) and EUCLID (Refregier et al., 2010, Laureijs et al., 2011) are including among their goals the measurements of weak lensing.

The main purpose of this work is to determine the effects of cosmic shear due to the dark matter distribution in the LSS produced on the background galaxies, by understanding how and how much its convergence field changes, changing the model used to describe the density field.

In order to represent the LSS, to estimate its lensing properties and be able to compare the observations with the numerical results, we have two possible alternatives. The first one is to simulate the evolution of a piece of universe by reproducing mock light cones with cosmological simulations, but, for making a statistical analysis, a large number of realizations is needed while the N-body simulations are very expensive in terms of computational time and space, or we can treat the LSS as an ensemble of dark matter clumps, with a given density profile and a cosmologically consistent distribution, compatibly with the halo-model idea, (Cooray and Sheth, 2002).
We proceeded by choosing the second approach. Then, our work is mainly based on the developing of Weak Lensing-Matter density distributiOn Kode for grAvitational lenses (WL-MOKA), a semi-analytical tool, which is able, given a three-dimensional distribution of dark matter halos, to create the surface density distribution of each spherical halo and then to calculate the convergence fields. This code respect to N-body simulations is very fast, so to test its limits and fine tune it, we took the available halo catalogues extracted from the COupled Dark Energy Cosmological Simulations (CoDECS) project, in particular the ΛCDM simulation, implemented with the parallel TREEPM-SPH N-body code GADGET (Springel, 2005) by Baldi (2012b), in which, they added the physical effect due to the interaction between the cold dark matter fluid and the dark energy scalar field.
Starting from the outputs of simulation, we created mock light cones filled with halos with a given density profile and we calculated the convergence maps. At

this step we considered the extension and the density profile outside the virial radius of the halos as free parameters. Then, we proceeded into a one-point and a two-point statistical analysis by deriving the probability distribution function and the power spectrum of the convergence, and we compared our results with the same quantities extracted from the simulation. Once the best match has been determined, we continued our study by analysing the entire a set of 25 light cones of the ΛCDM simulation and we calculated the covariance maps and the cross-correlation coefficient matrices of the power spectrum. At least we compared them from those derived directly from the simulation.
We also considered another cosmological simulation, ΛCDM-HS8, with the same cosmological parameters of the ΛCDM simulation and a different value for σ_8, and we applied the previous recipe.

All these comparisons allow us both to fix the parameters which better reproduce the simulations results and to point out to the pros and cons of our method.

The thesis is divided into four chapters

- The first one gives an essential cosmological scenario. Its aim is to provide the theoretical concepts necessary to understand the cosmological framework in which the research takes place. For this reason, after a brief introduction to the cosmological principle and the equations that lead the Universe's evolution, there is a focus on cosmological models and a dealing with the growth of perturbations in linear and non-linear regime.
- In the second chapter we depict the large scale structure, under an observational and a numerical point of view. We point out the clusters and their physical properties, in particular their connection with dark matter.
- The third chapter is dedicated to the gravitational lensing theory. Starting from simple assumptions, we can derive all the quantities we need to understand and give a global description of lensing, with the aim to introduce the concepts used in the research.
- In the last chapter we described in detail our work, the analysis and the results coming from the comparison with the simulations.

In the conclusions we summarize all the results we achieved, the emerged critical points and the future perspectives.

Chapter 1

Background

The standard cosmological model describes the evolution of the Universe. It is based upon the Friedmann-Robertson-Walker cosmological model, called also *hot Big Bang model.* In this chapter we introduce and summarize the theory and the evidences that support the standard cosmology.

1.1 Cosmological overview

In the space we can observe gravitationally bound structures, in which galaxies are the fundamental units. Their distribution in the local space under the action of gravity shows regions which have different densities and we can note that galaxies are bound in bigger and bigger structures, like groups and clusters, connected among them by filaments of matter.
If we move our attention on scales bigger than 100 Mpc, we can observe that the Universe is not disturbed by the great variety of its substructures.
On large scales the distribution of the structures is almost uniform and it does not show any preferential direction. The position of the observer does not influence the measure of the physic's laws and every observer[1], wherever he is, is able to measure the same physical laws.
This concept is the idea on which is based the *COSMOLOGICAL PRINCIPLE*: *the Universe is homogeneous and isotropic on large scales.*

For these reasons we will use the theory of the General Relativity to describe the cosmological overview and we assume that its equations satisfy the cosmological principle.

---

[1] We consider observer in inertial reference systems.

In the framework of General Relativity the space has the nature of a four-dimensional space, with three spatial dimensions and a temporal dimension, we call it *space-time*.

Once we have derived the metric, we define the fundamental parameters and we introduce the equations which describe the Universe and its evolution.

1.1.1 Geometry

To describe the geometrical characteristics of a space, we need to define at first the concept of distance between two points and then to define the scalar product between two vectors that belong to that space.

We take a generic vector in the space-time; because it is four-dimensional, $dx_\alpha = (dt, dx_i)$ will be a four-vector[2].

The scalar product is defined by:

$$dx_\alpha dx^\alpha = g_{\alpha\beta} dx^\alpha dx^\beta = g_{00} dt^2 + 2g_{0i} dt dx^i + g_{ij} dx^i dx^j; \tag{1.1}$$

the matrix $g_{\alpha\beta}$ is the so-called *metric*, where all the geometrical characteristics of the space are stored.

Assuming the cosmological principle, the geometry of the space-time has to satisfy the requests of homogeneity and isotropy.

Satisfying the isotropy is equivalent to ask the absence of preferential directions: for this reason the mixed element of space and time cannot exist, so $g_{0i} = 0$.

In addition to this because looking far in space is equal to look back in time, observed objects are in an evolutionary phase earlier than the objects in the local Universe; therefore to impose the homogeneity we need to consider that information coming from distant sources travel at a finite velocity: the *speed of light* $c \sim 3 \times 10^{10}$ cm sec^{-1}: so $g_{00} = c^2$.

After these assumptions we can obtain the norm of a four-vector:

$$ds^2 = c^2 dt^2 + g_{ij} dx^i dx^j = c^2 dt^2 - dl^2. \tag{1.2}$$

---

[2] Convention: the Latin indexes, like i,j,k..., are related to the three spatial coordinates, and vary among 1,2,3; the Greek indexes α,β,γ... are associated to the four coordinates of the space-time, so they will have values among 0,1,2,3, 0 is the temporal coordinate. We adopt the Einstein convention: the repeated indexes are summed.

If $ds^2 = 0$, we define it *lightlike distance*, it identifies the geodesics of the light; if $ds^2 > 0$, it is called *timelike distance*, it belongs to particles which have a velocity smaller than c; at least, if $ds^2 < 0$ we talk about *spacelike distance* and it is related to superluminal particles; it is evident that dl^2 is a surface element in the three-dimensional space, see the figure 1.1.

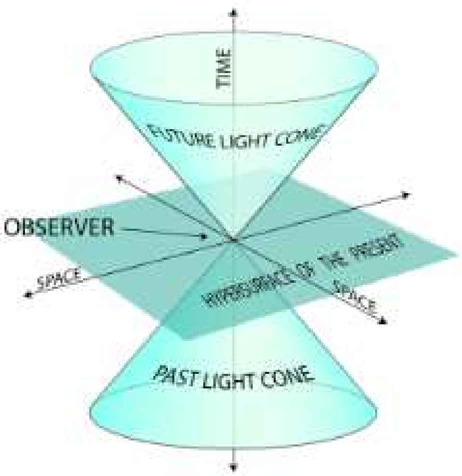

Figure 1.1: Light cone of the space-time. The photons travel through geodesics that lie on the light cone surface, the world lines of particles with velocities smaller than c are inside the cone, while the lines of ultra-relativistic particles run outside the cone.

We need to determine g_{ij}, in such a way that the assumptions of the cosmological principle are satisfied at every time.
In general we obtain

$$ds^2 = c^2dt^2 - a(t)^2\left(\frac{dr^2}{1-Kr^2} + r^2d\Omega^2\right), \qquad d\Omega^2 = d\theta^2 + \sin^2\theta d\varphi^2; \quad (1.3)$$

this diagonal metric is called *Robertson-Walker's metric.*
In the expression 1.3 the physical coordinate $x(t) = a(t)r$ is splitted into an dimensionless component r, comoving coordinate in solid with the rest frame, and in a component with the dimension of a length and depending on the time $a(t)$, the *scale factor*; K is the *curvature's parameter* of the Universe, related to the kind of geometry, as is shown in figure 1.2.

1.1.2 Parameters

We introduce the concept of *proper distance* to define two parameters that are necessary to describe the Universe: the scale factor $a(t)$ and the *cosmological redshift* z, from which we derive others two important parameters, the *Hubble constant* $H(t)$ and the *deceleration parameter* $q(t)$.

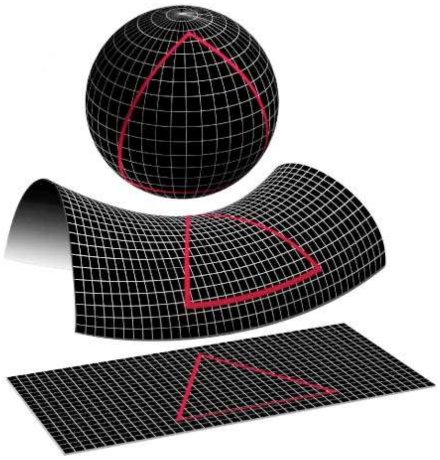

Figure 1.2: Geometry of the Universe: $K = 1$ spherical geometry, the Universe is an hypersphere, the space is closed, the volume is finite but unlimited, the parallels meet at the poles; $K = -1$ hyperbolic geometry, the Universe is an hyperboloid, the space is open and unlimited, the parallels never meet; $K = 0$ euclidean geometry, the Universe is flat, the space is infinite and the parallels will meet only at the infinite.

We calculate the proper distance at the time t from the origin, in which we have posed the observer, of a comoving object at the radial coordinate r, by integrating the equation 1.3:

$$d(r,t) = a(t)\int_0^r \frac{dr}{\sqrt{1-Kr^2}} = a(t)\begin{cases} \sin^{-1} r & K=1 \\ r & K=0 \\ \sinh^{-1} r & K=-1 \end{cases} \tag{1.4}$$

Because in the comoving frame r is constant in time, the proper distance between the observer and a comoving object increases or decreases proportionally to $a(t)$. We know that every position is totally equivalent to each other, so this proportionality is conserved between two different observers wherever they are in the Universe.

We can infer in this way that $a(t)$ is the measure of how much the Universe changes its dimensions during the time. In fact if we look the variation of the proper distance,

$$\dot{d} = \frac{\dot{a}}{a} d, \tag{1.5}$$

it is evident that the growing of $a(t)$ during the time, due to the expansion of the Universe, implies an increasing of the proper distance and vice versa, while its constance implicates a static Universe.

The rate on which the proper distance varies is the general expression of the *Hubble's law*: *the galaxies are receding form each other with a velocity that is proportional to their distance*:

$$v = H(t)d; \tag{1.6}$$

$H(t)$ is the Hubble constant and comparing the equation 1.5 with the equation 1.6 we obtain that:

$$H(t) \equiv \frac{\dot{a}\,(t)}{a(t)}. \tag{1.7}$$

The Hubble constant is constant in space but not in time: at the moment its value is[3] $H(t_0) = H_0 = 71 \pm 6$ km sec^{-1} Mpc^{-1} (Freedman et al., 2001). Due to the persisting of the uncertainties on the determination of H_0, currently we use $H_0 = 100h$ km sec^{-1} Mpc^{-1}, where $h \sim 0.7$ is an adimensional parameter.

The information on $a(t)$ comes from the analysis of distant galaxies spectra compared with spectra observed in laboratory. From the comparison it arises that the spectral lines of the galaxies are shifted in frequency or wavelength. How can we calculate it?

Taking a comoving frame, equation 1.3, centered in the observer, we integrate the equation for a geodesic of a light ray, $ds^2 = 0$, that is emitted by a source in r at the time t_e, and that arrives in the origin at time t_0:

$$\int_{t_e}^{t_0} \frac{dt}{a(t)} = \int_0^r \frac{dr}{\sqrt{1 - Kr^2}} = f(r). \tag{1.8}$$

The quantity $f(r)$ is constant in time, so the differential in 1.8 produces

$$\begin{aligned} \frac{\delta t_0}{a_0} &= \frac{\delta t_e}{a(t_e)}, \qquad (1.9) \\ \delta t_0 = \frac{1}{\nu_0} \quad &e \quad \delta t_e = \frac{1}{\nu_e}, \end{aligned}$$

where ν_0 and ν_e are, respectively, the frequency of the observed radiation and the frequency of the emitted radiation. The relation between emitted frequency and observed one, or equally between wavelengths, will be

$$\frac{\nu_0}{\nu_e} = \frac{a(t_e)}{a_0} \qquad \Longleftrightarrow \qquad \frac{\lambda_0}{\lambda_e} = \frac{a_0}{a(t_e)}. \tag{1.10}$$

Therefore, if $a(t)$ increases, the observed radiation will shift toward minor frequency or bigger wavelengths, in this case the light becomes redder and will be subjected to the redshift effect, while if the object is approaching $a(t)$ decreases and the radiation undergoes a blushift.

---

[3] Here and after the subscript 0 is related to physical quantity measured or calculated at present time $t = t_0$.

The proportionality factor on which frequencies and wavelengths change is by convention defined:

$$z \equiv \frac{\lambda_e - \lambda_0}{\lambda_0} \quad \Rightarrow \quad \frac{a(t_e)}{a_0} = 1 + z, \tag{1.11}$$

z is the cosmological redshift that in the case of blushift is negative.
At each z we can associate an age of the Universe: the *lookback time* t_L is the difference between the age of the Universe at present time t_0 and the age of the Universe at the time in which the photons of the source that we are observing have been emitted t_e and it gives the measure of how much we are looking backward.

From the scale factor $a(t)$ we can also derive the deceleration parameter $q(t)$. It indicates if the expansion of the Universe is in acceleration, deceleration or it is uniform and at the present time t_0 is defined as:

$$q_0 \equiv -\frac{1}{H_0^2 a_0} \frac{d^2 a(t)}{dt^2}\Big|_{t=t_0} \begin{cases} = 0 & \textit{uniform expansion} \\ < 0 & \textit{accelerated expansion} \\ > 0 & \textit{decelerated expansion} \end{cases} \tag{1.12}$$

1.1.3 Distance

On the base of what we said, the measure of distances at low redshift can neglect the expansion of the Universe and the curvature of the space-time due to the matter.

Measures for $z \lesssim 0.1$ are very important for cosmology because they allow to limit the value of H_0 and to calibrate the measure of the distances for higher redshift.
The main indicators of the distances at redshift $z \lesssim 0.03$ are the trigonometric parallax, the proper motions and the apparent magnitude through the distance module. At higher redshift always less than 0.1, we use the Tully-Fisher relation, the Faber-Jackson relation, the fundamental plane of elliptical galaxies and Supernovae Ia.

The measurement of the distances at $z > 0.1$ allows us to understand if the expansion of the Universe is in acceleration or deceleration, and which is the velocity.

We take the relation between the apparent luminosity l of a source with intrinsic luminosity L at a distance d from the observer. If we want to take care about the expansion of the Universe, we have to modify this relation.
In fact in the meanwhile the light reaches the observer, the area of the sphere on which the radiation is distributed, centered on the source and passing through the observer, is $4\pi r_1^2 a_0^2$, where $r_1 a_0$ is the distance of the observer from the source at time t_0; the rate of the arrive of the photons decreases of a factor $\frac{1}{1+z}$ respect to the emission rate and the same happens to the energy of the photons received, decreased of the same factor.
The new relation will be:

$$l = \frac{L}{4\pi d^2} \qquad \Rightarrow \qquad l = \frac{L}{4\pi r_1^2 a_0^2 (1+z)^2}; \tag{1.13}$$

we define *luminosity distance* d_L, the quantity such that the relation between apparent and intrinsic luminosity has the same form of the original equation:

$$l = \frac{L}{4\pi d_L^2} \qquad \Rightarrow \qquad d_L \equiv a_0 r_1 (1+z). \tag{1.14}$$

An extra definition can be obtained by the comparison of the angular dimensions with the physical ones and this quantity is the *angular distance* d_A.
If a source, at the comoving coordinate r_1 and that at the time t_1 emits light, is observed at current time under an angle of θ, taking the equation 1.3 and placing $d\varphi = 0$ and $dt = 0$ we obtain that $D_{pr}^2 = ds^2 = a(t_1)^2 r_1^2 \theta^2$, in which D_{pr} is the proper diameter of the source. Therefore

$$d_A = \frac{D_{pr}}{\theta} \qquad \Rightarrow \qquad d_A \equiv a(t_1) r_1; \tag{1.15}$$

$$d_A = d_L (1+z)^{-2}. \tag{1.16}$$

1.1.4 Equations

The equations of General Relativity allow us to connect the metric of the space-time with the distribution of the matter, describing in this way the dynamics of the Universe.

The expansion is driven by the *Einstein's field equation*

$$R_{\alpha\beta} - \frac{1}{2} g_{\alpha\beta} R = \frac{8\pi G}{c^4} T_{\alpha\beta}; \tag{1.17}$$

here $R_{\alpha\beta}$ is the *Ricci curvature tensor*, R is the *Ricci's scalar* or *scalar curvature*, $g_{\alpha\beta}$ is the metric and $T_{\alpha\beta}$ is the *stress-energy tensor* in which it is contained the contribution of pressure, mass and energy of the Universe. It is calculated considering the different components: baryonic and non-baryonic matter, relativistic and non-relativistic, the radiation and, as we can see in the following, the vacuum.

We made two assumptions: the first needs that the space is homogeneous and isotropic and this means that we will use the equation 1.3; the second one requires that $T_{\alpha\beta}$ describes a perfect fluid:

$$T_{\alpha\beta} = (P + \rho c^2)\mu_\alpha \mu_\beta - P g_{\alpha\beta}, \tag{1.18}$$

where P is the *pressure*, ρc^2 is the *energy density* including the rest mass and μ_α is the four-velocity.
From the field equation 1.17 under the two conditions we can derive the *Friedmann equations*:

$$\dot{a}^2(t) + Kc^2 = \frac{8\pi}{3} G \rho a^2(t), \tag{1.19}$$

$$\ddot{a}(t) = -\frac{4\pi}{3} G \Big(\rho + \frac{3P}{c^2}\Big) a(t). \tag{1.20}$$

The equation 1.20 is also-called *acceleration equation*.

Einstein, convinced that the Universe was static, added a term, the *Cosmological Constant* Λ, which had the role to balance the trend of the Universe to collapse or to expand. This term had the physical meaning of repulsive energy of the vacuum. With the introduction of Λ the field equation 1.17 had a new form:

$$R_{\alpha\beta} - \frac{1}{2} g_{\alpha\beta} R - g_{\alpha\beta}\Lambda = \frac{8\pi G}{c^4} T_{\alpha\beta}. \tag{1.21}$$

In order to write the tensors in a more compact way we define the *effective stress-energy tensor*, the *effective pressure* and the *effective density*:

$$\tilde{T}_{\alpha\beta} = T_{\alpha\beta} + \frac{\Lambda c^4}{8\pi G} g_{\alpha\beta}, \tag{1.22a}$$

$$\tilde{P} = P - \frac{\Lambda c^4}{8\pi G}, \tag{1.22b}$$

$$\tilde{\rho} = \rho + \frac{\Lambda c^4}{8\pi G}, \tag{1.22c}$$

$$\Longrightarrow \qquad \tilde{T}_{\alpha\beta} = \tilde{P}\, g_{\alpha\beta} + (\tilde{P} + \tilde{\rho}\, c^2)\mu_\alpha \mu_\beta. \tag{1.22d}$$

From the definitions 1.22b, 1.22c, 1.22d, we can rewrite the new Friedmann equations, equal in form to the equations 1.19 and 1.20.

The last equations necessary to build the models of Universe are the *adiabatic equation*, which describes the adiabatic expansion of the Universe,

$$d(\rho a^3) = -\frac{P}{c^2} da^3, \tag{1.23}$$

and the *equation of state*, that relates density and pressure,

$$P = w\rho c^2. \tag{1.24}$$

Because the sound velocity is defined as $c_s^2 \equiv \left(\frac{\partial P}{\partial \rho}\right)\Big|_{s=cost}$, then

$$c_s = \sqrt{w}c \qquad \Rightarrow \qquad \textit{Zel'dovich range:} \quad 0 \leqslant w < 1. \tag{1.25}$$

The value of the adimensional parameter w depends on the component of the Universe considered: $w = 0$ is for the non-relativistic matter which corresponds to $P = 0$, $w = 1/3$ is for a photons gas corresponding to $P = \rho c^2/3$ and $w = -1$ is for Λ for which $P = -\rho c^2$.

1.1.5 Models

Once all the equations that describe the Universe have been obtained, the possible cosmological models are all those we can derive by changing the dominant component or by varying the curvature.

Some models consider only one component and this is justified by the fact that in each era only one is dominant respect to the others.
The flat Universe of Einstein-de Sitter has $K = 0$, it has a positive cosmological constant and does not consider ordinary matter; it predicts an infinite expansion, the *Big Rip*.
The Friedmann's Universes are the so-called standard cosmological models and they do not include the cosmological constant ($\Lambda = 0$). For $K = 0$ they correspond to a flat Universe for which an exact solution exists, while open Universe with $K = -1$ and closed one with $K = 1$ have only parametric solution.

We can measure the space-time curvature calculating the ratio between the density and the *critical density*[4] defined as:

$$\rho_{0,cr} \equiv \frac{3H_0^2}{8\pi G} \Rightarrow \begin{cases} \rho_0 < \rho_{0,cr} & \Rightarrow \quad K = -1 \\ \rho_0 = \rho_{0,cr} & \Rightarrow \quad K = 0 \\ \rho_0 > \rho_{0,cr} & \Rightarrow \quad K = 1 \end{cases} \tag{1.26}$$

We define the *density parameter*, Ω_i, for each components:

$$\textit{radiation} \qquad \Omega_\mathrm{R} = \frac{\rho_{0,R}}{\rho_{0,cr}}, \tag{1.27a}$$

$$\textit{matter} \qquad \Omega_\mathrm{M} = \frac{\rho_{0,M}}{\rho_{0,cr}}, \tag{1.27b}$$

$$\textit{cosmological constant} \qquad \Omega_\Lambda = \frac{\rho_{0,\Lambda}}{\rho_{0,cr}} = \frac{\Lambda c^2}{3H_0^2} \quad \textit{(costant)}. \tag{1.27c}$$

The *total density parameter*, Ω_0, is defined as the sum of all density parameters:

$$\Omega_0 = \Omega_\mathrm{R} + \Omega_\mathrm{M} + \Omega_\Lambda \begin{cases} < 1 & \Rightarrow \quad K = -1 \\ = 1 & \Rightarrow \quad K = 0 \\ > 1 & \Rightarrow \quad K = 1 \end{cases} \tag{1.28}$$

On the base of the definitions 1.27a, 1.27b e 1.27c, we can redefine the deceleration parameter:

$$q = \frac{\Omega_\mathrm{M}}{2} - \Omega_\Lambda. \tag{1.29}$$

In an epoch dominated by the cosmological constant, the parameter q will be negative and the Universe is subjected to an accelerated expansion.

We derive that, in the evolution of flat Universe, the density parameter is fixed to the unit and the geometry of the Universe does not change during the time. This is true for all kind of Universe: the geometry once fixed does not have changes.

Thus the destiny of the Universe depends on its curvature and on its contents of matter and energy, see figure 1.3.

A flat Universe will have an expansion with a final velocity equal to zero.

An open Universe with $K = -1$ and $\Omega_0 < 1$ will expand till the *heat death* too, in fact $a(t)$ increases as in the flat Universes: $\dot{a}\,(t)$ never goes to zero and it is always positive.

Instead a closed Universe with positive curvature for which $\Omega_0 > 1$ will experiment an expansion followed by a collapse, the *Big Crunch*. In fact there

---

[4] Introducing the current value of H_0 in unit of h, $H_0 = 100h$ km sec^{-1} Mpc^{-1} we have that $\rho_{0,cr} = 1.4 \cdot 10^{-29} h^2$ gr cm^{-3} $= 2.775 \cdot 10^{11} h^2\, M_\odot$ Mpc^{-3}.

is a time t_m in which the derivative of the expansion parameter $\dot{a}\ (t)$ is zero. This means that for $t < t_m$ the expansion parameter increases as in the other Universe, but for time $t > t_m$ $a(t)$ decreases. Because the curve describing the evolution of $a(t)$ is symmetric respect to t_m, for $t_f = 2t_m$ another singularity exists, that is symmetric to Big Bang that implies the final collapse.

Figure 1.3: The curvature of the Universe, as its fate, depends strongly on the quantity of matter and energy that it contains. In the figure we can observe the trends, depending on time, of the scale factor for each kind of geometry (Coles and Lucchin, 2002).

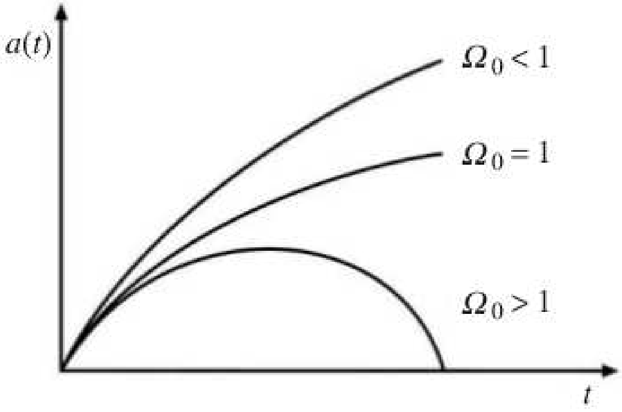

The Big Bang

The Friedmann's models have in common an initial singularity in which $a(t)$ is formally zero and the density goes to infinite (figure 1.4).

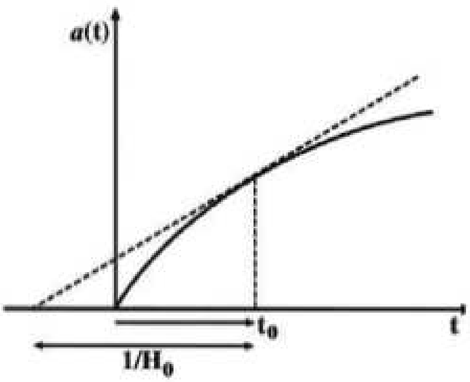

Figure 1.4: The concavity of $a(t)$ predicts the existence of an initial singularity (Coles and Lucchin, 2002).

Considering the Friedmann's equation 1.20 we can observe that $\ddot{a}\ (t)$ is always negative and, if $w \in [0, 1[$, $\dot{a}\ (t)$ is always positive. This means that in the Zel'dovich range $a(t)$ is a concave and increasing function.

Furthermore from equation 1.19 we can note that exists an instant $t = 0$ for which $\dot{a}(0) = 0$. This instant, in which $a(0) = 0$ and the density is divergent, is the initial singularity called *Big Bang*. We would stress that is a consequence of the initial conditions and not an effect of the pressure.

Flat models

In general, for flat models with only one fluid, where $\Omega_0 = 1$, from equation 1.24 we can derive the evolutionary trends of the physical parameters for each components i: radiation R, matter M and cosmological constant Λ.
Evolution of the density:

$$\rho_i = \rho_{0,i}\Big(\frac{a_0}{a(t)}\Big)^{3(w_i+1)}. \tag{1.30}$$

By replacing the equation 1.30 in the equation 1.19 we obtain the time evolution of the hubble constant:

$$H^2(t) = H_0^2\Big(\frac{a_0}{a(t)}\Big)\Big[(1-\Omega_0) + \Omega_{0,i}\Big(\frac{a_0}{a(t)}\Big)^{1+3w_i}\Big]. \tag{1.31}$$

By integrating the equation 1.31 we derive the trend of $a(t)$ during the time by varying the dominant component :

$$\textit{Evolution of } a(t) \qquad a(t) = \begin{cases} a_0\Big(\frac{t}{t_0}\Big)^{1/2} & \textit{radiation} \\ a_0\Big(\frac{t}{t_0}\Big)^{2/3} & \textit{matter} \\ a_0 e^{H(t-t_0)} & \Lambda \end{cases} \tag{1.32}$$

These equation show us as the expansion parameter in flat Universe increases indefinitely with time.
The equations 1.32 are equivalent to:

$$t = \begin{cases} t_0(1+z)^{-2} & \textit{radiation} \\ t_0(1+z)^{-3/2} & \textit{matter} \\ \frac{1}{H}\ln(1+z) + t_0 & \Lambda \end{cases} \tag{1.33}$$

Using the equation 1.33 and the equation 1.31 we obtain an expression to calculate the age of the Universe for each component:

$$t_0 = \frac{2}{3(1+w_i)H_0}\ . \tag{1.34}$$

The relation between temperature and time[5] is given by

$$T \approx \frac{10^{10}}{t^{1/2}}. \tag{1.35}$$

---

[5] Time in this formula is expressed in seconds.

Curve models

Curve models with one component have $\Omega_0 \neq 1$. Analyzing the behavior of the equation 1.31 for early times, near the Big Bang epoch, and so for very high redshift, we can see that the term $(1-\Omega_0)$ can be neglected because $\frac{a_0}{a(t)}$ increases. For this reason from equation 1.31 we have:

$$H^2(t) \simeq H_0^2 \Omega_{0,i} \left(\frac{a_0}{a(t)} \right)^{1+3w_i}. \tag{1.36}$$

Therefore curve models near the Big Bang are similar to the Einstein-de Sitter model. This means that with good approximation we can ignore the curvature when we are studying the early phases of the Universe.

1.2 Little perturbations grow up

The current standard scenario, the ΛCDM model, in which the cosmic structures formation is situated, requests the assumptions of some conditions deduced from observations.

- The dark matter is cold, this means non-relativistic during all the epochs that are interesting for the cosmic structures formation, non-collisional, non-baryonic and it dominates the density parameter of the matter $\Omega_{\rm M} = 0.25$.

- The baryons, predicted by the Big Bang nucleosinthesys and measured by the *Cosmic Microwave Background*[6], have a density parameter $\Omega_{\rm b} \sim 0.04$.

- The density perturbations have to be formed during the *Inflation*, and their following increasing is the responsible of the structures formation. The inflationary model requires a Universe in which $\Omega_0 \simeq 1$, so $1 - \Omega_{\rm M} = \Omega_\Lambda \approx 0.75$.

- At the epoch of the hydrogen recombination, $z_{rec} \sim 10^3$, the Universe has to be homogeneous and isotropic, so we ca use the Friedmann's models and the Robertson-Walker metric; the fluctuations of the order of 10^{-5} observed in the CMB spectrum seem to be the amplification of quantistic fluctuations originated at the Big Bang epoch.

---

[6] Here and after we refer to it as CMB.

- The cosmic structures formation is based on the concept of *gravitational instability*: the regions where $\delta = \frac{\Delta\rho}{\rho}$ is higher than the mean value have the tendency to grow up and to empty the underdense regions; this process is dominated by the CDM that, decoupling from radiation before the baryonic matter, forms the halos or potential wells, where $\delta \gg 1$, in which the perturbations of the matter fall at the decoupling.
- After the formation of the dark matter halos where the gas falls and becomes denser, galaxies form.

Observative proofs

The level of non-homogeneity on the smaller scales ($\sim 0.2\,h^{-1}$ Mpc) requires a recent history of formation of the structures, that is in agreement only with models in which the dark matter is cold.
There are several CDM models that are different for the “invisible matter” contents: invisible standard matter (sCDM), hot and small dark matter (νCDM), cosmological constant (ΛCDM) and others more complicated. The ΛCDM model is the only one whose predictions are also consistent with observations (Turner, 1997).

The luminosity distances of supernovae Ia have been determined using the existing relation between the luminosity and the light curve shape. Combining the measures with previous results several parameters have been calculated: Hubble constant H_0, matter density Ω_{M}, vacuum energy density Ω_Λ, deceleration parameter q_0 and the dynamical age of the Universe t_0. Distances of SN are on the average $10\% - 15\%$ higher than those predicted in a open Universe with $\Omega_{\mathrm{M}} = 0.2$ e $\Omega_\Lambda = 0$. The different methods of analysis of the light curves support models where the cosmological constant is greater than zero ($\Omega_\Lambda > 0$) and in which the expansion is, at the present time, accelerated ($q_0 < 0$). Even considering the possible sources of systematic error, like extension, local perturbations of the expansion rate, the metallicity evolution in the medium and the gravitational lensing, none of these effects can explain the data with a model where $\Omega_\Lambda = 0$ e $q_0 \geqslant 0$ (Riess et al., 1998). In the figure 1.5 it is evident the concordance among the different dataset on the geometry of the Universe.

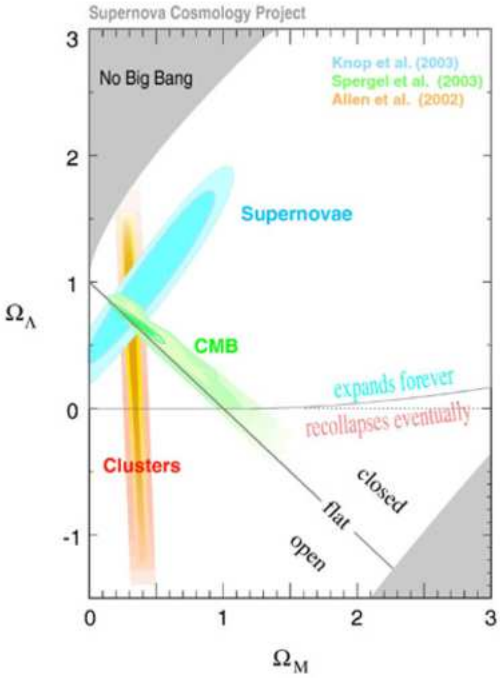

Figure 1.5: In the diagram is shown the combination of the datasets coming from supernovae, from galaxy clusters and from CMB. The continuous line is for the flat Universe: $\Omega_M + \Omega_\Lambda = 1$. Image from Supernova Cosmology Project; http://supernova.lbl.gov/.

The analysis coming from the statistic of weak gravitational lensing supports a model where Ω_Λ is different from zero. In addition to this, fixing $\Omega_M + \Omega_\Lambda = 1$, the number of the gravitational arcs, or in other words the probability that a galaxy at redshift z_s is subjected to the effect of lensing, increases dramatically with $\Omega_\Lambda \to 1$ and the fact that we do not observe a so high number of arcs puts a superior limit $\Omega_\Lambda \lesssim 0.7$.
The galaxy clusters are very important because the quantity of matter that they contain reflects statistically the content of matter in the Universe. Current measures show $\Omega_M \sim 0.3$ and $\Omega_\Lambda = 1 - \Omega_M$.

Measures coming from the CMB underline the strict dependence of the fist peak position of the acoustic oscillations with the geometry of the Universe:

$$\ell_{peak} \propto 220\,\Omega_0^{-1/2}. \tag{1.37}$$

ℓ_{peak} is the measure of the angular scale subtended by the Universe radius at the epoch of the formation of the CMB. A Universe with negative or positive curvature has angular dimensions bigger or smaller than the angular dimension of a flat Universe. This relation allow us to fix some limits to the value of $\Omega_0 \sim 1$.

1.2.1 Jeans theory

Giving a spherical distribution of matter, we would like to know which is its evolution.
In the case that self gravity dominates, it will collapse, while on the other hand, if the pressure forces are prevalent, it will expand.
As consequence of this, it exists a limit mass, called *Jeans mass* M_J, so systems with mass M higher than M_J will collapse, while systems whit smaller masses will expand under the action of pressure. M_J is naturally correlated with a scale radius, called *Jeans radius* R_J.
We can qualitatively derive the value of M_J from the energetic balance, from the balance of the forces or from the balance of the times:

$$M_J = \frac{4\pi}{3}\rho R_J^3 \quad \Rightarrow \quad R_J = \begin{cases} v\sqrt{\frac{1}{2G\rho}} & \textit{energies} \\ c_s\sqrt{\frac{1}{G\rho}} & \textit{forces} \\ c_s\sqrt{\frac{1}{4G\rho}} & \textit{times} \end{cases} \tag{1.38}$$

The *Jeans theory* describes the behavior of perturbations inside of a self gravitating system, as the Universe can be.

The thermodynamic variables are *density* ρ, *temperature* T, *pressure* P, *entropy* S and *gravitational field* ϕ. The system of equations is the following:
Continuity equation:

$$\frac{\partial \rho}{\partial t} + \nabla\cdot(\rho\vec{v}) = 0, \tag{1.39}$$

Euler equation[7]:

$$\frac{\partial \vec{v}}{\partial t} + (\vec{v}\cdot\nabla)\vec{v} = -\frac{1}{\rho}\nabla P - \nabla\phi, \tag{1.40}$$

Poisson equation:

$$\nabla^2\phi = 4\pi G\rho, \tag{1.41}$$

State equation:

$$P = P(\rho, S) \quad \textit{for adiabaticity} \Rightarrow \quad P = P(\rho), \tag{1.42}$$

Entropy evolution:

$$\frac{\partial S}{\partial t} = \dots \quad \textit{for adiabaticity} \Rightarrow \quad \frac{\partial S}{\partial t} = 0. \tag{1.43}$$

---

[7] It is the hydrodynamical equivalent of $F = ma$

Considering a static Universe, we suppose to know an unperturbed solution of the homogeneous system, and we perturb it (table 1.1) to observe how the perturbations evolve in time.

unperturbed solution	perturbed solution $\delta = \frac{\delta\rho}{\rho}$
$\rho = \rho_b = cost$	$\rho = \rho_b + \delta\rho = \rho_b(1+\delta)$
$P = P_b = cost$	$P = P_b + \delta P$
$\vec{v} = \vec{0}$	$\vec{v} = \delta\vec{v}$
$\phi = \phi_b = cost$	$\phi = \phi_b + \delta\phi$
linear phase$\Rightarrow$*we impose* δ, δP, $\delta\vec{v}$, $\delta\phi \ll 1$	

Table 1.1: Perturbations theory. We note that the unperturbed solution is not consistent with the equations: an homogeneous distribution of density ρ describes an expansion or an isotropic collapse, in other words this means that a stationary solution of the system does not exist.

If we consider the thermodynamical variables as plane waves:

$$\delta f(\vec{r}, t) = \delta f_k \exp{(i\vec{k} \cdot \vec{r} + i\omega t)}, \tag{1.44}$$

where δf_k is the wave *amplitude*, ω is the *pulsation* and k is the *wavenumber*, we obtain the *dispersion relation*

$$\omega(\omega k^2) - \vec{k} \cdot (c_s^2 \vec{k} k^2 - 4\pi G \rho_b \vec{k}) = 0, \tag{1.45}$$

$$\Rightarrow \quad \omega^2 = k^2 c_s^2 - 4\pi G \rho_b. \tag{1.46}$$

It is interesting to know how and why the perturbations grows up.

From the dispersion relation 1.45 we can derive an expression for the *Jeans wavenumber* k_J and so for R_J:

$$\omega^2 = 0 \quad \Rightarrow \quad k^2 = \frac{4\pi G \rho_b}{c_s^2} \equiv k_J^2,$$

$$k_J = \frac{2\pi}{\lambda_J} \quad \Rightarrow \quad \lambda_J = c_s \sqrt{\frac{\pi}{G\rho_b}}\,.$$

On the base of these definitions we can rewrite the 1.46 in this way:

$$\omega^2 = k^2 c_s^2 \Big[1 - \Big(\frac{k_J}{k}\Big)^2\Big] = k^2 c_s^2 \Big[1 - \Big(\frac{\lambda}{\lambda_J}\Big)^2\Big]; \tag{1.47}$$

it is evident that the behavior of the wave depends on the regimes that it will encounter during its evolution.

If $\lambda < \lambda_J$ or $k > k_J$ the typical pulsation of the wave is real,

$$\omega^2 > 0 \quad \Rightarrow \quad \omega = \pm k c_s \left[1 - \left(\frac{\lambda}{\lambda_J}\right)^2\right] : \tag{1.48}$$

the wave will travel with a phase velocity, defined as $v_f = \frac{\omega}{k}$, equal to:

$$v_f = c_s \left[1 - \left(\frac{\lambda}{\lambda_J}\right)^2\right]. \tag{1.49}$$

Analyzing the asymptotic trends we note that if $\lambda \to 0$ the wave propagates with the sound velocity $v_f = c_s$, while if $\lambda \to \lambda_J$ the wave is stationary because $v_f \to 0$; in any case its amplitude is constant and there is not collapse.

If $\lambda > \lambda_J$ or $k < k_J$ the pulsation of the wave is imaginary,

$$\omega^2 < 0 \quad \Rightarrow \quad \omega = \pm i \sqrt{4\pi G \rho_b} \left[1 - \left(\frac{\lambda_J}{\lambda}\right)^2\right]^{1/2}, \tag{1.50}$$

the wave does not propagate, it is like:

$$\delta f(\vec{r}, t) = \delta f_k \exp\left(\pm|\omega| t\right) \exp\left(i\vec{k} \cdot \vec{r}\right). \tag{1.51}$$

Its amplitude $\delta f_k \exp\left(\pm|\omega| t\right)$ decreases or increases exponentially with time. The increasing solution has a big cosmological interest, because the growing of the amplitude of the density perturbations imply the collapse of the structure. We calculate the *collapsing time of the perturbations* τ_g and the *free-fall time* τ_{ff}:

$$\tau_g = \frac{1}{|\omega|} = (4\pi G \rho_b)^{-\frac{1}{2}} \left[1 - \left(\frac{\lambda_J}{\lambda}\right)^2\right]^{-1/2}, \tag{1.52}$$

$$\tau_{ff} \propto \frac{1}{G\rho_b}; \tag{1.53}$$

if $\lambda \gg \lambda_J$ the growing time of perturbations tends to the free-fall time, the perturbation shows the *gravitational instability* phenomenon and the collapse can start.

1.2.2 Expanding Universe

In an expanding Universe perturbations will grow more slowly than in static Universe.

Interesting scales and times

The Jeans scale R_J measures when pressure starts to be not negligible,

$$R > R_J \quad \Rightarrow \quad \textit{pressure is negligible respect to the gravity}$$
$$R < R_J \quad \Rightarrow \quad \textit{pressure stops the collapse}$$

The *horizon radius* R_H is the scale inside which objects are in causal connection,

$$R_H(t) = \int_0^t \frac{cdt'}{a(t')}; \quad R > R_H \quad \textit{all scales can grow up} \tag{1.54}$$

The *dissipation scale* R_D is the scale on which the cancellation of perturbations happens. It separates scale $R_D < R < R_J$ on which perturbations are propagating like acoustic waves from scales $R < R_D$ on which the wave is dissipated.

The interesting times are the decoupling[8], $z_{dec} \sim 1089$, the moments in which the dominant component of the Universe changes, like z_{eq} in which we have the passage from radiation to matter as dominant component and $z_{M\Lambda}$ in which we pass from matter to Λ, and the time in which particles pass from a relativistic regime to a non-relativistic one, z_{nr}.

Applying the equations 1.19 and 1.20 both to the background Universe, in which the curvature parameter is $K_b = 0$ and the density is ρ_b, and to the perturbation, with $K_p = 1$ e ρ_p, we define the density fluctuation as

$$\delta \equiv \frac{(\rho_p - \rho_b)}{\rho_b} = \frac{\rho_p}{\rho_b} - 1, \tag{1.55}$$

and we obtain the temporal evolution of the density perturbation out of the horizon:

$$\delta = \frac{3c^2}{8\pi G \rho_b a^2},$$
$$\rho_b \propto a^{-3(1+w)}, \qquad a \propto t^{\frac{2}{3(1+w)}},$$
$$\delta \propto a^{1+3w} \propto t^{\frac{2(1+3w)}{3(1+w)}}. \tag{1.56}$$

---

[8] Recombination, decoupling and last scattering happen in a relatively short time, so we can use them as equivalently times scale, $z_{rec} \sim z_{dec} \sim z_{ls}$.

For $t < t_{eq}$ and $\lambda_J > R_H$, the dominant component is the radiation:

$$\rho \sim \rho_R \quad \xrightarrow{w=\frac{1}{3}} \quad \delta \simeq \delta_R(t) \propto a^2 \propto t$$

$$\begin{array}{lll} \lambda > R_H & \Rightarrow & \delta_R \propto \delta_{DM} \propto \delta_b \propto a^2 \\ \lambda < R_H & \Rightarrow & \left\{ \begin{array}{ll} \delta_R & \propto \delta_b \propto \textit{oscillating waves} \\ \delta_{DM} & \propto \textit{constant due to the stagnation} \end{array} \right. \end{array}$$

In the epoch when the radiation is dominant, $\Omega = 1$ is a good approximation.

For $t_{eq} < t < t_{rec}$ and $\lambda_J < R_H$ the matter is the dominant component, in particular the dark matter:

$$\rho \sim \rho_M \quad \xrightarrow{w=0} \quad \delta \simeq \delta_M(t) \propto a \propto t^{\frac{2}{3}}$$

$$\begin{array}{lll} \lambda > R_H & \Rightarrow & \delta_{DM} \propto \delta_R \propto \delta_b \left\{ \begin{array}{ll} \propto a & \Omega = 1 \\ > a & \Omega > 1 \\ < a & \Omega < 1 \end{array} \right. \\ \lambda_J < \lambda < R_H & \Rightarrow & \left\{ \begin{array}{l} \delta_{DM} \quad \left\{ \begin{array}{ll} \propto a & \Omega = 1 \\ > a & \Omega > 1 \\ < a & \Omega < 1 \end{array} \right. \\ \delta_R \propto \quad \delta_b \propto \textit{oscillating waves} \end{array} \right. \\ \lambda < \lambda_J & \Rightarrow & \delta_{DM} \propto \delta_R \propto \delta_b \propto \textit{oscillating waves} \end{array}$$

For $t > t_{rec}$ dark matter is still dominating:

$$\begin{array}{lll} \lambda > R_H & \Rightarrow & \delta_{DM} \propto \delta_R \propto \delta_b \\ \lambda_J < \lambda < R_H & \Rightarrow & \left\{ \begin{array}{ll} \delta_{DM} & \left\{ \begin{array}{ll} \propto a & \Omega = 1 \\ > a & \Omega > 1 \\ < a & \Omega < 1 \end{array} \right. \\ \delta_R \propto & \textit{oscillate and decay} \\ \delta_b \propto & \textit{accelerated increase, then} \propto \delta_{DM} \end{array} \right. \\ \lambda < \lambda_J & \Rightarrow & \delta_{DM} \quad \left\{ \begin{array}{l} \textit{cancelled by diffusion} \\ \textit{baryons have the same fate} \end{array} \right. \end{array}$$

1.2.3 Dark matter: hot or cold?

The time when a particle with a mass m_x becomes non-relativistic depends on the relation:

$$KT(a_{nr}) = m_x c^2 \tag{1.57}$$

on the base of z_{nr}, when the transition from relativistic regime to the non-relativistic one of a particle happens, we can define, respect to z_{dec}, two kind of dark matter particles: the *Hot Dark Matter* and the *Cold Dark Matter*[9]. For the HDM particles this transition had place after the decoupling from radiation $a_{nr} > a_{dec}$ and from the equation 1.57 we can deduce that are particles with very low masses; for the CDM particles the passage to the non-relativistic regime happened before the decoupling, $a_{nr} < a_{dec}$ and they are high mass particles.

If we calculate the Jeans mass for each type of particles we obtain: for the HDM at the equivalence $M_{J,HDM}(t_{eq}) \sim 10^{15}\Omega_{DM}h^{-2}M_{\odot}$, for the CDM at the same time: $M_{J,CDM}(t_{eq}) \sim 10^5 - 10^6 M_{\odot}$, while for the bayons the Jeans mass at the decoupling is $M_{J,b}(t_{dec}) \sim 10^{16}M_{\odot}$.
This means that if at the equivalence the HDM dominates, the scenario of the cosmic structures formation is *top-down*, the big structures are the first to be formed and only after they are subjected to fragmentation; if the CDM dominates the scenario is *bottom-up* or *hierarchical*, in this case small structures are formed, and later under the action of gravity, they group in the bigger structures; if in the Universe there were only baryons, the scenario should be top-down.

Present scenario

We need only 10 parameters to describe expansion, geometry, age and composition of the Universe.
These parameters are derived from observations, in particular in the table 1.2 are included values coming from the data collected during the 7 years observations of the *Wilkinson Microwave Anisotropy Probe*[10] mission.
In the table 1.2 are also reported the theoretical prediction of the ΛCDM model on the values of the same parameters, we can note that theoretical and observative data are in a quite good agreement.
At the moment the simplest model, in agreement with the observations, capable to explicate the CMB and to predict a Universe with an accelerated expansion is the ΛCDM model, and this implies a hierarchical structures formation.

---

[9] Here and after we refer to them as HDM and CDM, respectively

[10] Here and after we refer to it as WMAP.

Parameter		*Value*[a]	WMAP[b]
age of the Universe	t_0	13 ± 1.5 Gyr	13.75 ± 0.13 Gyr
Hubble constant	H_0		71.0 ± 2.5 km/sec/Mpc
deceleration parameter	q_0	-0.67 ± 0.25	-0.66 ± 0.1
the temperature of the CMB	T_0	2.725 ± 0.001 K	
density parameter	Ω_0	1.03 ± 0.03	$1.08^{+0.093}_{-0.071}$
baryonic density	$\Omega_{\rm b}$	0.039 ± 0.008	0.0449 ± 0.0028
CDM *density*	Ω_{CDM}	0.29 ± 0.04	0.222 ± 0.026
massive neutrinos density	Ω_ν	$0.001 - 0.05$	
dark energy density	Ω_Λ	0.67 ± 0.06	0.734 ± 0.029
state equation of Λ	w	-1 ± 0.2	$-1.12^{+0.42}_{-0.43}$

Table 1.2: Cosmological parameter at present time, from Freedman and Turner (2003)[a] and Jarosik et al. (2011)[b].

1.2.4 Power spectrum

The matter distribution in the Universe is determined by the fluctuations growing up phenomena and these are stochastic processes. Unfortunately, we can not proceed in a statistical analysis[11] of the Universe to know how the matter is distributed; consequently we assume the *ergodic principle*: *the average on a sample can be substituted by averages made on regions of the sample itself*, under the hypotheses that the examined regions are big enough, adequately representative and not overlapping.

The ergodic principle is a theorem in the case of a Gaussian distribution and for stochastic fluctuations on sufficiently big scale, the assumption of gaussianity is a good approximation.

We define the Gaussian stochastic field δ, decomposing it in waves in the Fourier space:

$$\delta(\vec{x}) = \frac{1}{(2\pi)^3} \int \hat{\delta}(\vec{k}) e^{(i\vec{k}\cdot\vec{x})} d^3k, \tag{1.58}$$

$$\hat{\delta}(\vec{k}) = \int \delta(\vec{x}) e^{(-i\vec{k}\cdot\vec{x})} d^3x. \tag{1.59}$$

---

[11] In order to make a statistical analysis of a certain phenomenon we need several representations of the same phenomenon.

We define the *two point correlation function*, $\xi(\vec{r})$, as the measure of how much the density field δ is correlated on a given scale r, or, in other words, the probability to find two objects inside a given distance $\vec{r}$:

$$\xi(\vec{r}) =< \delta(\vec{x})\delta(\vec{x}+\vec{r}) > . \tag{1.60}$$

We define the *power spectrum* $P(k)$ the measure of how big are the mean quadratic fluctuations of the density field:

$$< \hat{\delta}(\vec{k})\hat{\delta}(\vec{k'}) >= (2\pi)^3 P(k)\delta_d^{(3)}(k+k'), \tag{1.61}$$

where $\hat{\delta}$ is the perturbation in the Fourier space.
Substituting the 1.61 in the 1.60 we obtain the result known as *Wiener-Khintchine theorem*:

$$\xi(\vec{r}) = \frac{1}{(2\pi)^3}\int d^3k P(k) e^{(i\vec{k}\cdot\vec{r})}, \tag{1.62}$$

from which we can deduce that the correlation function is the inverse Fourier transform of the power spectrum and this ensures that the two quantity are totally equivalent.

The value of $P(k)$ for each k measures how much the contribution of the perturbations on scale k is important in the Fourier integral to form the generic perturbation $\delta(\vec{x})$ in the configuration space.
The spectrum is then a measure of the power density of a fluctuation on the scale k. The power will be given by $P(k)d^3k$.
It is common to assume for the primordial power spectrum a functional form with a power law:

$$P(k) = A_p k^{n_p}, \tag{1.63}$$

where A_p is the amplitude and n_p is called *spectral index*.
The spectra described by power laws are also-called *scale-free* because their logarithmic slope is constant on all scales and so they do not depend on any of them in particular; in addition to this the inflationary model predicts fluctuations with a power law spectrum.

A Gaussian distribution is fully characterized by its variance, due to the fact that the mean value is zero, so we have that:

$$\sigma^2 \equiv< \delta^2(\vec{x}) > - < \delta(\vec{x}) >^2 =< \delta^2(\vec{x}) > . \tag{1.64}$$

Assuming the ergodic principle, reason why volumes V_∞ that are adequately big and not overlapping can be considered independent realization of the Universe itself, we make a spatial average on each volume and at least we make a statistical average among these values. In this way the equation 1.64 becomes:

$$\sigma^2 = \frac{1}{V_\infty} \int d^3x < \delta^2(\vec{x}) >; \tag{1.65}$$

for the *Parseval relation*[12] the variance 1.65 can be written as:

$$\begin{aligned} \sigma^2 &= \frac{1}{V_\infty} \frac{1}{(2\pi)^3} \int d^3k < \delta(k)\delta^*(k) >= \\ &= \frac{1}{(2\pi)^3} \int d^3k P(k) = \\ &= \frac{1}{2\pi^2} \int_0^\infty dk P(k) k^2. \end{aligned} \tag{1.66}$$

The second equivalence directly derives from the definition of $P(k)$, equation 1.61, while in the last one we used the isotropic condition.

In reality the estimation of $\delta = \delta\rho/\rho$ for each point of the space is not simple at all; that is why we use the mean density fluctuation in a given volume V: $\delta_M = \delta M/M \equiv \delta(\vec{x}) * w(\vec{x}, R)$, with $w(\vec{x}, R)$ as window function[13], and, substituting it in the equation 1.66, we obtain the *mass variance*, σ_M^2:

$$\sigma_M^2 \propto \int_0^\infty dk\, k^2 P(k) \tilde{w}^2(k, R). \tag{1.67}$$

If $R \to 0$ the window function tends to the Dirac delta function and $\sigma_M^2 \to \sigma^2$.

The linear theory asserts that the perturbations increase in time proportionally to $\delta_+(t)$ called *growing factor* and the power spectrum evolution derive from the evolution of the perturbation:

$$\begin{aligned} \delta(\vec{x}, t) &= \delta(\vec{x}, t_0)\delta_+(t), && (1.68) \\ P(k, t) &= P(k, t_0)\delta_+^2(t). && (1.69) \end{aligned}$$

---

[12] The Parseval relation says that the integral of two functions extended to the configurations space is equal to the integral of their Fourier transform extended to the wavenumber space:

$$\int_{-\infty}^{+\infty} f(x) g^*(x) dx = \frac{1}{2\pi} \int_{-\infty}^{+\infty} \hat{f}(k) \hat{g}^*(k) dk.$$

[13] The window function centered in $\vec{x}$ acts like a filter of the mass distribution on a radius equal to R.

At this point we can substitute in the equation 1.67 the power law 1.63 and the power spectrum evolution 1.69,

$$\sigma_M^2 \propto \int_0^\infty dk\, k^{n+2}\tilde{w}^2(k,R) \propto \delta_+^2(t)k^{n+3}. \tag{1.70}$$

Knowing that the wavenumber k is dimensionally the inverse of a length and that the mass is proportional to the third power of a length, we can rewrite the equation 1.70:

$$\sigma_M^2 \propto \delta_+^2(t)M^{-\frac{n+3}{3}}; \tag{1.71}$$

and we can derive some non-linear scale laws, which are valid when $\delta \gtrsim 1$. These laws allow us to put limits on the primordial spectral index.

If $\delta = 1$ then also $\sigma_M^2 \sim 1$, and it is the reason why, assuming to be in a Einstein-De Sitter Universe, $\delta_+(t) \propto a(t)$:

$$M_* \propto a(t)^{\frac{6}{3+n}}, \tag{1.72}$$

this is the mass formed when the non-linearity starts. From this we can derive the typical time 1.73a when a structure with a given mass forms and the virialization temperature object from the quadratic mean velocity 1.73b:

$$t_* \propto M_*^{\frac{3+n}{4}}, \tag{1.73a}$$

$$< v^2 >_* \propto M_*^{\frac{1-n}{6}}. \tag{1.73b}$$

If we impose that the structures formation is hierarchical, t_* has to be a crescent function of M_*: $n > -3$. In addition to this the energy has to be related to the collapse of the structure, so it has to be a crescent function of M_*: $n < 1$. Hence a bottom-up scenario requires a spectral index $-3 < n < 1$.

The *Zel'dovich spectrum* is a particular power spectrum where the spectral index is 1 and it is the prediction of the simplest inflationary model. Its main property is that the potential fluctuations are constant for each scale.

But we would like to know how the perturbations spectrum evolves before and after the entrance in the horizon. Because R_H is a crescent function of the time, the first scales to entry in the horizon are the smallest ones and they are also those which are affected for the longest time by the stagnation, till $t = t_{eq}$, therefore the spectrum is deformed. The mass contained in the horizon radius $M_H = \rho_H R_H^3 = \rho_H k_H^{-3}$ is for $t < t_{eq}$ proportional to $a(t)^3$ and for $t > t_{eq}$ proportional to $a(t)^{3/2}$.

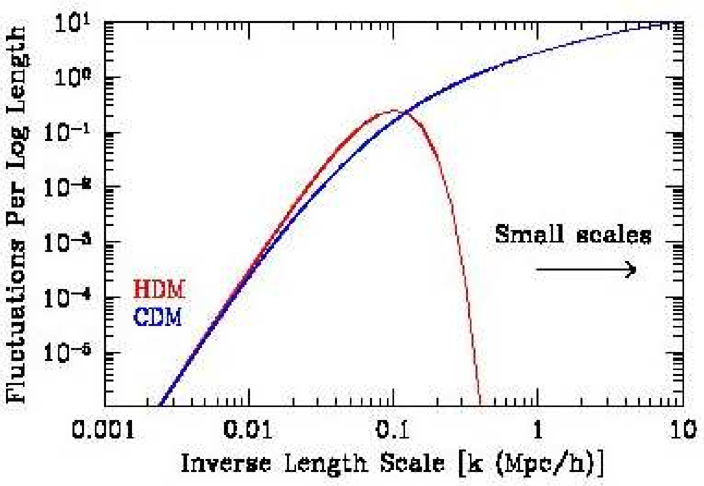

Figure 1.6: Power spectrum of the cold dark matter compared to the hot dark matter one. We note that the *free-streaming* damps the power on the small scales. Image from Supercluster; http://universe-review.ca/F03-supercluster.htm.

Pointing out on the CDM power spectrum shown in the figure 1.6, for which M_J is small, we consider a perturbation on a scale k such that the entry in the horizon happens before the equivalence, $a_H < a_{eq}$. The perturbation will grow up till this entrance and then it will be affected by the stagnation till the equivalence:

$$\delta(k, a_{eq}) = \delta(k, a_{in}) \left(\frac{a_H}{a_{in}} \right)^2 \propto \delta(k, a_{in}) a_H^2 \propto \delta(k, a_{in}) k^{-2}. \tag{1.74}$$

Instead a perturbation on a scale k that enter in the horizon after the equivalence does not suffer the stagnation, and its evolution will be:

$$\delta(k, a_{eq}) = \delta(k, a_{in}) \left(\frac{a_{eq}}{a_{in}} \right)^2 \propto \delta(k, a_{in}). \tag{1.75}$$

Consequently the spectrum at the equivalence of the perturbation which is subjected to the stagnation will be:

$$P(k, a_{eq}) \propto \delta^2(k, a_{eq}) \propto \delta^2(k, a_{in}) k^{-4} \propto P(k, a_{in}) k^{-4} \propto k^{n-4}; \tag{1.76}$$

while the spectrum of the perturbation on large scale will remain almost proportional to the primordial spectrum:

$$P(k, a_{eq}) \propto P(k, a_{in}) \propto k^n. \tag{1.77}$$

This can be translated in the change of the slope of the primordial spectrum when the scale $k_{eq} \sim R_H^{-1}(a_{eq})$ enters in the horizon at the equivalence.
For all those reasons we introduce a transferring function T_{CDM}. It measures how much of the primordial signal is transferred at the equivalence in a CDM dominant scenario:

$$P_{eq} = P_{in} T_{CDM}^2 \Longrightarrow T_{CDM} \begin{cases} \propto 1 & k \to 0 \\ \propto k^{-2} & k \to \infty \end{cases} \tag{1.78}$$

In the figure 1.6 the spectra of the two different kind of dark matter are compared: it is evident that they have different transferring function.
From the power spectrum we can infer on the values of several cosmological parameters. In fact in a closed Universe R_H is bigger, consequently k_{eq} is smaller and the transition will happen on bigger scales R; conversely if the Universe is open R_H decreases, k_{eq} increases and the change of the spectrum slope will happen on smaller scales R.

1.2.5 Zel'dovich approximation

The non-linear regime starts when the overdensity reaches the value $\delta = 1.686$: in this case the examined object is collapsed. But, while the linear regime is easy to treat, because it does not change the Gaussian distribution of the fluctuations, the non-linear one can be correctly treated only through numerical simulation.

However an approximated solution exists: the *weakly non-linear regime* or *Zel'dovich approximation* that is true for $\delta > 1$ but small.
We assume that, given a particle distribution, the final position of a particle subjected to the gravitational field is:

$$\vec{r}(\vec{q}, t) = a(t)\vec{q} + F(\vec{q}, t); \tag{1.79}$$

$\vec{r}$ is the Eulerian position and $\vec{q}$ is the Lagrangian position. We suppose that $F(\vec{q}, t)$ is separable in its variables:

$$F(\vec{q}, t) = f(t)G(\vec{q}). \tag{1.80}$$

By substituting the equation 1.80 in the 1.79 we obtain:

$$\vec{r}(\vec{q},t) = a(t)\vec{q} + f(t)G(\vec{q}); \tag{1.81}$$

and imposing

$$f(t) = a(t)\delta_+(t) \quad \textit{and} \quad G(\vec{q}) = -\nabla_q \Phi_0(\vec{q}), \tag{1.82}$$

where $\delta_+(t)$ is the growing factor of the perturbations discussed before, and $\Phi_0(\vec{q})$ is the peculiar velocity potential; we have:

$$\vec{r}(\vec{q},t) = a(t)\Big[\vec{q} - \delta_+(t)\nabla_q \Phi_0(\vec{q})\Big]; \tag{1.83}$$

from which we can calculate the velocity:

$$\vec{v} = \frac{d\vec{r}}{dt} - H(t)\vec{r} = -a(t)\,\dot{\delta}_+(t)\nabla_q \Phi_0(\vec{q}). \tag{1.84}$$

The evolution is fixed by the initial conditions.

We can calculate the density by imposing $x = r/a$:

$$dM = \rho_0 d^3q = \rho(x,t)d^3x, \tag{1.85a}$$

$$\rho(x,t) = \rho_0 \frac{d^3q}{d^3x}. \tag{1.85b}$$

In the 1.85a the second equivalence is valid because the mass is conserved during the transformation from the Lagrangian space to the Eulerian one and in the 1.85b the factor $\frac{d^3q}{d^3x}$ is the measure of how much the Lagrangian volume changes respect to the Eulerian one. The variation can be rewritten as:

$$\begin{aligned} \frac{dV_{eul}}{dV_{lag}} &= \frac{d^3x}{d^3q} = J\Big[\frac{\partial x}{\partial q}\Big] = a^3\Big[\delta_{ij} - \delta_+(t)\frac{\partial^2\Phi_0}{\partial q_i \partial q_j}\Big] = \\ &= a^3\big[1 - \delta_+(t)\lambda_1(q)\big]\big[1 - \delta_+(t)\lambda_2(q)\big]\big[1 - \delta_+(t)\lambda_3(q)\big]. \end{aligned} \tag{1.86}$$

$\frac{\partial^2\Phi_0}{\partial q_i \partial q_j}$ is the *deformation tensor* that measures how much the space is modified and, once diagonalized, $\lambda_1(q)$, $\lambda_2(q)$ and $\lambda_3(q)$ are its eigenvalues.

If we substitute the 1.86 in the equation 1.85b we obtain the density evolution:

$$\rho(x,t) = \frac{\rho_0}{a^3}\big[1 - \delta_+(t)\lambda_1(q)\big]^{-1}\big[1 - \delta_+(t)\lambda_2(q)\big]^{-1}\big[1 - \delta_+(t)\lambda_3(q)\big]^{-1}. \tag{1.87}$$

From the equation 1.87 we can infer that if $\lambda_1 < \lambda_2 < \lambda_3$ and $\lambda_i < 0$ then $\rho(x,t)$ decreases and there is an expansion; if $\lambda_1 < \lambda_2 < \lambda_3$ and $\lambda_i > 0$,

there are some values that put the denominator to zero and $\rho \to \infty$, hence the collapse starts. The collapse happens on all directions, but the one which corresponding at the higher eigenvalue is the first. In the other cases we have: if $\lambda_1, \lambda_2 < 0$ and $\lambda_3 > 0$ the collapse happens along one direction and planar structures are formed; if $\lambda_1, \lambda_2 > 0$ and $\lambda_3 < 0$ the collapse happens along two directions and filamentary structures are formed.
For a Gaussian distribution the probability to have one of this solutions is: 8% for each solution with concordant signs and 42% for each solution with almost one non concordant sign.

If we take the expansion in series for very small t, this solution is reduced to the linear regime. In this approximation the *shell crossing* problem can arise, because we do not take care about the possibility that the particles orbits can cross each others. We can neglect this problem considering the second order terms in the expansion.

Chapter 2

Galaxy clusters

The clusters of galaxies are the biggest gravitationally bound system and, in a hierarchical scenario, this means that they are also the youngest structures in the Universe. In fact the bottom-up model says that from the density fluctuations of the early Universe a gravitational collapse began, which led to the formation of more and more massive structures until the galaxy clusters at present time.

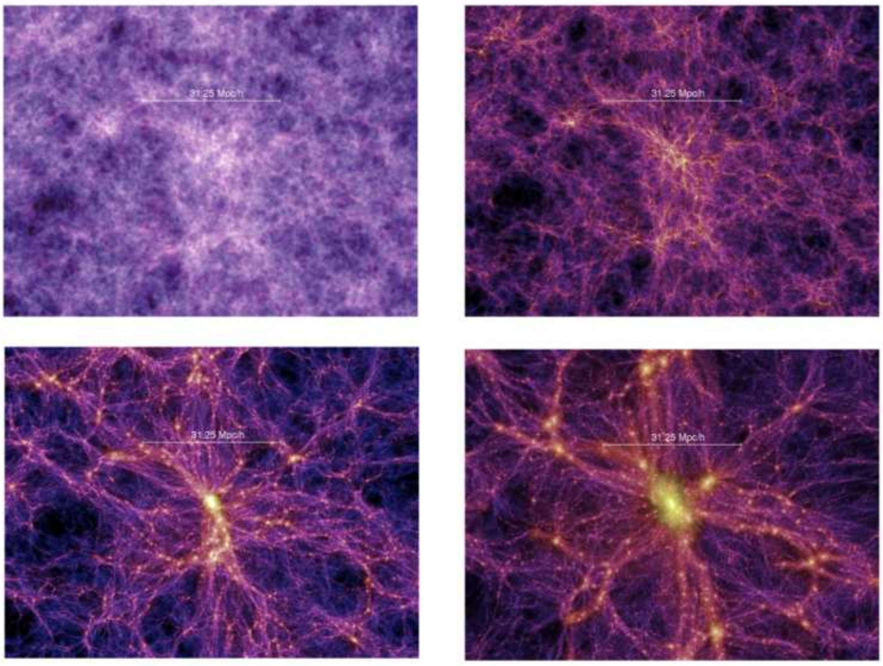

Figure 2.1: In this figure it is shown the evolution of a density field at different redshift; from the isotropic, stochastic dark matter distribution to the formation of a central cluster, high density region, and of the filaments, less dense regions. Image from Millennium Simulation Project; http://www.mpa-garching.mpg.de/galform/virgo/millennium/.

They are located at the nodes of the cosmic web, where filaments intersect. For example, we can see in figure 2.1 some snapshots extracted from the cosmological numerical simulation *Millennium run*[1], of 2005, based on the ΛCDM model and on the WMAP-1 dataset; the simulation followed the evolution of more of 10^{10} particles in a box with dimension of $L = 500$ Mpc and with a force resolution of $\varepsilon = 5$ kpc.

Because the mass fraction of clusters, as we can see in the table 2.1, is comparable to the universal content, they can be treated as ideal laboratory to check the theory predictions on galaxy evolution.

Components	Mass Fraction	Energy band
Galaxies	1-5 %	Visible band
Hot Gas	9-10 %	X-ray band
Dark matter	85-90 %	Not visible

Table 2.1: Main components in a cluster in order of abundance.

2.1 Physical characteristics

Clusters are extended over a radius of 1-2 Mpc and their virial mass is ranging approximately from $\sim 10^{14}$ to 10^{15} $M_\odot$. They collect from hundreds to thousands of galaxies interacting in the dark matter potential well and the velocity dispersion of galaxies is $\sigma \sim 1000$ km sec^{-1} . The potential well of a cluster is so deep that clusters can be considered as closed boxes.

The distribution of galaxies in a cluster shows that going towards the center the number of early type increases and the number of late type decreases, this is called the *morphology-density relation.* The fraction of galaxies of different morphological types in a region depends on the density of the environment: the population of early type galaxies, like E and S0 dominates rich environments. The *Brightest Cluster Galaxy*[2] is in general an elliptical giant galaxy, which lies

---

[1] The Millennium run simulated the Universe till the present time in order to trace the matter distribution evolution. It was possible to recreate the evolution history of galaxies, which populated the big volume of the simulation, and of the super massive black holes, which occasionally gave origin to quasars. By comparison of the simulated data with observations we could investigate on the physical processes responsible of the formation of galaxies and more in general of the cosmic web.

[2] Here and after BCG.

close to kinematical and geometric center of the host cluster, in other words at the bottom of the dark matter potential well.

In addition, the clusters are filled by hot gas, the *Intra Cluster Medium*[3], at temperature of $T_X \sim$ 3-10 keV that corresponds to $T_X \sim 10^7$-10^8 K, with a density if 10^{-3} atoms cm^{-3}. The ICM is a totally ionized plasma with traces of metals $z \sim 0.37\ z_\odot$ that emits, for $KT > 2$ keV, via *bremsstrahlung* a luminosity $L_X \sim 10^{44-45}$ erg sec^{-1}.

Bremsstrahlung

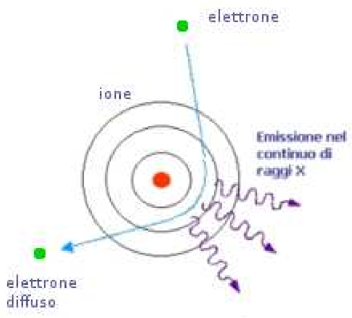

Figure 2.2: Simple sketch of the X-ray production process through bremsstrahlung.

The bremsstrahlung, or deceleration radiation, is a typical process in a highly ionized plasma during which a dynamical scattering happens between an ion or an atomic nucleus and a free electron. The electron, subjected to the electromagnetic field of the ion, deviates from its trajectory and during the acceleration emits radiation.
The emissivity of the process, expressed in unit of erg cm^{-3} sec^{-1}, depends on the second power of the density:

$$\epsilon_{ff} = 1.4 \times 10^{-27} T^{1/2} n_e n_i Z^2 g, \qquad (2.1)$$

n_e and n_i are respectively the electronic density and the ionic density, Z is the nuclear charge of the ions and g is the Gaunt factor.

In the figure 2.2 a simplification of the phenomenon is shown. For temperatures $KT < 2$ keV the X-ray spectrum is emission lines dominated. From the spectrum in the X band it is possible to extract the metallicity z of the gas. It is not uniform, it increases from outside to inside. Hot clusters are more massive and show high α/Fe ratio due to the enrichment of the SNII. Cold clusters are less massive and show a low α/Fe ratio because the enrichment is due to SNIa.

---

[3] Here and after ICM.

2.1.1 Luminosity function

The luminosity of galaxies in a cluster ranges over a wide interval, there are till seven order of magnitude of difference between the BCG and the faintest galaxy. The *Luminosity function*[4], providing information about the formation and the evolution of galaxies and about the evolution of luminosity as a function of redshift, is a useful tool to test cosmological models. It is also strictly related with the mass function, because we can always switch from luminosity to mass and vice versa.

The LF counts the number density of galaxies per luminosity interval. The analytical form was suggested by Schechter (1976), in order to give a parametric description of observed luminosities:

$$\phi(L)dL = n_* \left(\frac{L}{L_*}\right)^{\alpha} exp\left(-\frac{L}{L_*}\right) d\left(\frac{L}{L*}\right). \qquad (2.2)$$

Here L_* is the characteristic luminosity where the function change its slope and the power-law form cuts off, n$_*$ is the number density of galaxies for $L = L_*$ and provides the normalization, α is the slope of the LF.

The function has two different trend: a power law with negative slope which dominates for $L < L_*$ and an exponential cut off for $L > L_*$, thus for low luminosities the function increases as L decreases, while higher is the luminosity and more rare is the galaxy.

The LF evolves, in fact looking back in time the typical luminosity of galaxies grows up, while looking forward in time the number of low luminosity galaxies increases, these are the reason why with the passing of time the LF shifts on lower luminosities and increases the number of galaxies with low L.

The derivation of the LF requires the accurate measurements of the distance of the galaxies in order to know their absolute magnitude; for clusters, assuming that all galaxies have approximately the same distance, we can take into account only the mean cluster redshift.

2.1.2 Sunyaev-Zel'dovich effect

After the recombination the Universe is neutral, but observations at high redshift show that the ICM at $z \sim 5$ is totally ionized, because we do not observe the *Gunn-Peterson effect*. The Gunn-Peterson trough is a feature of

---

[4] Here and after LF.

the spectra of quasars due to the neutral hydrogen; it is a suppression of the electromagnetic emission of quasars at wavelength less than that of the $Ly\alpha$ line at the redshift of the quasar. The absence of this effect shows that in an epoch between $z = 1000$ and $z = 5$ the Universe has been subjected to a global *reionization*. The reionization can happen on a local scale and interests limited regions of the Universe like clusters of galaxies.

In a reionized Universe photons can be influenced by the velocity and the overdensity of baryons, and the anisotropies of temperature can be deleted or created. This is what we call *Sunyaev-Zel'dovich effect*[5]: thermal and kinematic, (Sunyaev and Zeldovich, 1980).

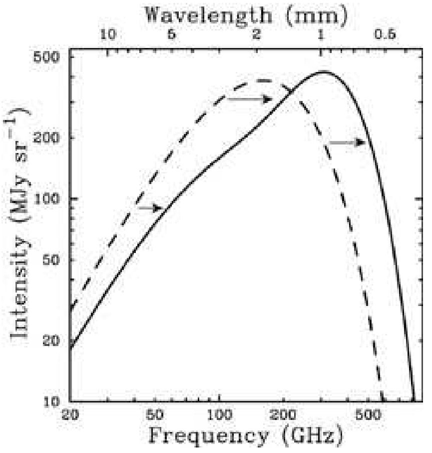

Figure 2.3: Because the SZE is a very small effect ($\leq$ 1 mK), in this plot it is shown the SZE spectral distortion for a mock cluster that is over 1000 times more massive than a typical cluster. The dashed line belongs to the undistorted CMB spectrum, while the solid line refers to the distorted one, (Reese, 2004).

The kinematic effect is due to the peculiar velocity along the line of sight, v_{pec}, of the cluster; the Compton effect on the CMB's photons shifts their energy to red or blue on the basis of the fact that the cluster is approaching or moving away.

$$\frac{\Delta T_{SZE}}{T_{CMB}} \propto -\left(\frac{v_{pec}}{c}\right). \tag{2.3}$$

The thermal effect is independent of the cluster velocity. The photons of the CMB are scattered by the inverse Compton effect due to a distribution of relativistic electrons in the hot gas. The black body spectrum is shifted to highest energies and this appears like a decreasing of photons temperature at low frequency $\leq$ 218 GHz and a correspondent increasing of the photon temperature at high frequency, as we can see in figure 2.3. The thermal SZE is ten times higher than the kinematic SZE.

---

[5] Here and after SZE.

The SZE originates a distortion at dimensionless frequency $x \equiv \frac{h\nu}{KT_{CMB}}$ proportional to the density n_e and the temperature of the gas T_e:

$$\frac{\Delta T_{SZE}}{T_{CMB}} = f(x)y = f(x)\int n_e \frac{kT_e}{m_e c^2}\sigma_T dl. \tag{2.4}$$

Here y is the so-called *Compton y-parameter*, which is proportional to the optical depth and to the fractional energy gain per scattering, and the integration is along the line of sight. In $f(x)$ there is the frequency dependence and it takes into account of the relativistic correction.
The SZE does not depend on the redshift.

Using the different dependence from density of SZE and of the X-brightness, S_X, we can directly derive the linear dimension of the cluster:

$$r_c \propto \frac{\left(\Delta T_{SZE}/T_{CMB}\right)^2}{S_x} \tag{2.5}$$

From the dimension of the cluster we can calculate the angular distance $D_A = \frac{r_c}{\theta_c}$ and, measuring the redshift z from the galaxies members of the cluster, we can infer the values of the cosmological parameters as the Hubble constant and the deceleration parameter:

$$D_A = D_A(H_0, q_0, z) = \frac{c}{H_0 q_0^2}\frac{q_0 z + (q_0 - 1)(\sqrt{1 - 2q_0 z} - 1)}{(1+z)^2}. \tag{2.6}$$

2.2 Mass estimates

The total mass of a cluster can be estimated by using different techniques that belong to the different properties of the components of cluster in different energy bands, we will qualitatively discuss the methods in the following subsections.

In figures 2.4 and 2.5 we have two clusters, respectively *Abell* 2199 and the *Bullet cluster* shown in different bands. It is easy to notice that using only the baryonic component as a mass tracer leads to a misunderstanding of the mass distribution in clusters, and that is better to use the several techniques as complementary.
In particular, in the figure 2.5, we can note that the bullet-shaped cloud of gas marked in pink at the right has been warped during the impact between

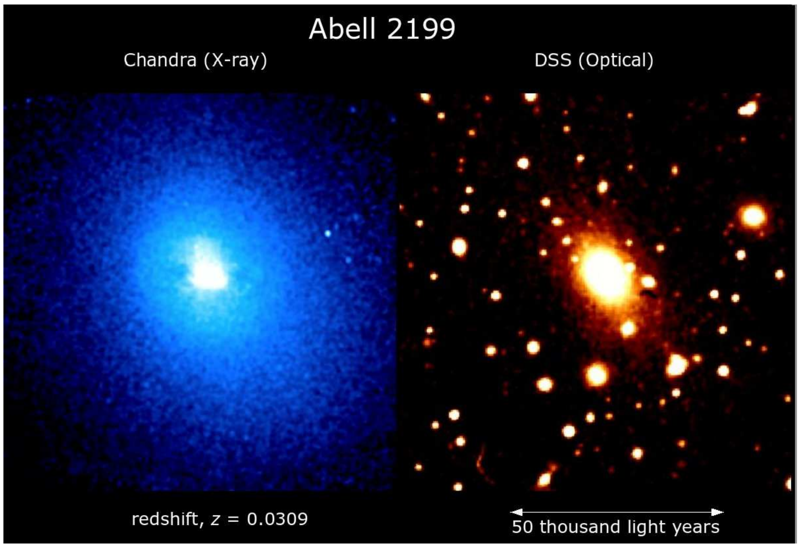

Figure 2.4: In this image *Abell* 2199 we can see a comparison between an X-ray image from Chandra (on the left side of the panel), showing the ICM emission, and an optical Digitized Sky Survey (DSS) image (on the right), in which only the galaxies are visible.

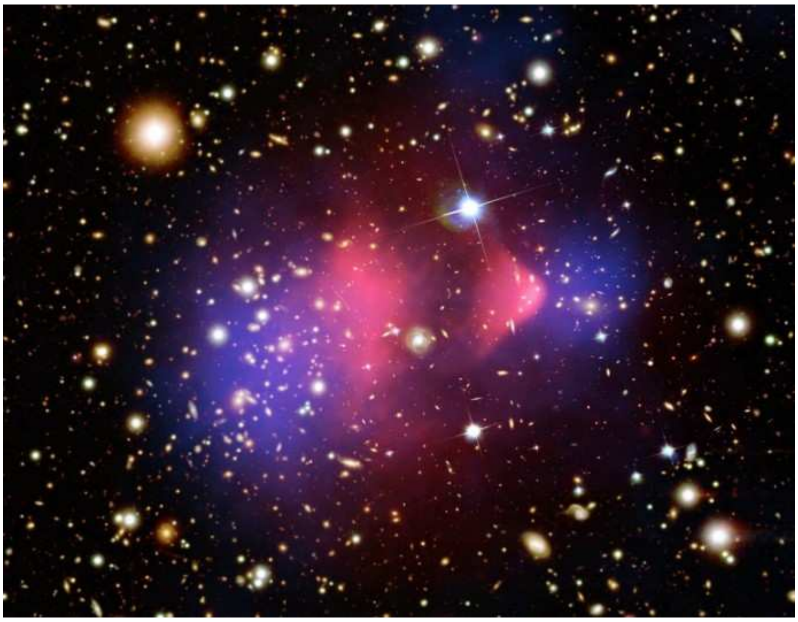

Figure 2.5: The image of the *Bullet cluster* is a composition of different images that shows the contribution of different components. The optical data belongs to galaxies and the X-ray data relates to the hot gas, in the image their distribution is underlined in pink. Instead the blue hues show the distribution of dark matter, the mapping has been done through lensing observations, (Markevitch, 2006; Clowe et al., 2006).

two galaxy clusters that created the larger bullet cluster itself. The different distribution of the dark matter, coloured in blue, respect to the gas shows that the only interaction between them was by gravity, thus this is considered a direct proof of the dark matter existence, (Clowe et al., 2006).

2.2.1 Dynamical mass

We can use the dynamics of the members of the cluster, that are observable in the visible band. Assuming that the clusters are virialized objects, we can write the *Virial theorem*:

$$< T >= -\frac{1}{2} < U >, \tag{2.7}$$

where T is the total kinetic energy and U is the gravitational potential energy both averaged on time, and the observed velocity distribution of galaxies in cluster can be converted into a mass estimate:

$$M \sim \frac{\sigma_v^2 R_{vir}}{G}, \tag{2.8}$$

where σ_v is the line of sight velocity dispersion and R_{vir} is the virialization radius which is determined from the positions of galaxies recognized as members of the cluster by redshift.
This derivation suffers both the virialization assumption and the contamination of the galaxies sample by galaxies that are on the line of sight but do not belong to the cluster, leading to an overestimation of the mass.

2.2.2 X-ray mass

The ICM, as visible through its bremsstrahlung in X-rays, traces the gravitational potential of the cluster. Assuming the hydrostatic equilibrium:

$$P = \frac{K\rho T}{\mu m_H} \qquad and \qquad \frac{dP}{dr} = -\frac{GM\rho}{r^2}, \tag{2.9}$$

the mass is given by

$$M(r) = \frac{K}{\mu m_H G} T_r \left(\frac{dlnT}{dlnr} + \frac{dln\rho}{dlnr} \right). \tag{2.10}$$

If we assume for the density profile a β-model for which $\rho_{gas} \propto \rho_{dm}^{\beta}$, then

$$\rho_{gas}(r) = \rho_{gas,0} \left[1 + \left(\frac{r}{r_c} \right)^2 \right]^{-\frac{3\beta}{2}} \tag{2.11}$$

Using the density profile derived from the β-model and considering $T = cost$, we can write the mass as:

$$M(r) = \frac{3K\beta}{\mu m_H G} T \frac{x^2}{1+x^2} r. \tag{2.12}$$

Considering instead that the gas is polytropic, $T \propto \rho^{\gamma-1}$, the mass becomes

$$M(r) = \frac{3K\gamma\beta}{\mu m_H G} T \frac{x^2}{1+x^2} r. \tag{2.13}$$

We can extract the density profile $\frac{d\rho}{dr}$ from the image in the X-ray band: we examine concentric rings on the image and how much the surface brightness changes. This is sensitive to the gas density and so we can use the surface brightness profile of the image X as a fit for the density profile; for the temperature profile $\frac{dT}{dr}$ we analyze the X spectrum at a different temperatures corresponding to the different regions of the cluster from which we can estimate the temperature. Also this technique has problems related to the fact that we have to assume the equilibrium.

2.2.3 Lensing mass

Because clusters are the most massive object in the Universe, they act as very efficient gravitational lenses. Light coming from distant sources travel along paths that are distorted by the strong gravitational field related to the mass of the clusters. Both the different regimes strong and weak probe the projected mass distribution of the clusters at different radii, with strong lensing connected to the inner region, whereas weak lensing can yield mass measurements for larger radii. In addition to this the gravitational lensing does not rely on dynamical and equilibrium assumptions, reducing the bias on the mass estimate.

2.3 Some numerical results on dark matter properties in clusters

Galaxy clusters are a good tool to probe the properties of dark matter.
As we said before, halos are formed hierarchically due to the gravitational instability of the dark matter density fluctuations. Small systems form before and merge in order to form bigger objects. Thus the cluster halos are still experiencing the formation process and their density profile are dominated by

dark matter, in fact the cooling due to gas does not have the time to be efficient and to compress the halo.

The formation history tightly depends in the environment in which the halo grows up. This is the reason why virialized structure with the same final mass could have experimented different formation channel, and this has a great impact on the properties of the halo.
We would like to summarize the properties of the dark matter component in a halo derived from simulations.

2.3.1 Mass distribution

Halos, dominated by cold dark matter, are expected to have a universal density profile well described by a two parameter function called *Navarro-Frenk-White profile*[6], ρ_{NFW} (Navarro et al., 1996), and data coming from lensing are in good agreement with it. The NFW density profile is:

$$\rho_{NFW}(r) = \frac{\rho_s}{\frac{r}{r_s}\left(1+\frac{r}{r_s}\right)^2}, \tag{2.14}$$

where r_s is the scale radius, ρ_s is the density of the dark matter at the scale radius and they are two free parameters depending on the characteristics of each halo. In simulations of structure formation and the evolution of Universe, the NFW profile was found to be a good fit for a wide range of dark matter halo masses $[10^9 - 10^{15}]\,M_\odot$.
The integrated total mass is divergent and this is the reason why it is used to define the *virial radius*, R_{vir}, as the distance from the center of the halo that includes a fixed density contrast, Δ_{vir} that is the *virial overdensity*, and that is useful to be taken as the edge of the cluster[7]. The *virial mass*, M_{vir}, is then derived by the integration of the equation 2.14 from 0 to R_{vir} and it is related to cosmology in the following way:

$$M_{vir} = \int_0^{R_{vir}} dr\, 4\pi r^2 \rho_{NFW} \equiv \frac{4\pi}{3} R_{vir}^3 \frac{\Delta_{vir}}{\Omega_{\rm M}(z)} \Omega_0 \rho_c \tag{2.15}$$

where ρ_c is the critical density of the Universe and $\Omega_0 = \Omega(0)$ is the density parameter of the matter at the current time.

---

[6] Here and after we refer to it as NFW.

[7] In literature it is usual to find R_{200}, defined as the radius at which the average density within this radius is 200 times the critical density, this value is naturally related to a mass called M_{200}.

We define a new quantity the *concentration*, c_{vir}, as the ratio between the virial radius and the scale radius:

$$c_{vir} = \frac{R_{vir}}{r_s}. \tag{2.16}$$

using the definitions 2.15 and 2.16 we can express the scale density as a function of M_{vir} and c_{vir}:

$$\rho_s = \frac{M_{vir}}{4\pi r_s^3}\left[ln(1+c_{vir}) - \frac{c_{vir}}{1+c_{vir}}\right]^{-1}. \tag{2.17}$$

The concentration is in inverse relation with the host halo mass. Indeed, the collapse time of a dark matter halo depends on its mass and on the fact that the formation history is hierarchical: small systems collapse at higher redshift than the bigger ones, thus at a given redshift small halos have higher concentration than the bigger ones.

Zhao et al. (2009) performed a large number of high resolution N-body simulations with different structure formation models in order to investigate the mass accretion histories, the mass and redshift dependence of concentrations and the concentration evolution histories of dark matter halos. They derived an accurate and universal empirical *mass-concentration relation*:

$$c_{vir}(M_{vir}, z_L) = 4\left\{1 + \left[\frac{t(z_L)}{3.75\, t_{0.04}}\right]^{8.4}\right\}^{\frac{1}{8}}. \tag{2.18}$$

This relation describes the concentration of a given halo as a function of the time $t_{0.04}$, in which its main progenitor collected the 4% of its mass. But halos with the same mass at the same redshift, could have different concentration, due to the different formation histories experienced by such halos. Fixed the mass, the concentration distribution is fitted by a log-normal distribution function[8] with a variance $\sigma_{\ln c}$ that spans between 0.1 and 0.25.

Baryonic component effects

The contribution of the baryonic component to the density profile of a cluster becomes not negligible when its density approaches to the dark matter one and this is true for the inner region of the galaxy cluster.

The brightest central galaxy, residing in the halo center, can be very important in the strong lensing features (Meneghetti et al., 2003). Jaffe (1983) derived

---

[8] A log-normal distribution is a continuous probability distribution of a random variable whose logarithm is normally distributed: if X is log-normal distributed then $Y = log(X)$ is normal distributed.

from the the observation a function, equation 2.19a, useful to describe the mass density profile in ellipticals and in the bulge of spirals. Later, Hernquist (1990) proposed a new density profile, equation 2.19b, to avoid some deviations of the *Jaffe profile* from the $R^{1/4}$ law (de Vaucouleurs, 1948; Kormendy, 1977). These models can be used to describe the stellar component of the BCG:

$$\rho_{Jaf}(r) = \frac{\rho_{g,Jaf}}{\left(\frac{r}{r_g}\right)^2 \left(1+\frac{r}{r_g}\right)^2}, \tag{2.19a}$$

$$\rho_{Hern}(r) = \frac{\rho_{g,Hern}}{\frac{r}{r_g} \left(1+\frac{r}{r_g}\right)^3}. \tag{2.19b}$$

These profiles have a scale radius, r_g, related to effective radius, also called half-mass radius, R_e, by $r_g = 0.551\, R_e$, and R_e is derived from the virial radius as $R_e = 0.03R_{vir}$ (Keeton, 2001). The scale density can be calculated starting from the definition of the total mass:

$$\rho_{g,Jaf} = \frac{M_{Jaf}}{4\pi r_g^3}, \tag{2.20a}$$

$$\rho_{g,Hern} = \frac{M_{Hern}}{2\pi r_g^3}. \tag{2.20b}$$

They both go for larger radii as r^{-4}, while they differ in the inner region because the profile 2.19a has a steeper cusp than the profile 2.19b.

The dissipative baryonic component is able to perturb the dark matter distribution, in particular near to the host halo center. In fact, the baryonic infall contracts the distribution creating cores that are smaller and denser than would have evolved in absence of dissipation, (Blumenthal et al., 1986).

2.3.2 Geometry

Due the tidal interactions with the density field of the environment during the collapse, dark matter halos are not perfect sphere but triaxial (Sheth and Tormen, 2002). There is a correlation between the shape of the halo and its surroundings and it depends on the matter density parameter and on the typical collapse mass.

From a combined analysis of high-resolution halo simulations and large cosmological simulations Jing and Suto (2002) performed a statistical study

of halo shapes and they derived an accurate fitting formula to give a complete description of the triaxial density profiles of cold dark matter halos.
If we define a the minor axis, b the median axis and c the major axis, the distribution 2.21:

$$p(\lambda)d\lambda = \frac{1}{\sqrt{2\pi}\sigma_\lambda} \exp\left[-\frac{(\lambda - 0.54)^2}{2\sigma_\lambda}\right] d\lambda, \tag{2.21}$$

where $M_*(z_L)$ is the non linear mass at z_L, $\sigma_\lambda = 0.113$ and

$$\lambda = \left(\frac{a}{c}\right)\left(\frac{M_{vir}}{M_*(z_L)}\right)^{0.07\Omega(z_L)},$$

united with the conditional probability for the axial ratio:

$$p\left(\frac{a}{b}|\frac{a}{c}\right) = \begin{cases} \frac{3}{2(1-r_{min})}\left[1 - \left(\frac{2\frac{a}{b}-1-r_{min}}{1-r_{min}}\right)^2\right] & \frac{a}{b} \geq r_{min} \\ 0 & \frac{a}{b} < r_{min} \end{cases} \tag{2.22}$$

in which $r_{min} = 0.5$ if $\frac{a}{c} < 0.5$ and $r_{min} = \frac{a}{c}$ otherwise, gives us the empirical relation between the axial ratios $\frac{a}{c}$ and $\frac{a}{b}$.

2.3.3 Substructures

Halos show a great amount of substructures, representing the cores of accreted progenitor halos, thus they are not smooth objects (Ghigna et al., 1999; Gao et al., 2004).

As we stressed before, the different formation histories heavily affect the characteristics of a halo, as the number of substructures, and the different times scale on which the subhalos lose mass contribute to this. Hence, at the same redshift massive halos preserve more substructures than the less massive ones. In the same way, halos which have been formed later and have lower concentrations are more sub-structured, on the average, respect to more concentrated halos.
Giocoli et al. (2010) derived a fit of the mass function of subhalos:

$$\frac{1}{M_{vir}}\frac{dN(M_{vir}, c_{vir}, z_L)}{dm} = A(1+z_L)^{\frac{1}{2}}\frac{\bar{c}}{c_{vir}}m^\alpha \exp\left[-\beta\left(\frac{m}{M_{vir}}\right)^3\right], \tag{2.23}$$

in this expression $A = 9.33 \times 10^{-4}$, $\beta = 12.2715$, $\alpha = -0.9$ and $\bar{c}$ is the mean concentration of a halo with mass M_{vir} at redshift z_L.
The typical procedure to populate a halo with substructures of mass m_i is to

randomly sample the distribution 2.23 fixing a minimum mass m_{min} for the subhalos.

The density profiles of subhalos are modified by several causes: the interaction with the smooth component of the main halo, to the close encounters with other substructures, the gravitational heating and the dynamical friction. These events are responsible to the mass loss and can lead to the complete destruction of the substructure, (Choi et al., 2009). Those which survive have density profiles that are different to the NFW one because they are truncated at the tidal radius[9].

For example, we can consider the truncates singular isothermal sphere model of Keeton (2003):

$$\rho_{sub}(r) = \begin{cases} \frac{\sigma_v^2}{2\pi G r^2} & r \leq R_{sub} \\ 0 & r > R_{sub} \end{cases} \tag{2.24}$$

where σ_v^2 is the quadratic velocity dispersion and for R_{sub} we can use the definition of the mass of a subhalo by integrating the equation 2.24:

$$m_{sub} = \int_0^{R_{sub}} 4\pi r^2 \rho_{sub}(r) dr \quad \Rightarrow \quad R_{sub} = \frac{G m_{sub}}{2\sigma_v^2}. \tag{2.25}$$

The spatial distribution of subhalos follows the trend of the distribution of the smooth component. In any case, structures close to the center are easily disrupted by the tidal interactions and this is the reason why the distribution is less concentrated than the NFW profile of the host halo.

The spatial density cumulative distribution of the subhalos can be written as (Gao et al., 2004):

$$\frac{n(< x)}{N_{tot}} = \frac{(1 + \alpha' c_{vir}) x^{\beta'}}{(1 + \alpha' c_{vir} x^2)}. \tag{2.26}$$

In this expression we have: x, that is the distance from the center of the host halo in unit of the virial radius, N_{tot}, which is the total number of the subhalos, $\alpha' = 0.244$ and $\beta' = 2.75$.

To distribute the subhalos typically the distribution is randomly sampled, assigning the coordinates of the subhalos on a sphere.

---

[9] The tidal radius is defined as the radius beyond which the components of the subhalo are subjected to a gravitational force of the host halo that is greater than the one exercised by the subhalo itself.

Chapter 3

Gravitational lensing

Gravitational lensing is the deflection of light by masses in the Universe. This phenomenon happens because the light crosses the space-time deformed by the action of the gravitational fields produced by massive objects, called *gravitational lenses*, a simple sketch of the effect is shown in figure 3.1. Every massive object in the sky, from brown dwarfs to galaxy clusters, produces lensing effects on background sources, (Narayan and Bartelmann, 1996; Kneib and Natarajan, 2011).

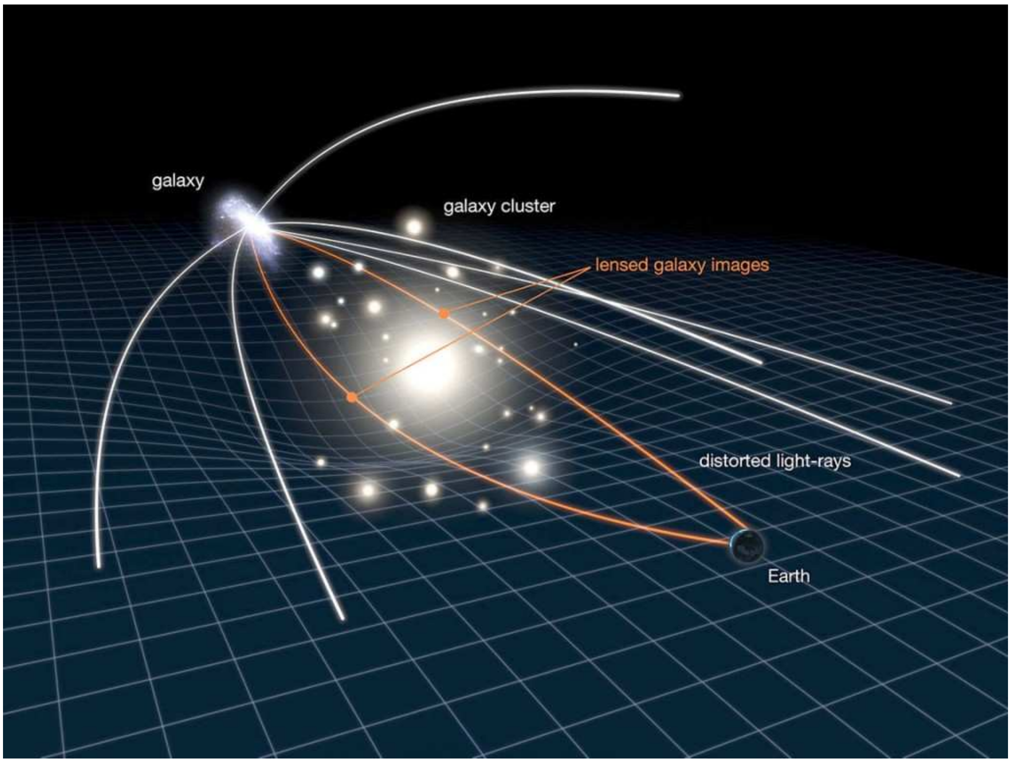

Figure 3.1: The image shows the effect of a gravitational lens on the space-time. Image from NASA/ESA.

Because of the light deflection, the background sources change their shapes and sizes and, as the surface brightness is conserved, this results in a source magnification or demagnification. The strength of the effect depends on the characteristics of the source-lens-observer system, in particular on their relative distances, and on the intrinsic properties of the lens.

3.1 Historical reference

Even though the theory of gravitational lensing was developed in the twentieth-century with the arrival of the General Relativity, the idea that light could be deflected by the presence of mass along its path has its seeds in classical physics. In fact, in the 18^{th} century, Isaac Newton suggested that masses should deflect light via gravity, even if he dis not develop the formalism to describe the phenomenon, (Ellis, 2010). The first formalization of this concept was realized in 1783 by John Mitchell, who, speculating that light consists of particles, sent to Henry Cavendish a paper with a method to calculate the mass of a star by measuring the reduction of light speed due to gravity in the path from the source to the observer. Later also Pierre Simon Laplace re-proposed this idea. Starting from that paper Cavendish calculated, in some private notes, in the framework of Newtonian theory of gravitation the deflection angle produced by a massive Sun-like body:

$$\Delta\theta \equiv \frac{2Gm}{c^2R} \approx 0''.875, \tag{3.1}$$

here G is the universal gravitational constant, c is the light speed and, for a Sun-like body, m and R correspond to the mass $M_\odot$ and the radius $R_\odot$ of the Sun, respectively.

This results was published only at the beginning of the nineteenth century by Johann Soldner. This value, calculated in the Newtonian limit, has been proved to be wrong and equal to one half of the true value. Indeed, its derivation did not take into account the local curvature of space-time in the surrounding of massive objects.

In 1915, Albert Einstein calculated in the framework of General Relativity, the true value of the deflection angle for a light ray passing in the gravitational field of the Sun:

$$\alpha \equiv \frac{4GM_\odot}{c^2R_\odot} \approx 1''.75. \tag{3.2}$$

The first experimental proof came in 1919 with the measurement of α during a total solar eclipse made by Arthur Eddington. Due to the lack of instrumentation dedicated to this kind of study, for several years the effects predicted by Einstein were believed to be unobservable, except for very particular rare cases, and this led to a very slow progress. This was true until the 60's when the publication of three papers on the lensing of galaxies by galaxies (Klimov, 1963), the lensing of stars on stars (Liebes, 1964) and the properties of point lenses and time delay (Refsdal, 1964), and the detection of the first quasars, gave new impulse to the field of research. Fifteen years later the first case of extragalactic lensing event was observed.

3.2 Gravitational lensing zoo

The deflection is described by geodesic lines following the curvature of the space-time[1]. The light is bent towards the mass which causes the space-time curvature. This gives origin to several important phenomena:

- *multiple images*: produced by multiple light paths around a single lens;
- *distortion of the sources in size and shape*: the deflection angle of light rays depends on the mass of the lens and on the impact parameter, so two light rays can be deflected differently according to how much close they pass to the deflector. In some cases, when the ray passes through the inner region of the lens, very spectacular and strong distortion can be seen, as Einstein rings, arcs and arclets. In other cases the amplitude of the distortion is very small, as in the case when the ray is passing very far from the lens. In this situations, distortions can be revealed only statistically, by averaging on a large number of sources;
- *magnification or demagnification*: Lensing does not change the surface brightness, it is only a geometrical effect and thus it can be used, in case of magnification, like an amplifier to observe distant sources too weak to be observed otherwise.
- *time delay*: due to the fact that different paths require different light travel time, the multiple images of the same source are characterized by different time delays.

---

[1] In curved space-time, geodesic lines are lines which are as straight as possible, resembling straight lines in flat space-time.

3.3 Lensing theory

We would like to derive a simple formalism to explain the lensing observational phenomenology. Starting from the field equations of general relativity, we can interpret the gravitational lens in terms of standard optics. In this way we can easily derive the main quantities that totally describe the observed features due to gravitational lensing.

3.3.1 Deflection angle

In the framework of General Relativity light propagates on null geodesics as it is defined in equation 1.2, depending on the matter distribution through the Einstein's field equation 1.17. The derivation of the deflection angle can be done by studying geodesic curves, and equivalently it is described by the *Fermat's principle: the path taken between two points by a light ray is the one that can be traversed in the least time.*

According to Fermat's principle, we search for a path $\vec{x}(l)$ such that the variational principle is satisfied:

$$\delta \int_A^B dl \, n(\vec{x}(l)) = 0. \tag{3.3}$$

Here, $n(\vec{x}(l))$ is the *effective refraction index* and its expression depends on the Newtonian gravitational potential, Φ. In order to find a function that well describes its behavior we need to make some approximations:

- we require that the *lens is weak*, this means that the Newtonian gravitational potential that characterizes the lens has to be much smaller than c^2:

$$\frac{\Phi}{c^2} \ll 1; \tag{3.4}$$

- we can assume that the inhomogeneities in the matter distribution are responsible for local perturbations in the metric, hence the dimension of the lens has to be small compared to the entire lensing system.

These assumptions are valid in all cases of astrophysical interest, even in the case of very massive lenses such as galaxy clusters. Indeed, the dimension of a galaxy cluster are few Mpc, whereas the typical size of a lensing system is fair fractions of the Hubble length, for example if we take sources at redshift

$z \sim 1$ the distances are on the order of 1 Gpc which are much larger than the physical size of the lens, and its gravitational potential is $|\Phi| < 10^{-4}c^2 \ll c^2$. Of course it is possible to extend the theory in order to describe other contexts that do not respect these requirements, as in the extreme cases of lensing due to neutron stars and black holes, (Virbhadra and Ellis, 2000, Bozza et al., 2001, Bozza, 2010). In these special cases the first order approximation is not sufficient,.

Considering the *Minkowsky metric*, that is the metric of unperturbed space-time:

$$\eta_{\mu\nu} = \begin{pmatrix} 1 & 0 & 0 & 0 \\ 0 & -1 & 0 & 0 \\ 0 & 0 & -1 & 0 \\ 0 & 0 & 0 & -1 \end{pmatrix}, \tag{3.5}$$

the norm of a four-vector in a Minkowsky's space will be:

$$ds^2 = \eta_{\mu\nu} dx^\mu dx^\nu = (dx^0)^2 - (d\vec{x})^2 = c^2dt^2 - (d\vec{x})^2. \tag{3.6}$$

If we consider the existence of a weak lens, the metric 3.5 will be perturbed by a small quantity $\frac{2\Phi}{c^2}$ in the following way:

$$\eta_{\mu\nu} \to g_{\mu\nu} = \begin{pmatrix} 1+\frac{2\Phi}{c^2} & 0 & 0 & 0 \\ 0 & -\left(1-\frac{2\Phi}{c^2}\right) & 0 & 0 \\ 0 & 0 & -\left(1-\frac{2\Phi}{c^2}\right) & 0 \\ 0 & 0 & 0 & -\left(1-\frac{2\Phi}{c^2}\right) \end{pmatrix}, \tag{3.7}$$

thus the norm becomes:

$$ds^2 = g_{\mu\nu} dx^\mu dx^\nu = \left(1+\frac{2\Phi}{c^2}\right)c^2dt^2 - \left(1-\frac{2\Phi}{c^2}\right)(d\vec{x})^2. \tag{3.8}$$

Because light propagates on null geodesic, the element ds has to be zero, thus imposing $ds = 0$ in equation 3.8 we derive the effective light speed in the gravitational field:

$$c' = \frac{|d\vec{x}|}{dt} = c\sqrt{\frac{1+\frac{2\Phi}{c^2}}{1-\frac{2\Phi}{c^2}}} \approx c\left(1+\frac{2\Phi}{c^2}\right), \tag{3.9}$$

where the last equality is due to the fact that the field has to be weak by assumptions. We can then calculate the refraction index:

$$n = \frac{c}{c'} = \frac{1}{1+\frac{2\Phi}{c^2}} \approx 1 - \frac{2\Phi}{c^2}. \tag{3.10}$$

So with $\Phi \leq 0$, $n \geq 1$ and the light speed in the regions perturbed by the gravitational field c' is lower than in the vacuum. This reduction of velocity implies that the time needed to travel along a perturbed path is larger by a quantity called *Shapiro delay*, (Shapiro, 1964):

$$\Delta t = \int \frac{dl}{c'} - \int \frac{dl}{c} = \frac{1}{c} \int (n-1) dl = -\frac{2}{c^3} \int dl\, \Phi. \tag{3.11}$$

In order to find the light path that satisfies the equation 3.3, we write the spatial element of integration as: $dl = |\frac{d\vec{x}}{d\lambda}| d\lambda$, where λ is a curve parameter; then with this change of variable, the equation 3.3 becomes:

$$\delta \int_{\lambda_A}^{\lambda_B} d\lambda\, n[\vec{x}(\lambda)] \frac{d\vec{x}}{d\lambda} = 0. \tag{3.12}$$

The argument of the integral in the equation 3.12 has the role of the Lagrangian $L(\dot{\vec{x}}, \vec{x}, \lambda) = n[\vec{x}(\lambda)] \frac{d\vec{x}}{d\lambda}$, with $\dot{\vec{x}} \equiv \frac{d\vec{x}}{d\lambda}$ that is the tangent vector to the light path that we can normalize by choosing conveniently λ. Using these definitions, we obtain the *Euler equations* :

$$\frac{d}{d\lambda} \frac{\partial L}{\partial \dot{\vec{x}}} - \frac{\partial L}{\partial \vec{x}} = 0. \tag{3.13}$$

$$\textit{if} \quad \vec{e} \equiv \dot{\vec{x}} \quad \textit{and} \quad |\dot{\vec{x}}| = 1 \quad \Rightarrow \quad \frac{d}{d\lambda}(n\vec{e}) - \vec{\nabla} n = 0. \tag{3.14}$$

It is possible to demonstrate that $\dot{\vec{e}} = \vec{\nabla}_\perp \ln n$. Using the expression for the refraction index 3.10 and the assumption of weak lens 3.4, it will result that

$$\dot{\vec{e}} \approx -\frac{2}{c^2} \vec{\nabla}_\perp \Phi. \tag{3.15}$$

The *total deflection angle* of the light path is the integral over $-\dot{\vec{e}}$, equation 3.15, along the light path:

$$\hat{\vec{\alpha}} = \frac{2}{c^2} \int_{\lambda_A}^{\lambda_B} d\lambda \vec{\nabla}_\perp \Phi. \tag{3.16}$$

But the equation 3.16 is not so useful as it stands, because we have to integrate on the actual path. Because we are in the weak lens approximation, the deflection angles are expected to be small, this is the reason why we can adopt the *Born approximation*[2] and integrate on the unperturbed light path.

---

[2] The Born approximation consists of taking the incident field in place of the total field, as the driving field at each point in the scatter. It derives from the perturbation method applied to scattering by an extended body. It is accurate if the scattering field is small, compared to the incident field, in the scatter.

Thus, supposing a light ray starts out into $+\vec{e}_z$- direction and passes the lens at $z = 0$, with *impact parameter* b, the deflection angle is given by:

$$\hat{\vec{\alpha}}(b) = \frac{2}{c^2} \int_{-\infty}^{+\infty} dz\, \vec{\nabla}_\perp \phi. \tag{3.17}$$

Point mass lens

The simplest example of gravitational lens is the point mass. Given the mass M, its gravitational potential is

$$\Phi = -\frac{GM}{r}. \tag{3.18}$$

We can calculate the gradient of Φ:

$$\vec{\nabla}_\perp \Phi = \begin{pmatrix} \partial_x \Phi \\ \partial_y \Phi \end{pmatrix} = \frac{GM}{r^3} \begin{pmatrix} x \\ y \end{pmatrix}. \tag{3.19}$$

Then, by substituting the equation 3.19 in the 3.17, we derive the deflection angle[3]

$$\hat{\vec{\alpha}}(b) = \frac{4GM}{c^2 b} \begin{pmatrix} \cos\phi \\ \sin\phi \end{pmatrix}. \tag{3.20}$$

The result 3.20, even if it was derived for a simple case, it is very important, because it ensures that $\hat{\vec{\alpha}}$ depends linearly on the mass M. Thus the deflection angle of an array of lenses can be linearly superposed.

3.3.2 General lens

In the case of an ensemble of point masses, we can use the linearity of the deflection in the potential, equation 3.20, and derive the deflection angle using the superposition principle.

Given N point masses M_i on a plane, whose positions are $\vec{\xi}_i$, with $1 \leq i \leq N$, the deflection angle of a light ray crossing the plane at the position $\vec{\xi}$ will be:

$$\hat{\vec{\alpha}}(\vec{\xi}) = \sum_i \hat{\vec{\alpha}}_i(\vec{\xi} - \vec{\xi}_i) = \frac{4G}{c^2} \sum_i M_i \frac{\vec{\xi} - \vec{\xi}_i}{|\vec{\xi} - \vec{\xi}_i|^2}. \tag{3.21}$$

---

[3] In the equations 3.19 and 3.20 the coordinates are:

$$r = \sqrt{x^2 + y^2 + z^2}, \qquad b = \sqrt{x^2 + y^2}$$

$$\textit{and} \qquad \begin{pmatrix} x \\ y \end{pmatrix} = b \begin{pmatrix} \cos\phi \\ \sin\phi \end{pmatrix},$$

where z is the component which lies along and b is the one perpendicular to the unperturbed path.

In a more realistic scenario masses are not distributed on a plane, but the matter has a three-dimensional distribution.
Since the size of the lens is typically much smaller than the dimension of the observer-lens-source system, we are justified to use the *thin screen approximation*: the three-dimensional matter distribution of the deflector is approximated by a planar distribution, called *lens plane*, also the background sources are approximated to lie on a plane, the *source plane.*

In this context the lensing matter distribution is well described by its *surface density*, given by the integral along the line of sight of the density profile:

$$\Sigma(\vec{\xi}) = \int dz\, \rho(\vec{\xi}, z), \tag{3.22}$$

where $\vec{\xi}$ is the two-dimensional vector on the lens plane and ρ is the three-dimensional density distribution. According to the fact that the deflection angle is the linear superposition of contributions due to all lens masses, we obtain the total deflection angle by summing the contribution of all mass elements $\Sigma(\vec{\xi})d^2\xi$:

$$\hat{\vec{\alpha}}(\vec{\xi}) = \frac{4G}{c^2} \int d^2\xi'\, \Sigma(\vec{\xi}) \frac{(\vec{\xi} - \vec{\xi}')}{|\vec{\xi} - \vec{\xi}'|^2}. \tag{3.23}$$

3.3.3 Lens equation

In figure 3.2 we show a diagram illustrating the typical geometry of a gravitational lens system.

Suppose to have a mass distribution placed at redshift z_L, thus it is at an angular diameter distance D_L from the observer. This lens perturbs the path of the light rays coming from a background source at redshift z_S, corresponding to the angular diameter distance D_S. The optical axis passes through the center of the lens and the observer, perpendicularly to the lens and the source planes. The source is at the angular position $\vec{\beta}$, which lies on the source plane at the distance $\vec{\eta} = \vec{\beta} D_S$ from the optical axis but, due to deflection, the source is seen as it was emitting light at the angular position $\vec{\theta}$. The deflection angle $\hat{\vec{\alpha}}$ of the light ray, coming from that source and having an impact parameter $\vec{\xi} = \vec{\theta} D_L$ on the lens plane, is given by the equation 3.17.

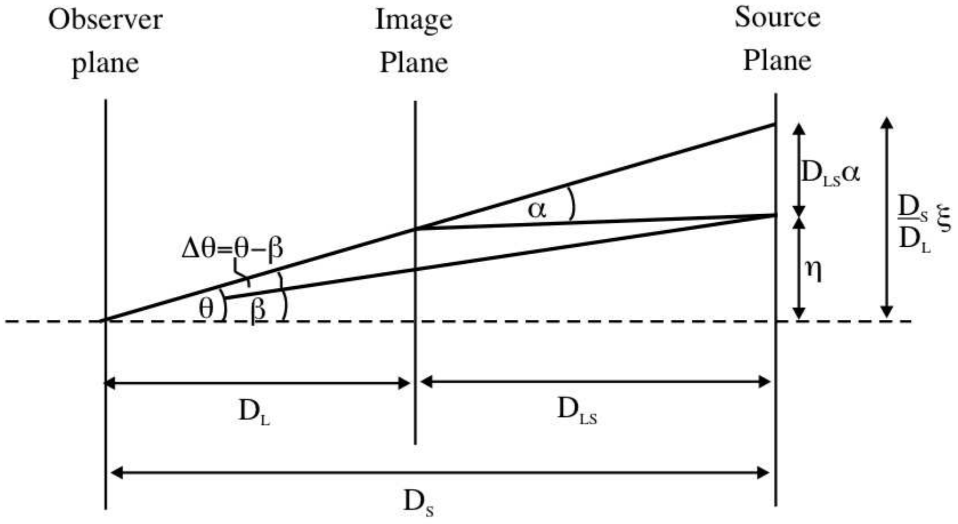

Figure 3.2: The diagram shows a simplification of a lens system. In the thin lens approximation the system is divided into three planes; the observer plane, the lens plane which is also plane that defines the angular position of the images on the sky and the source plane, (image taken from the thesis of A. Amara by courtesy of the author).

If $\vec{\theta}$, $\vec{\beta}$ and $\hat{\vec{\alpha}}$ are small, the true position of the source and the observed one are in a very simple relation, called the *lens equation*:

$$\vec{\theta} D_S = \vec{\beta} D_S + \hat{\vec{\alpha}} D_{LS}, \tag{3.24}$$

here D_{LS} is the angular diameter distance between the lens plane and the source plane.

We can define the *reduced deflection angle* as:

$$\vec{\alpha}(\vec{\theta}) \equiv \frac{D_{LS}}{D_S} \hat{\vec{\alpha}}(\vec{\theta}). \tag{3.25}$$

By substituting the definition 3.25 in the equation 3.24 we obtain a more simple form for the lens equation:

$$\vec{\beta} = \vec{\theta} - \vec{\alpha}(\vec{\theta}). \tag{3.26}$$

It is useful to rewrite the lens equation 3.24 in a dimensionless form, defining a length scale on the lens plane ξ, a corresponding length scale $\eta_0 = \xi_0 \frac{D_S}{D_L}$ on the source plane, the dimensionless vectors:

$$\vec{x} = \frac{\vec{\xi}}{\xi_0} \qquad \textit{and} \qquad \vec{y} = \frac{\vec{\eta}}{\eta_0}, \tag{3.27}$$

and the *scaled deflection angle*

$$\vec{\alpha}(\vec{x}) \equiv \frac{D_L D_{LS}}{\xi_0 D_S} \vec{\alpha}(\xi_0 \vec{x}). \tag{3.28}$$

Using the definitions 3.27 and 3.28 in the lens equation 3.24 we obtain the *dimensionless lens equation*:

$$\vec{y} = \vec{x} - \vec{\alpha}(\vec{x}). \tag{3.29}$$

3.3.4 Lensing potential

The *effective lensing potential* $\hat{\Psi}$ is a very important quantity for the characterization of a gravitational lens. It is obtained by projecting the three-dimensional Newtonian potential on the plane of the lens and by properly rescaling it:

$$\hat{\Psi}(\vec{\theta}) = \frac{D_{LS}}{D_L D_S} \frac{2}{c^2} \int dz \, \Phi(D_L \vec{\theta}, z). \tag{3.30}$$

Its dimensionless counterpart is $\Psi = \frac{D_L^2}{\xi_0^2} \hat{\Psi}$.

The effective lensing potential is related to the deflection angle and to the mass distribution of the lens:

- the gradient of Ψ gives the scale deflection angle $\vec{\alpha}(\vec{x})$,

$$\vec{\nabla}_x \Psi(\vec{x}) = \vec{\alpha}(\vec{x}); \tag{3.31}$$

- the laplacian of Ψ gives the *convergence* κ,

$$\Delta_x \Psi(\vec{x}) = 2\kappa(\vec{x}). \tag{3.32}$$

The convergence is a dimensionless surface density and it is defined as:

$$\kappa(\vec{x}) \equiv \frac{\Sigma(\vec{x})}{\Sigma_{cr}}, \tag{3.33}$$

where $\Sigma(\vec{x})$ is the surface density as defined in 3.22 and Σ_{cr} is the *critical surface density*, a constant depending on the angular diameter distances of the source D_S, of the lens D_L and among lens and source D_{LS}:

$$\Sigma_{cr} = \frac{c^2}{4\pi G} \frac{D_S}{D_L D_{LS}}. \tag{3.34}$$

If we integrate the relation between the potential and the convergence 3.32, we can express Ψ in terms of κ:

$$\Psi(\vec{x}) = \frac{1}{\pi} \int_{\mathbb{R}^2} d^2x' \, \kappa(\vec{x}') \ln|\vec{x} - \vec{x}'|; \tag{3.35}$$

then, from the equation 3.35 and the relation 3.31, we obtain the scaled deflection angle as a function of κ:

$$\vec{\alpha}(\vec{x}) = \frac{1}{\pi} \int_{\mathbb{R}^2} d^2x' \, \kappa(\vec{x}') \frac{\vec{x} - \vec{x}'}{|\vec{x} - \vec{x}'|}. \tag{3.36}$$

3.3.5 Distortion and magnification

The distortion introduced by lensing into the shape of sources is very important, mostly when the source has no negligible apparent size, like galaxies. The effect of distortion arises because light rays, passing in the area perturbed by the gravitational field, are deflected differentially depending on the distance from the lens center.
In theory the resolution of the lens equation 3.24 for all the points within the extended source allows us to reconstruct the shape of the image. If the source is much smaller than the angular size on which the physical properties of the lens change, the relation 3.29 between source and image position can locally be linearized.

The distortion of images can be fully described by the *Jacobian matrix* A, defined at the first order as:

$$A \equiv \frac{\partial \vec{y}}{\partial \vec{x}} = \left(\delta_{ij} - \frac{\partial \alpha_i(\vec{x})}{\partial x_j} \right) = \left(\delta_{ij} - \frac{\partial^2 \Psi(\vec{x})}{\partial x_i \partial x_j} \right). \tag{3.37}$$

The second equality in equation 3.37 is possible because of the relation 3.31.

We split the matrix A in its components, the symmetric and the antisymmetric one[4]. The symmetric component depends on the convergence:

$$\left(\frac{1}{2} trA \cdot I \right)_{ij} = \frac{1}{2} \left(1 - \Psi_{11} + 1 - \Psi_{22} \right) \delta_{ij} = (1 - \kappa) \delta_{ij}. \tag{3.38}$$

While the antisymmetric trace-free component is given by:

$$\begin{aligned} \left(A - \frac{1}{2} trA \cdot I \right)_{ij} &= \delta_{ij} - \Psi_{ij} - \frac{1}{2} \left(1 - \Psi_{11} + 1 - \Psi_{22} \right) \delta_{ij} \\ &= \begin{pmatrix} -\frac{1}{2}(\Psi_{11} - \Psi_{22}) & -\Psi_{12} \\ -\Psi_{21} & \frac{1}{2}(\Psi_{11} - \Psi_{22}) \end{pmatrix}. \end{aligned} \tag{3.39}$$

This antisymmetric trace-free matrix is very important and it is called *shear matrix*. It quantifies the projection of the gravitational tidal field, that is the gradient of the gravitational force, which describes the distortions on

---

[4] In the following we use the notation:

$$\Psi_{ij} = \frac{\partial^2 \Psi(\vec{x})}{\partial x_i \partial x_j}.$$

background sources. We define the pseudo-vector *shear* $\vec{\gamma} = (\gamma_1, \gamma_2)$ on the lens plane, its components are[5]:

$$\begin{cases} \gamma_1(\vec{x}) = \frac{1}{2}(\Psi_{11} - \Psi_{22}) = \gamma\cos(2\phi) \\ \gamma_2(\vec{x}) = \Psi_{12} = \Psi_{21} = \gamma\sin(2\phi) \end{cases} \tag{3.40}$$

The eigenvalues of the shear matrix are $\pm\sqrt{\gamma_1^2 + \gamma_2^2} = \pm\gamma$.

We can express the definition 3.37 in terms of shear and convergence:

$$\begin{aligned} A = &\begin{pmatrix} 1-\kappa-\gamma_1 & -\gamma_2 \\ -\gamma_2 & 1-\kappa+\gamma_1 \end{pmatrix} = \\ = (1-\kappa) &\begin{pmatrix} 1 & 0 \\ 0 & 1 \end{pmatrix} - \gamma \begin{pmatrix} \cos 2\phi & \sin 2\phi \\ \sin 2\phi & -\cos 2\phi \end{pmatrix}. \end{aligned} \tag{3.41}$$

The equation 3.41 underlines that the image distortions depend on the different contribution of convergence and shear.

In fact, the convergence, related to the symmetric component of the Jacobian, is responsible for the isotropic transformation, it does not alter the shape of the source and mapped it onto an image rescaled in size by a constant factor $(1-\kappa)$, in all directions, whereas the shear, introducing an anisotropic mapping, stretches the intrinsic shape of the source along a one privileged direction, the quantity $\gamma = (\gamma_1^2 + \gamma_2^2)^{1/2}$ is the magnitude of the shear and ϕ describes its orientation.

In figures 3.3 and 3.4 there are simple geometric explanation of the behavior of convergence and shear on a circular source.

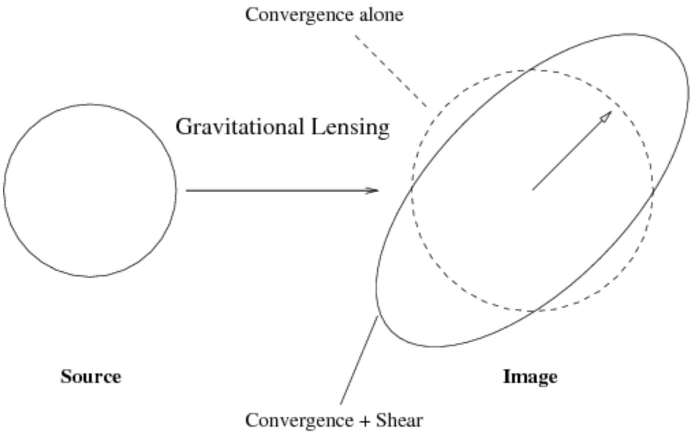

Figure 3.3: Effects of the convergence κ and the shear γ on the shape and size of a hypothetical circular source. The convergence acting alone causes an isotropic magnification of the image (dashed circle), while the shear deforms it to an ellipse, (Umetsu, 2010).

---

[5] The factor 2 on the angle ϕ reminds us that the shear components are elements of a 2×2 tensor and not a vector.

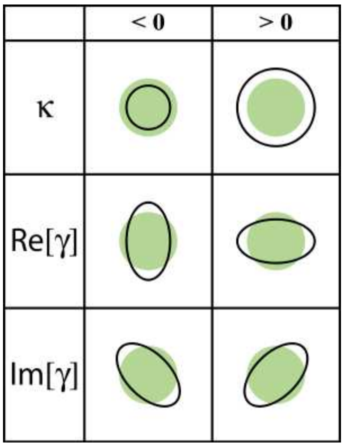

Figure 3.4: Effects of the components of the shear: $\gamma_1 = Re[\gamma]$ causes images to be stretched in the x or y directions; $\gamma_2 = Im[\gamma]$ causes images to be stretched along the 45 degree directions south-west to north-east and north-west to south-east.

The eigenvalues of A are:

$$\begin{cases} \lambda_t = 1 - \kappa - \gamma \\ \lambda_r = 1 - \kappa + \gamma \end{cases} \tag{3.42}$$

The *magnification* is an important consequence of the deformation of the shape and the size of the image.

According to the *Liouville theorem* and given that during the light deflection no photons are emitted or absorbed, the gravitational lensing conserves the source surface brightness, but the solid angle element $\delta\beta^2$, connected to the surface element δy^2 of the source, is mapped into the solid angle $\delta\theta^2$, related to δx^2 of the image. Thus, it changes the apparent solid angle under which the source is seen and this implies that the flux received from it is magnified or demagnified.

The magnification is given by the ratio of the image area to the source area and it is quantified by the inverse of the determinant of A: $M = A^{-1}$ is called the *magnification tensor*:

$$\mu = detM = \frac{1}{detA} = \frac{1}{(1-\kappa)^2 - \gamma^2} \tag{3.43}$$

The eigenvalues of M measure the magnification in the tangential and in the radial directions:

$$\begin{cases} \mu_t = \frac{1}{\lambda_t} = \frac{1}{1-\kappa-\gamma} \\ \mu_r = \frac{1}{\lambda_r} = \frac{1}{1-\kappa+\gamma} \end{cases} \tag{3.44}$$

When the determinant of the inverse of M vanishes the magnification becomes formally infinite. This happens when $\lambda_t = 0$ and $\lambda_r = 0$ and these two conditions define two curves on the lens plane called the *tangential* and *radial critical lines*, while on the source plane the corresponding locations are called *caustics*.

As example, in figure 3.5 we can see the caustics and the critical lines for a spherically symmetric lens.

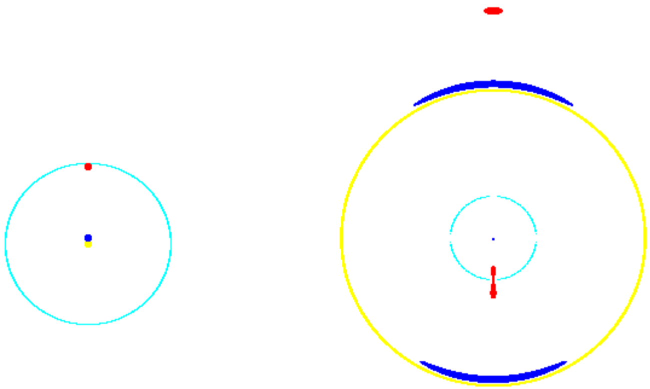

Figure 3.5: The caustics in the source plane are shown on the left panel, while the critical lines in the image plane are described in the right panel. The tangential and the radial caustic are respectively the central point in yellow and the circle in light blue on the source plane. The corresponding radial critical line is the light blue circle on the image plane, whereas the tangential one is the outer yellow circle. The appearance of the images corresponding to different source position in red and blue are also shown., (Hattori et al., 1999).

A source which lies close to the caustic can be magnified by very large factors. An image forming along the tangential critical line is strongly distorted tangentially to this line. An image forming close to the radial critical line is stretched in the direction perpendicular to the line itself.

3.4 Lensing at all the scales

Gravitational lensing can occur on all scales. The lens can be a point mass like stars, planets or compact objects, in this case we talk about of *micro-lensing*, or it can be extended like galaxies and clusters of galaxies. For the sake of simplicity we distinguish the effect, as we can see in figure 3.6, into two different regimes: *strong lensing*, when the convergence $\kappa > 1$, and *weak lensing*, when $\kappa \ll 1$ and $|\gamma| \ll 1$.

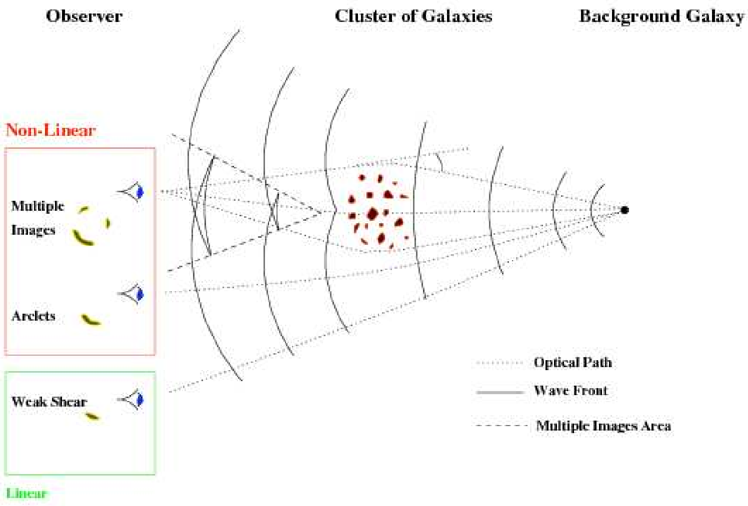

Figure 3.6: A simple schematic sketch of how lensed images are produced, delineating the strong and weak regimes, (Kneib and Natarajan, 2011).

3.4.1 Micro-lensing

Micro-lensing is due to small objects like stars, that are lenses too weak to produce images big enough to be resolved, in fact even if the lens splits the light coming from the source into two images their separation is less than few milli-arcsec. However the lensing does cause a measurable change in brightness of the background source and the amount depends on the angular separation between the source and the lens, (Wambsganss, 2006).

Then, if a star passes in front of some other object due to their relative motion, we may see a variability in the light curve of the source, then the magnification becomes a function of time.

Micro-lensing can be a useful tool in the searches of exoplanets (more details in Gaudi, 2010) and in the reconstruction of the distribution of the so-called MACHOs[6], which are possible candidates for the dark matter component in the galaxy, (Wyrzykowski et al., 2011).

3.4.2 Strong lensing

The strong regime happens when the observer is looking at far sources which appear to be projected on the sky at small angular distance from the center of the lens, (see e.g. Kochanek, 2006; Treu, 2010).

---

[6] Massive Astrophysical Compact Halo Objects

The strong lensing regime is characterized by strong distortion and production of multiple images separated up to several arcminutes.
The strong distortions, like the Einstein rings and the gravitational arcs, arise from the differential deflection of the light bundles, that can be in the radial or in the tangential direction, we can see in figures 3.7 and 3.8 two example of possible distortions.

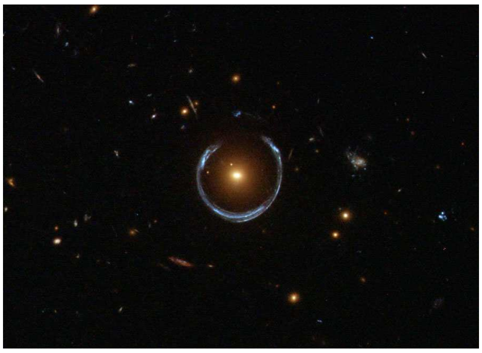

Figure 3.7: In the picture, the light coming from a distant blue galaxy is totally distorted in a almost complete ring by the strong gravitational field of the massive red galaxy $LRG\,3\text{-}757$, nearly perfectly aligned with the background galaxy and the observer, (image by courtesy of ESA & NASA).

Figure 3.8: The view of a distant galaxy, $\sim$ 10 billion light-years, has been distorted into a giant arc by the gravity of the galaxy cluster known as $RCS2\,032727\text{-}132623$, $\sim$ 5 billion light-years, (image by courtesy of NASA, ESA, J. Rigby, K. Sharon, M. Gladders and E. Wuyts).

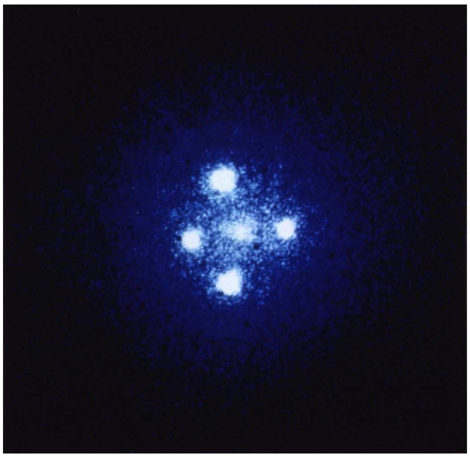

Figure 3.9: This is an image of the gravitational lens $G2237{+}0305$, also called *Einstein Cross*. In the photograph, a very distant quasar, due to the lensing effect of a relatively nearby galaxy, shows up into four images, with an angular separation of 1.6 arcsec between the upper and the lower, (image by courtesy of NASA, ESA and STScI).

Whereas the displacement of the images is due to the mass distribution of the lens, see figure 3.9 for an example, the spectra of all these images conserve all

the characteristic of the original spectrum of the source, thus multiple images can be identified by spectral analysis.
The effects of strong lensing are visually very impressive; nevertheless, for its nature, it happens to be rare.

3.4.3 Weak lensing

If the angular separation between source and lens is large, lensing shows up in the weak regime. In the weak regime the lensing effect results only in a tiny distortion of the elongation of the background galaxies. Unlikely the strong regime, that happens only at the center of the gravitational potential, it is present everywhere else, (see e.g. Mellier, 1999; Schneider, 2005). So the weak lensing regime represents a wonderful tool to study the matter distribution, (see e.g. Hoekstra et al., 2011). In particular, it is useful to investigate the properties of dark matter in large scale structure. In fact the LSS, spanning the space-time, is able to perturb the paths of photons emitted by distant galaxies and to weakly distort their shapes. Thus, the statistical analysis of the distortion pattern allows us to directly map the dark matter distribution, (Bacon et al., 2000, Refregier, 2003).

Being an effect with weak distortions and small magnification, in which the Jacobi matrix A, equation 3.37, is very close to the unit matrix, we cannot identify the weak lensing in an individual source, but to detect it we are forced to follow statistical approaches. Only averaging over the shapes of a large ensemble of images of background lensed galaxies and assuming the totally random distribution for their intrinsic shapes we can reconstruct the weak lensing signal with accuracy.

Image mapping

As we said before, the distortions can be described by the linearized lens mapping A.
According to the fact that light deflection preserves the surface brightness, $I(\vec{\theta}) = I^{(s)}[\vec{\beta}(\vec{\theta})]$, and considering the locally linearized lens equation:

$$\vec{\beta} - \vec{\beta}_0 = A(\vec{\theta}_0) \cdot (\vec{\theta} - \vec{\theta}_0), \tag{3.45}$$

the distortion of small lensed images is described by

$$I(\vec{\theta}) = I^{(s)}[\vec{\beta}_0 + A(\vec{\theta}_0) \cdot (\vec{\theta} - \vec{\theta}_0)]. \tag{3.46}$$

We introduce a new quantity the *reduced shear* g, defined as:

$$g(\vec{\theta}) \equiv \frac{\gamma(\vec{\theta})}{[1 - \kappa(\vec{\theta})]}. \tag{3.47}$$

By substituting the definition 3.47 in the equation 3.41, the Jacobi matrix can be written as:

$$A(\vec{\theta}) = (1 - \kappa) \begin{pmatrix} 1 - g_1 & -g_2 \\ -g_2 & 1 + g_1 \end{pmatrix}. \tag{3.48}$$

Then we can notice that the reduced shear fully describes the shape distortion of images through gravitational light deflection. It is a two-component quantity, g_α with $\alpha = 1, 2$. Both the shear and the reduced shear can be conveniently written as complex numbers:

$$\gamma = \gamma_1 + i\gamma_2 = |\gamma| e^{2i\varphi}; \qquad g = g_1 + ig_2 = |g| e^{2i\varphi}; \tag{3.49}$$

the amplitude describes the degree of distortion, whereas the phase fix the direction of distortion.

Consider a circular source with radius R; mapping it by the local Jacobi matrix, equation 3.48, its image will be an ellipse, with semi-axes:

$$\begin{cases} a = \frac{R}{1-\kappa-|\gamma|} = \frac{R}{(1-\kappa)(1-|g|)} \\ b = \frac{R}{1-\kappa+|\gamma|} = \frac{R}{(1-\kappa)(1+|g|)} \end{cases} \tag{3.50}$$

and the major axis encloses an angle φ with the positive θ_1-axis. So if the sources with circular isophotes could be identified, the measured image ellipticities would immediately constrain the value of the reduced shear, through the axis ratio $r = \frac{b}{a}$:

$$|g| = \frac{1 - r}{1 + r} \quad \Leftrightarrow \quad r = \frac{b}{a} = \frac{1 - |g|}{1 + |g|} \tag{3.51}$$

and the orientation of the major axis φ. In these relation we assumed that a is the major axis and $|g| < 1$.

The ellipticity is defined as

$$e = \frac{a - b}{a + b} = g = \frac{\gamma}{1 - \kappa} \approx \gamma. \qquad \kappa, \gamma \ll 1 \tag{3.52}$$

So in the limit of weak lensing the e is a measure of the reduced shear and then of the shear, that becomes an observable.

But distant faint galaxies are not intrinsically round, thus the observed image ellipticity, $e^{(\ell)}$, is a combination of intrinsic ellipticity, $e^{(s)}$, and shear, that acts like an extra ellipticity component due to the lensing structure along the line of sight.

$$e^{(\ell)} \sim e^{(s)} + g. \tag{3.53}$$

The strategy to estimate the shear or the reduced one consists in locally averaging over sufficiently many galaxy images, assuming that the intrinsic ellipticities are randomly oriented. In order to proceed, we need to understand what we define ellipticity of a source that is surely not circular but is not simply elliptical and so it has arbitrary isophotes.

The center of the image is defined in the following way:

$$\bar{\vec{\theta}} \equiv \frac{\int d^2\theta \, I(\vec{\theta}) q_I[I(\vec{\theta})]\vec{\theta}}{\int d^2\theta \, I(\vec{\theta}) q_I[I(\vec{\theta})]}, \tag{3.54}$$

where $I(\theta)$ is the brightness distribution of the image and q_I is a weight function. We can then define the *second-moment brightness tensor*:

$$Q_{ij} = \frac{\int d^2\theta \, I(\vec{\theta}) q_I[I(\vec{\theta})](\theta_i - \bar{\theta}_i)(\theta_j - \bar{\theta}_j)}{\int d^2\theta \, I(\vec{\theta}) q_I[I(\vec{\theta})]}, \qquad i, j \in \{1, 2\}. \tag{3.55}$$

Q is such that if the source has circular isophotes it is diagonal and $Q_{11} = Q_{22}$. Decomposing Q, the trace belongs to the size of the image, while the traceless part contains information about the ellipticity. From the equation 3.55 we can define two complex ellipticities:

$$\chi^{(\ell)} \equiv \frac{Q_{11} - Q_{22} + 2iQ_{12}}{Q_{11} + Q_{22}}; \tag{3.56}$$

$$\epsilon^{(\ell)} \equiv \frac{Q_{11} - Q_{22} + 2iQ_{12}}{Q_{11} + Q_{22} + 2(Q_{11}Q_{22} - Q_{12}^2)^{1/2}}; \tag{3.57}$$

which have the same phase but a different normalization. In the simple case of an images with elliptical isophotes and axis ratio $r \leq 1$, the ellipticities are:

$$|\chi^{(\ell)}| = \frac{1 - r^2}{1 + r^2}; \qquad |\epsilon^{(\ell)}| = \frac{1 - r}{1 + r}. \tag{3.58}$$

For the unlensed source the second-moment brightness tensor, $Q_{ij}^{(s)}$, and the complex ellipticities, $\chi^{(s)}$ and $\epsilon^{(s)}$, are defined in a similar way by replacing $\vec{\theta}$ with $\vec{\beta}$ and using $I^{(s)}$. It is possible to demonstrate that $Q_{ij}^{(s)}$ and $\chi^{(s)}$ and $\epsilon^{(s)}$ transform in the following way:

$$Q^{(s)} = AQA^T = AQA \tag{3.59}$$

$$\chi^{(s)} = \frac{\chi - 2g + g^2\chi^*}{1 + |g|^2 - 2Re(g\chi^*)} \tag{3.60}$$

$$\epsilon^{(s)} = \begin{cases} \frac{\epsilon - g}{1 - g^*\epsilon} & |g| \leq 1 \\ \frac{1 - g\epsilon^*}{\epsilon^* - g^*} & |g| > 1 \end{cases} \tag{3.61}$$

In cluster lensing data the case $|g| > 1$ only occurs for a small number of sources inside the critical curves: in massive clusters this region is typically small compared to the usual data fields.

We would stress that the weak lensing signal of a cluster is too faint to be distinguished from the intrinsic ellipticity of individual galaxies. This is the reason why, to derive the coherent distortion pattern and to estimate the shear and the reduced shear, we assume that the intrinsic orientation of galaxies is random, so its mean value is zero

$$E\left(\chi^{(s)}\right) = 0 = E\left(\epsilon^{(s)}\right). \tag{3.62}$$

This assumption is valid since there is no privileged direction in the Universe and among the galaxies there are cosmological distances, so they are not physically associated. Thus, by averaging the transformation law 3.61 over the intrinsic source orientation, Seitz and Schneider (1997) obtained:

$$E(\epsilon^{(\ell)}) = \begin{cases} g & |g| \leq 1 \\ 1/g^* & |g| > 1 \end{cases} \tag{3.63}$$

This is a very important result, because it shows that each image ellipticity provides an unbiased estimate of the local shear, though very noisy. The noise is determined by the intrinsic ellipticity dispersion:

$$\sigma_\epsilon = \sqrt{\langle \epsilon^{(s)} \epsilon^{(s)*} \rangle} \tag{3.64}$$

when averaging over N galaxy images all subject to the same reduced shear, the 1-σ deviation of their mean ellipticity from the true shear is $\sigma_\epsilon/\sqrt{N}$, and the noise can be beaten down by increasing the sample. Thus, the accuracy of a shear estimate depends on the local number density of galaxies so deep and wide imaging observations are required. The expectation value of χ cannot be easily calculated and is not simply related to the reduced shear as that of ϵ. However in the weak lensing regime $\kappa \ll 1$ and $|\gamma| \ll 1$ so we find:

$$\gamma \sim g \sim \langle \epsilon^{(\ell)} \rangle \sim \frac{\langle \chi^{(\ell)} \rangle}{2} \tag{3.65}$$

Instrumentation

For what we said before, the instruments useful for weak lensing studies need to have a high resolution (sub-arcsec) and to collect a large amount of galaxies: this can be achieved with a very large field of view and a large collective area to perform deep surveys. Furthermore, to accomplish accurate measurements of the intrinsic ellipticity, the telescope needs to have a stable PSF and, more generally, a stable optical response. At the moment there are a number of telescopes suitable for weak lensing studies, like the *Canada France Hawai'i Telescope* (CFHT, Radovich et al., 2008), the *Hubble Space Telescope* (HST, Hoekstra et al., 2000), the *Large Binocular Telescope* (LBT, Romano et al., 2010), the *VLT Survey Telescope* (VST, (de Jong et al., 2013)), the *Dark Energy Camera* (DECam, (Flaugher et al., 2015)) and Subaru (Okabe et al., 2010). Subaru has a wide field of view and a very stable PSF; it is an 8.2-meter optical-infrared ground telescope at the summit of the Mauna Kea, Hawai'i, and it represents the state of the art for such kind of studies.

In the near future we expect to have a further step forward, thanks to several new missions as the *Large Synoptic Survey Telescope* (LSST, LSST Science Collaboration et al., 2009) and Euclid, (Laureijs, 2009; Refregier et al., 2010). In particular, the Euclid mission, whose launch is expected to be 2020, is an ESA space mission that aims to investigate and to measure, with a great resolution: ~ 0.1 arcsec for the Visible Imager, VIS, and ~ 0.3 arcsec for the Near Infrared Spectrometer, NISP, the shape, the redshift and the spectrum of galaxies and galaxy clusters in 15000 deg^2 out to redshifts ~ 2, in the visible band and in the NIR, to infer information about dark Universe: dark energy, dark matter, gravity and initial condition of the Universe. The main scientific cosmological goals are the measure of baryonic acoustic oscillations, the redshift-space distortion pattern and the measure of the cosmic shear due to the weak lensing produced by the distribution of matter in the Universe on the background sources.

3.5 Lensing by Large Scale Structures

As we said in the previous sections, in an unperturbed space-time, light rays travel along null geodesic of the symmetric, homogeneous and isotropic Universe. But considering the LSS, the lenses have sizes comparable with the curvature scale of the Universe. Thus we need to upgrade the idea of straight light paths which are instantly perturbed and then deflected by sheet-like, thin lenses.

Starting from null geodesic in space-time, we can write the propagation equation for light bundles which travel through the unperturbed Universe, such that the comoving[7] separation vector $\vec{x}$ between them varies with the radial comoving coordinate w as

$$\frac{d^2\vec{x}}{dw^2} + K\vec{x} = 0, \tag{3.66}$$

where $K = (H_0/c)^2(\Omega_0 + \Omega_\Lambda - 1)$ is the curvature parameter of the Universe[8]. Ω_0 is the density parameter of the Universe at present time ($z = 0$), defined by 1.28 and Ω_Λ is the contribution to the density parameter by the cosmological constant, defined in the equation 1.27c.

The metric 1.3 can be written as

$$ds^2 = c^2dt^2 - a^2[dw^2 + f_K^2(w)d^2\Omega], \tag{3.67}$$

where $f_K(w)$ depends on the curvature of the Universe,

$$f_K(w) = \begin{cases} \frac{1}{\sqrt{K}}\sin(\sqrt{K}w) & K > 0 \\ w & K = 0 \\ \frac{1}{\sqrt{-K}}\sinh(\sqrt{-K}w) & K < 0 \end{cases} . \tag{3.68}$$

The equation 3.66 can be easily solved: it is an oscillator equation.
We find that:

$$\vec{x}(w) = \vec{\theta} f_K(w). \tag{3.69}$$

We can read into the solutions 3.69 in a very simple way. For $K = 0$ we are in an flat Euclidean space and we have $\vec{x} = \vec{\theta}w$. For negative and positive values of K, the bundles drift apart from each other, or get closer to each other, as the meridional lines on a hyperboloid or a sphere do.

---

[7] We would stress that the comoving coordinates take into account of the expansion of the Universe.

[8] Because c/H_0 is the Hubble length, K has the unit of an inverse squared length.

The masses responsible for the lensing are typically much smaller than the Hubble radius, this allow us to add perturbations in a very simple way, by considering a flat space-time in their surroundings, and to use our earlier result on the deflection angle. Thus the propagation equation 3.66 changes to[9]

$$\frac{d^2\vec{x}}{dw^2} + K\vec{x} = -\frac{2}{c^2}\vec{\nabla}_\perp\phi, \tag{3.70}$$

the new propagation equation 3.70 contains the space curvature and the local perturbations caused by a potential ϕ.

The equation 3.70 is an inhomogeneous oscillator and it can be solved by using a Green's function[10] $G(w, w')$, defined on the square $0 \leq w \leq w_s$, $0 \leq w' \leq w_s$, where w_s is the comoving distance of the source. According to the definition of a Green's function, for construction $G(w, w')$ satisfies the following conditions:

- $G(w, w')$ is continuously differentiable and satisfies the homogeneous differential equation 3.66;
- $G(w, w')$ is continuous on the entire square;
- the derivative of $G(w, w')$ with respect to w jumps by 1 on the boundary between the triangles A_1 and A_2 which form the domain;
- as a function of w, $G(w, w')$ satisfies the homogeneous boundary conditions on the solution.

These requirements are respected by the Green's function, generalized for different signs of K:

$$G(w, w') = \begin{cases} 0 & w < w' \\ f_k(w - w') & w > w' \end{cases} . \tag{3.71}$$

Therefore the general solution of the equation 3.70 reads

$$\vec{x} = f_K(w)\vec{\theta} - \frac{2}{c^2}\int_0^w dw' f_K(w - w')\vec{\nabla}_\perp\phi. \tag{3.72}$$

---

[9] Note that the perpendicular gradient of ϕ must be taken with respect to the comoving coordinates.

$$\vec{\nabla}_\perp\phi = \frac{1}{f_K(w)}\vec{\nabla}_{\vec{\theta}}\phi.$$

[10] The Green's functions are defined as the solutions of inhomogeneous differential equations, defined on a domain, with specified initial conditions or boundary conditions.

As we did in the single-lens plane approach, we assume the Born approximation and estimate this integral along the unperturbed path $f_K(w)\vec{\theta}$.

The deflection angle is defined as the deviation of the perturbed path from the unperturbed one,

$$\vec{\alpha} = \frac{f_K(w)\vec{\theta} - \vec{x}}{f_K(w)} = \frac{2}{c^2}\int_0^w dw' \frac{f_K(w-w')}{f_K(w)} \vec{\nabla}_\perp \phi[f_K(w')\vec{\theta}, w']. \tag{3.73}$$

This equation describes the angle $\vec{\alpha}(\vec{\theta}, w)$ along a light path propagating into direction $\vec{\theta}$ out to the distance w.

In the case of a flat Universe, we have $K = 0$ and $f_K(w) = w$. Then the equation 3.73 can be written as

$$\begin{aligned} \vec{\alpha}(\vec{\theta}, w) &= \frac{2}{c^2}\int_0^w dw' \left(1 - \frac{w'}{w}\right) \vec{\nabla}_\perp \phi(w'\vec{\theta}, w') = \\ &= \frac{2w}{c^2}\int_0^1 dy (1-y) \vec{\nabla}_\perp \phi(wy\vec{\theta}, wy). \end{aligned} \tag{3.74}$$

3.5.1 Effective convergence

In the single lens-plane case, the convergence is one half of the divergence of $\vec{\alpha}$, equations 3.31 and 3.32. Analogously, we define here an *effective convergence* for LSS lenses,

$$\begin{aligned} \kappa_{eff} &= \frac{1}{2}\vec{\nabla}_{\vec{\theta}} \vec{\alpha}(\vec{\theta}, w) = \\ &= \frac{1}{c^2}\int dw' \frac{f_K(w') f_K(w-w')}{f_K(w)} \Delta^{(2)} \phi[f_K(w')\vec{\theta'}, w'], \end{aligned} \tag{3.75}$$

here $\Delta^{(2)}$ is the two-dimensional Laplacian with respect to the comoving coordinates[11].

Now we replace the two-dimensional Laplacian with the three-dimensional one[12], Δ, and we assume that $\frac{\partial \phi}{\partial z} = 0$ at the boundaries of the perturbations. Thus the effective convergence becomes

$$\kappa_{eff} = \frac{1}{c^2}\int_0^w dw' \frac{f_K(w') f_K(w-w')}{f_K(w)} \Delta \phi[f_K(w')\vec{\theta'}, w']. \tag{3.76}$$

---

[11] Two-dimensional Laplacian:

$$\Delta^{(2)} = \vec{\nabla}_\perp^2 = \frac{\partial^2}{\partial x^2} + \frac{\partial^2}{\partial y^2}.$$

[12] Substitution:

$$\Delta^{(2)} \to \Delta = \frac{\partial^2}{\partial x^2} + \frac{\partial^2}{\partial y^2} + \frac{\partial^2}{\partial z^2}.$$

In $\Delta\phi$ we would substitute the Poisson's equation. It is expressed by the equation 1.41, where the Laplacian is taken with respect to the physical coordinates.
Considering the density contrast, δ, defined in the equation 1.55, we can write

$$\Delta\phi = 4\pi G\bar{\rho}(1+\delta)a^2 = 4\pi G\bar{\rho}_0(1+\delta)a^{-1}, \tag{3.77}$$

where we have inserted the equation 1.30 for ordinary matter[13].

We can decouple the potential into two contributes, one from the background and a peculiar one from the perturbation

$$\Delta\bar{\phi} = 4\pi G\bar{\rho}_0 a^{-1}, \tag{3.78a}$$

$$\Delta\phi = 4\pi G\bar{\rho}_0 a^{-1}\delta. \tag{3.78b}$$

By using $\bar{\rho}_0 = \frac{3H_0^2}{8\pi G}\Omega_0$, we yield the Poisson's equation 3.78b for the perturbation that we need,

$$\Delta\phi = \frac{3}{2}H_0^2\Omega_0 a^{-1}\delta. \tag{3.79}$$

The effective convergence can then be written as

$$\kappa_{eff}(\vec{\theta}, w) = \frac{3H_0^2\Omega_0}{2c^2}\int_0^w dw' \frac{f_K(w')f_K(w-w')}{f_K(w)}\frac{\delta[f_K(w')\vec{\theta}, w']}{a(w)}. \tag{3.80}$$

There is a similarity between the distance factor $\frac{f_K(w')f_K(w-w')}{f_K(w)}$ and the factor $\frac{D_L D_{LS}}{D_S}$ that we had in the single-lens case.

If the sources has a distribution in redshift z, the mean effective convergence is

$$\langle\kappa_{eff}\rangle(\vec{\theta}) = w\int_0^{w_H} dw\, G(w)\kappa_{eff}(\vec{\theta}, w), \tag{3.81}$$

here $G(w)dw$ represents the probability to find a source within the range $[w, w+dw]$.
Then we can write

$$\langle\kappa_{eff}\rangle(\vec{\theta}) = \frac{3H_0^2\Omega_0}{2c^2}\int_0^{w_H} dw\, W(w)f_K(w)\frac{\delta[f_K(w')\vec{\theta}, w']}{a(w)}, \tag{3.82}$$

where $W(w)$ is the effective weight function and it is defined as

$$W(w) = \int_0^{w_H} dw' G(w')\frac{f_K(w-w')}{f_K(w)}. \tag{3.83}$$

---

[13] The non-relativistic matter has the parameter of state equation w equal to 0, so the equation 1.30 becomes $\bar{\rho} = \bar{\rho}_0 a^{-3}$.

3.5.2 Limber's equation

It would be very interesting to derive the spatial distribution of perturbations though the lensing signal. But it is quite complicated to predict exactly which density fluctuations will be encountered by a light ray during its path.
Starting from what we know about the effective convergence, we thus resort to a statistical approach. We want to compute the two-point correlation function of the convergence

$$\langle \kappa(\vec{\theta})\kappa(\vec{\theta}+\vec{\phi})\rangle_{\vec{\theta}} = \xi_\kappa(\phi), \tag{3.84}$$

the average is made over all positions $\vec{\theta}$ on the sky, and over all directions of the separation vector $\vec{\phi}$. Anyway, the result cannot depend on the direction of $\vec{\phi}$, because of the isotropy. The two-point correlation gives information about the correlation on a given angular distance θ, (Coles and Lucchin, 2002).

If we move in the Fourier space, the formalism is more convenient and we can use the power spectrum.

Let suppose to have a function $g(x)$ in a n-dimensional space, whose correlation function is written as

$$\langle g(x)g(x+y)\rangle_x = \xi_{gg}(y). \tag{3.85}$$

In Fourier space, $g(x)$ and its transform are:

$$g(x) = \frac{1}{(2\pi)^n}\int d^n k\, \hat{g}(k)\exp(-ikx), \tag{3.86a}$$

$$\hat{g}(k) = \int d^n x\, g(x)\exp(ikx), \tag{3.86b}$$

and, by using the definition 3.86b, we calculate the correlation function:

$$\begin{aligned}\langle \hat{g}(k)\hat{g}^*(k')\rangle &= \left\langle \int d^n x\, g(x)\exp(ikx)\int d^n x'\, g(x')\exp(-ik'x')\right\rangle = \\ &= \int d^n x\ \exp(ikx)\int d^n x'\ \exp(-ik'x')\langle g(x)g(x')\rangle.\end{aligned} \tag{3.87}$$

We substitute $y + x = x'$ and use the isotropy of the correlation function, so the equation 3.87 becomes

$$\begin{aligned}\langle \hat{g}(k)\hat{g}^*(k')\rangle &= \int d^n x\ \exp[i(k-k')x]\int d^n y\ \exp(-ik'y)\xi_{gg}(y) = \\ &= (2\pi)^n\delta_D^{(n)}(k-k')P_g(k).\end{aligned} \tag{3.88}$$

In this equation we have defined the power spectrum

$$P_g(k) \equiv \int d^n y \, \exp(-iky) \xi_{gg}(y), \tag{3.89}$$

as the Fourier transform of the two-point correlation function[14]. The function $\delta_D^{(n)}$ is the Dirac delta in n-dimensions:

$$\delta_D^{(n)} = \int \frac{d^n x}{(2\pi)^n} \exp[i(k-k')x]. \tag{3.90}$$

Suppose that the power spectrum of a three-dimensional function $\delta(\vec{x})$ is known. What can we say about the power spectrum of its two-dimensional projection

$$g(\vec{\theta}) = \int dw \, q(w) \delta[f_K(w)\theta, w], \tag{3.91}$$

where $q(w)$ is a generic weighting function?

Let's answer to the question. The two point correlation function of $g(\vec{\theta})$ is

$$\begin{aligned} \xi_{gg} &= \langle g(\vec{\theta}) g(\vec{\theta'}) \rangle = \\ &= \int dw \, q(w) \int dw' \, q(w') \langle \delta[f_K(w)\vec{\theta}, w] \delta[f_K(w')\vec{\theta'}, w'] \rangle. \end{aligned} \tag{3.92}$$

Inserting the Fourier transform of δ, we find

$$\begin{aligned} \xi_{gg} = \int dw \, q(w) \int dw' \, q(w') \int \frac{d^3k}{(2\pi)^3} \int \frac{d^3k'}{(2\pi)^3} \langle \hat{\delta}(\vec{k}) \hat{\delta}^*(\vec{k'}) \rangle \\ \exp[-i f_K(w) \vec{\theta} \vec{k}_\perp] \exp[i f_K(w') \vec{\theta'} \vec{k'}_\perp] \exp(-iwk_s) \exp(iw'k'_s), \end{aligned} \tag{3.93}$$

here the wave vector k has been splitted into a perpendicular, $\vec{k}_\perp$, and a parallel component, k_s. The average $\langle \hat{\delta} \hat{\delta}^* \rangle$ can be replaced by the power spectrum of δ

$$\begin{aligned} \xi_{gg} = &\int dw \, q(w) \int dw' \, q(w') \int \frac{d^3k}{(2\pi)^3} P_\delta(k) \exp\{-i[f_K(w)\vec{\theta} - f_K(w')\vec{\theta'}]\vec{k}_\perp\} \cdot \\ &\cdot \exp[-ik_s(w-w')] = \\ = &\int dw \, q^2(w) \int \frac{d^3k}{(2\pi)^3} P_\delta(k) \exp[-i f_K(w)(\vec{\theta} - \vec{\theta'})\vec{k}_\perp] \cdot \\ &\cdot \int d(\Delta w) \exp(-ik_s \Delta w). \end{aligned} \tag{3.94}$$

The last integral in the equation 3.94 is equal to $2\pi\delta_D(k_s)$; this means that only modes perpendicular to the line-of-sight contribute to the correlation function,

---

[14] Wiener-Khintchine theorem, see for more details the sub-section 1.2.4.

and so $\vec{k} = (\vec{k}_\perp, 0)$. For this reason the k_s-integral can be carried out and we get

$$\xi_{gg} = \int dw\, q^2(w) \int \frac{d^2 k_\perp}{(2\pi)^2} P_\delta(|\vec{k}_\perp|) \exp[i f_K(w)(\vec{\theta} - \vec{\theta}')\vec{k}_\perp]. \tag{3.95}$$

We define $\phi \equiv |\vec{\theta} - \vec{\theta}'|$ the norm of the separation vector which spans between the two light paths. Considering isotropy, we have that

$$\xi_{gg}(\phi) = \int dw\, q^2(w) \int \frac{d^2 k}{(2\pi)^2} P_\delta(k) \exp[-i f_K(w)\vec{\theta}\vec{\phi}]. \tag{3.96}$$

From the previous equation we obtain the power spectrum of the projected quantity $g(\vec{\theta})$,

$$\begin{aligned} P_g(\ell) &= \int d^2\phi\, \xi_{gg}(\phi) \exp(i\vec{\ell}\vec{\phi}) = \\ &= \int dw\, q^2(w) \int \frac{d^2 k}{(2\pi)^2} P_\delta(k) \exp\{i[\vec{\ell} - f_K(w)\vec{k}]\vec{\phi}\}, \end{aligned} \tag{3.97}$$

here ℓ is the Fourier component related to the angular dimension θ in real space, through $\ell = \frac{2\pi}{\theta}$. We can now simply read the power spectrum of the effective convergence. By using the following weighting function

$$q(w) = \frac{3H_0^2\Omega_0}{2c^2} W(w) f_K(w) a^{-1}, \tag{3.98}$$

we have the so-called *Limber's equation*, (Limber, 1953):

$$P_\kappa(\ell) = \frac{9H_0^4\Omega_0^2}{4c^4} \int_0^{w_H} dw \frac{W^2(w)}{a^2} P_\delta\left(\frac{\ell}{f_K(w)}\right). \tag{3.99}$$

This equation is very important, because it relates the power spectrum of the convergence, P_κ, to the power spectrum of the density fluctuations, P_δ, and so, using it, we are able to connect the projected angular clustering of galaxies with the tree-dimensional clustering of galaxies.

For example, the two-point correlation function of the convergence is

$$\xi_\kappa = \int \frac{d^2\ell}{(2\pi)^2} P_\kappa \exp(-i\vec{\ell}\vec{\phi}). \tag{3.100}$$

Similarly to the single lens-plane case, see for details the sub-section 3.3.5, the magnification is given by

$$A = I - \frac{\partial\vec{\alpha}}{\partial\vec{\theta}} \to \mu = \frac{1}{detA} \to \mu \sim 1 + \vec{\vec{\nabla}}_{\vec{\theta}} \cdot \vec{\alpha} = 1 + 2\kappa_{eff} \tag{3.101}$$

Thus, the deviation with respect to unity of the magnification has the subsequent correlation function

$$\langle\delta_\mu(\vec{\theta})\delta_\mu(\vec{\theta}+\vec{\phi})\rangle = \xi_\mu(\phi) = 4\xi_\kappa(\phi) \tag{3.102}$$

and its root mean square value is

$$\langle\delta_\mu^2\rangle^{1/2} = \xi_\mu^{1/2}(0) = \left[\int_0^\infty \frac{\ell d\ell}{2\pi} P_\kappa(\ell)\right]^{1/2} \tag{3.103}$$

which is a measure of the typical magnification of sources due to the LSS.

3.5.3 Shear power spectrum

The shear, contrary to the convergence that has an isotropic behavior, depends on a privileged direction.

In a rotated reference frame, the shear γ can be decomposed in a tangential, γ_t, and in a cross, $\gamma_\times$, component. Let define ψ the effective lensing potential and $\vec{\phi}$ the separation vector between any two points that have a polar angle α with respect to the principal-axis frame of the shear. The components are:

$$\begin{cases} \gamma_t = -Re[\gamma e^{-2i\phi}] = \gamma[\cos^2(\alpha) - \sin^2(\alpha)] = \gamma\cos(2\alpha) \\ \gamma_\times = -Im[\gamma e^{-2i\phi}] = \gamma\sin(2\alpha) \end{cases} \tag{3.104}$$

remember that α could vary, so we have to average over it.

If we define the two-point correlation function of γ_t as $\langle\gamma_t\gamma_t'\rangle \equiv \xi_{tt}(\phi)$, we can obtain it from the power spectrum of the tangential shear component,

$$\xi_{tt}(\phi) = \int \frac{d^2\ell}{(2\pi)^2} P_{\gamma_t} \exp(-i\vec{\ell}\vec{\phi}). \tag{3.105}$$

The Fourier transform of γ_t is

$$\hat{\gamma}_t = -\frac{1}{2}(k_1^2 + k_2^2)\hat{\psi} = \frac{k^2}{2}[\cos^2(\alpha) - \sin^2(\alpha)]\hat{\psi}, \tag{3.106}$$

thus, its power spectrum is

$$P_{\gamma_t} = \frac{k^4}{4}[\cos^2(\alpha) - \sin^2(\alpha)]^2 P_\psi. \tag{3.107}$$

We know that the power spectrum of the convergence, κ, is

$$P_\kappa = \frac{1}{4}(k_1^2 + k_2^2)^2 P_\psi = \frac{k^4}{4} P_\psi, \tag{3.108}$$

therefore we can express P_{γ_t} in terms of P_κ :

$$P_{\gamma_t} = (\cos^2(\alpha) - \sin^2(\alpha))^2 P_\kappa. \tag{3.109}$$

Likewise for the tangential one, the two-point correlation function of the cross component of the shear, $\gamma_\times$, is

$$\langle \gamma_\times \gamma'_\times \rangle = \xi_{\times\times}(\phi) = \int \frac{d^2\ell}{(2\pi)^2} P_{\gamma_\times}(\ell) \exp(-i\vec{\ell}\vec{\phi}). \tag{3.110}$$

As before, we express the cross component power spectrum in function of the convergence one:

$$P_{\gamma_\times} = k_1^2 k_2^2 P_\psi = k^3 \cos^2(\alpha)\sin^2(\alpha) P_\psi = 4\cos^2(\alpha)\sin^2(\alpha) P_\kappa. \tag{3.111}$$

Finally, the mixed correlation function $\langle \gamma_t \gamma'_\times \rangle$ derives from the mixed power spectrum

$$P_{\gamma_t\gamma_\times} = \frac{1}{2}(k_1^2 - k_2^2) k_1 k_2 \frac{4}{k^4} P_\kappa = 2[\cos^2(\alpha) - \sin^2(\alpha)] \sin(\alpha)\cos(\alpha) P_\kappa \tag{3.112}$$

The integral which define $\langle \gamma_t \gamma'_\times \rangle$ has an odd symmetry[15], thus it makes the correlation function vanish, so $\xi_{t\times}(\phi) = 0$.
In any case, it makes sense to define the correlation functions:

$$\xi_\pm(\phi) \equiv \langle \gamma_t \gamma'_t \rangle \pm \langle \gamma_\times \gamma'_\times \rangle, \tag{3.113a}$$

$$\xi_\times \equiv \langle \gamma_t \gamma'_\times \rangle, \tag{3.113b}$$

and the expectation value of $\xi_\times(\phi)$ is 0. For any measurement of cosmic shear, $\xi_\times(\phi) = 0$ provides a test for the reliability of the measurement, because $\xi_\times(\phi) \neq 0$ points at systematic errors.

3.6 Lens model

In the lensing theory, in order to understand which type of lens is responsible of a particular image, several analytical lens models has been used to describe the lensing effect on different scales. For example, compact objects like planets, stars, black holes and MACHOs are well described by point mass lenses, while galaxies and clusters can be approximated to axially symmetric lenses.

---

[15] Because of the identity:

$$2[\cos^2(\alpha) - \sin^2(\alpha)] \sin(\alpha)\cos(\alpha) = \cos(2\alpha)\sin(2\alpha) = \frac{1}{2}\sin(4\alpha).$$

In the last case, the simple approximation has the advantage that surface density of such extended objects is independent on the position angle with respect to the center. Thus, choosing an optical axis intercepting the lens plane on the lens center, the surface density is $\Sigma(\vec{\xi}) = \Sigma(|\vec{\xi}|)$ and the problem can be reduced to a one dimensional form.

In general the deflection angle is a two-component vector, in this symmetric case $\hat{\alpha}$ points toward the center of the symmetry and its modulus is

$$\hat{\alpha}(\xi) = \frac{4GM(\xi)}{c^2\xi}, \qquad M(\xi) = 2\pi \int_0^{\xi} d\xi' \, \Sigma(\xi')\xi'. \tag{3.114}$$

3.6.1 The Navarro-Frenk-White density profile

As we described in the sub-section 2.3.1, in a ΛCDM cosmology, dark matter halos are well described by the NFW universal density profile, equation 2.14, within the broad halo mass range $3 \times 10^{11} \leq M_{200}/M_{\odot} \leq 3 \times 10^{15}$. The logarithmic slope of this profile changes from -1 at the center to -3 at larger radii. If we take $\xi_0 = r_s$ and we integrate the equation 2.14 along the line of sight, we obtain the surface mass density (Bartelmann, 1996):

$$\Sigma(x) = \frac{2\rho_s r_s}{x^2 - 1} f(x), \tag{3.115}$$

$$f(x) = \begin{cases} 1 - \frac{2}{\sqrt{x^2-1}} \arctan \sqrt{\frac{x-1}{x+1}} & x > 1 \\ 0 & x = 1 \\ 1 - \frac{2}{\sqrt{1-x^2}} \arctan h \sqrt{\frac{1-x}{x+1}} & x < 1 \end{cases}$$

Here the radial coordinate x is the radius in the two-dimensional space in units of the scale radius. If we define $\kappa_s \equiv \rho_s \Sigma_{cr}^{-1}$, then the convergence is

$$\kappa(x) = 2\kappa_s \frac{f(x)}{x^2 - 1}. \tag{3.116}$$

The shear depends only on the dimensionless radius and it is explicitly independent of the cosmology; its radial dependence, defining δ_c as the characteristic overdensity for the halo, is (Wright and Brainerd, 2000):

$$\gamma(x) = \kappa_s \delta_c \begin{cases} g_>(x) & x > 1 \\ \left[\frac{10}{3} + 4\ln\left(\frac{1}{2}\right)\right] & x = 1 \\ g_<(x) & x < 1 \end{cases} \tag{3.117}$$

where

$$g_>(x) = \frac{8 \arctan h \sqrt{(1-x)/(1+x)}}{x^2\sqrt{1-x^2}} + \frac{4}{x^2}\ln\left(\frac{x}{2}\right) - \frac{2}{x^2-1} + \frac{4 \arctan h \sqrt{(1-x)/(1+x)}}{(x^2-1)\sqrt{1-x^2}}$$

$$g_<(x) = \frac{8 \arctan \sqrt{(x-1)/(1+x)}}{x^2\sqrt{x^2-1}} + \frac{4}{x^2}\ln\left(\frac{x}{2}\right) - \frac{2}{x^2-1} + \frac{4 \arctan \sqrt{(x-1)/(1+x)}}{(x^2-1)^{3/2}}$$

The lens equation for this kind of lens can be solved using numerical methods. At fixed halo mass, the critical curves of an NFW lens are close to its center because of its flat density profile. There, the potential is less curved, thus the image magnification is larger and decreases more slowly away from the critical curves. Therefore NFW lenses are not so good in image splitting, but efficient in image magnification.

Chapter 4

Numerical simulation

In chapter 3 we stressed that with lensing measurements of the large scale structures we are able to determine the cosmic shear signal and we are interested to measure the cosmological parameters of its power spectrum. Additionally, in sub-section 3.5, we discussed the relation that allows us to express the power spectra of several observables, for example the shear, in terms of the convergence power spectrum. In its turn the convergence power spectrum, through the Limber's equation 3.99, is strictly related to the power spectrum of the density field.

Current experiments, as *Dark Energy Survey* (DES, Becker et al., 2016) and *Kilo Degree Survey* (KiDS, Kuijken et al., 2015), and future missions, like the *Large Synoptic Survey Telescope* (LSST, LSST Science Collaboration et al., 2009) and Euclid (Refregier et al., 2010, Laureijs et al., 2011), are including among their goals the measurements of the cosmic shear due to the weak lensing produced by the LSS in order to investigate the influence of dark matter on the development of structures on cosmic scales. In this framework it is very important to improve our knowledge about the effect of the large scale distribution of matter on light bundles coming from distant sources, in order to understand what these new missions are going to observe and how to improve their skills.

In this chapter we show a new method to reconstruct the LSS, able to reproduce the statistical properties of the density field and so of the lensing observables too, e.g. the cosmic shear.

4.1 Statistics

Because the observed details of the LSS, like the size, the densities and the distribution, strictly depend on cosmological parameters and on the properties of dark energy and dark matter (Davis et al., 1985) and it can affect the evolution of galaxies (Hung et al., 2016) too, the statistical features of the weak lensing produced by LSS can be used to constrain cosmological models in detail.

We focus our attention on *probability distribution function* and on the *power spectrum* of the convergence. Finally, we derived the *covariance matrix* and the *cross-correlation coefficient matrix* of the power spectrum, that are required for the building up of the Fisher matrix used in the estimate of the cosmological parameters from the observation.

4.1.1 Probability Distribution Function

The Probability Distribution Function of the convergence[1] gives the probability that, during the ray-tracing procedure, a light bundle coming from a certain redshift z_S can encounter a certain amount of density, and so can deflect of a consequent angle. In other words, it is an indirect measure of the amount of mass along the photons path, because it provides an estimate of the PDF of the density field responsible of the deflection, (Valageas, 2000).

The typical shape of the PDF is well represented by a log-normal function (Kayo et al., 2001, Takahashi et al., 2011) and through the analysis of PDF it is possible to distinguish among different cosmologies, but with the increasing of the source redshift, due to the fact that the amount of mass between the observer and the background galaxies increases, the PDF tends to be more Gaussian, so the differences among the models become less noticeable, (Munshi and Jain, 2000).

4.1.2 Power spectrum

The power spectrum is an important statistical quantity which characterize the LSS, allowing to extract cosmological information from the observation. We discussed in detail the convergence power spectrum $P_\kappa(\ell)$ in sub-section 3.5.2.

---

[1] Here and after we refer to it as PDF.

The power spectrum quantifies how much the density fluctuations on scale ℓ in the Fourier space contribute to density field in the real space, this means that it represents a measure of the power of the fluctuations in the scale ℓ.
As we said before, depending on the cosmological parameters, it is very useful to distinguish the cosmological models. In addition to this, $P_\kappa(\ell)$ provides information about the structures at all scales possible within the volume of the simulation in comparison with a theoretical model, thus it allows us to probes both the resolution limits and the accuracy of the lensing maps, (Harnois-Déraps et al., 2012).

4.1.3 Covariance matrix

The covariance matrix contains information about the variation of a random variable respect to others. It generalizes the notion of covariance for dimensions greater than two.

Given a population of n vectors X_i with k elements x_{hi}, $i = [1...n]$ and $h = [1...k]$, the covariance matrix will have $k \times k$ dimensions and its elements are defined by:

$$\sigma_{ij} = \frac{1}{n}\sum_{h=1}^{n}[(x_{hi} - \mu_i)(x_{hj} - \mu_j)], \tag{4.1}$$

where μ_i is the average made among the n values of x_{hi}.
By construction, it is symmetric, so $\sigma_{ij} = \sigma_{ji}$. On the main diagonal we find the variance, σ_{ii}, of x_{hi}, while out of the diagonal there is the covariance, σ_{ij}, between x_{hi} and x_{hj}.
Depending on the sign of the elements σ_{ij}, we can infer which kind of relation there is among the variables. If σ_{ij} is greater than 0, it means that the variables are correlated, a negative value points out an inverse correlation. If the variables are statistically independent, we have $\sigma_{ij} = 0$.

4.1.4 Cross-correlation coefficient matrix

The cross-correlation coefficient matrix is directly derived from the covariance matrix, definition 4.1, in the following way:

$$\rho_{ij} = \frac{\sigma_{ij}}{\sqrt{\sigma_{ii}\sigma_{jj}}}. \tag{4.2}$$

This matrix has $k \times k$ dimensions and it is symmetric, $\rho_{ij} = \rho_{ji}$. With respect to the covariance matrix, we lose all the information on variance because on

the main diagonal there are only 1, $\rho_{ii} = 1$. But it is very useful to underline the linear relation among the variables.
In fact, according to the sign of the elements of the matrix, we deduce the type of the correlation: if $\rho_{ij} > 0$ the variables are correlated, if $\rho_{ij} < 0$ they are anti-correlated, while if $\rho_{ij} = 0$, it means that the variables are uncorrelated. In addition, we can quantify the degree of correlation or anti-correlation: if $0 < |\rho_{ij}| \leq 0.3$ the correlation is weak, if $0.3 < |\rho_{ij}| \leq 0.7$ it is moderate, if $|\rho_{ij}| > 0.7$ the variables are strongly correlated.

4.2 Simulating the LSS with WL-MOKA

We want to build a tool to simulate the LSS in order to make cosmological forecast and compare to observations. There are two possible lines to follow, the first one is to reproduce light cones with N-body simulations, but we need a large number of realizations while the simulations are typically very expensive in terms of computational time or, and this is the way we pursue here, we can model the large scale structure as an ensemble of dark matter halos, in which the clumps of matter are distributed in a cosmologically consistent way.

This idea is based on the so-called halo-model for non-linear gravitational clustering. In this model, the density field is described by a distribution of clumps of matter with a given density profile (Cooray and Sheth, 2002).
For this reason we developed a semi-analytical tool able to reproduce mock light cones filled with halos. The LSS is thus described as the superposition of their density fields. During our work, we tested if this treatment is compatible with the simulation results.

4.2.1 MOKA

Our work builds on MOKA (Matter density distributiOn Kode for grAvitational lenses) developed by Giocoli et al. (2012a).
MOKA is a fast code for modeling dark matter halos in various cosmological context. Tuned on the state of the art of numerical simulations, it produces surface density distributions, convergence, shear and deflection angle maps. of isolated halos, modeled with the NFW profile. The halos can be spherical or triaxial (Jing and Suto, 2002).

In input the algorithm only requires the cosmological parameters ($\Omega_{\rm M}$, Ω_Λ, h, w), the redshift z_L and the mass of the lens and the source redshift z_S. It is also possible to choose the size of the map. It allows to add a BCG, whose stars are distributed following the Jaffe's profile 2.19a or the Hernquist's profile 2.19b. The central galaxy mass estimate is done with the Halo Occupation Distribution technique following the Wang et al. (2006) relation between the halo mass and the stellar mass. This feature is useful for strong lensing studies (Giocoli et al., 2016a). We stress that it is a very flexible tool, for that reason it assumes by default some relations, for e.g the Neto et al. (2007) c-M relation, but it is always possible to use an input file with the required relation. The code provides also the possibility to add substructures following the distribution 2.23, and to model their density profile with NFW or a Singular Isothermal Sphere, equation 2.24.

4.2.2 WL-MOKA

In this work we use a very fast version of MOKA, dedicated to the analysis of the weak lensing properties of dark matter, called WL-MOKA. At the moment we can simulate only the surface density of spherical halos, but in the next future we would like to modify the code by increasing the complexity of the halos, adding the possibility to consider different shapes, introducing the triaxiality (Jing and Suto, 2002), the presence of substructures (Salvador-Solé et al., 2011) and of a brightest cluster galaxy in the center (Postman et al., 2012) in order to make the code more realistic.
Starting from cosmologically consistent catalogues of masses, positions and redshifts of dark matter halos, WL-MOKA generates mock light cones filled with three-dimensional distributions of halos and derives total convergence maps. Finally, we add a feature which is able to calculate the two-dimensional power spectrum of the convergence.

The main ingredients of our recipe are listed below, with the reference to the previous sections where we discussed them in detail:

- *Virial mass* and *virial radius* of the dark matter halos, equation 2.15:

$$M_{vir} = \frac{4\pi}{3} R_{vir}^3 \frac{\Delta_{vir}}{\Omega_m(z)} \Omega_0 \rho_c;$$

- *Navarro-Frenk-White radial density profile*, equation 2.14:

$$\rho_{NFW}(r) = \frac{\rho_s}{\frac{r}{r_s}\left(1+\frac{r}{r_s}\right)^2};$$

- *Virial concentration*, equation 2.16:

$$c_{vir} = \frac{R_{vir}}{r_s},$$

for which we assumed the fitting formula derived by Zhao et al. (2009) fixing the value of the variance $\sigma_{\ln\,c} = 0.25$, equation 2.18:

$$c_{vir}(M_{vir}, z_l) = 4\left\{1+\left[\frac{t(z_l)}{3.75\,t_{0.04}}\right]^{8.4}\right\}^{\frac{1}{8}}.$$

In figure 4.1 we show the c-M relations for all the lens plane redshifts.

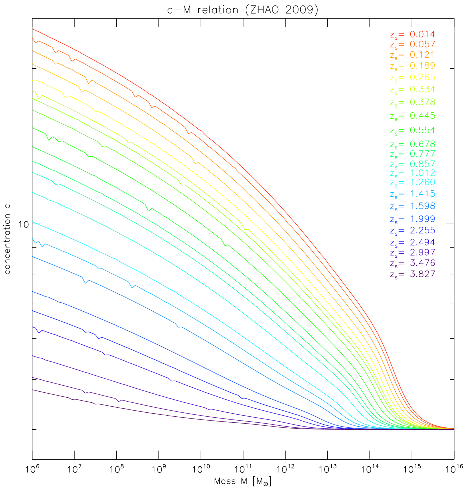

Figure 4.1: The concentration-mass relation derived by Zhao et al. (2009) for all the lens redshift of interests for our light cones; from redshift 0 (red curve) up to redshift 4 (violet curve).

In the following table 4.1, we listed the cosmological parameters used to reconstruct the mock light cones, which are consistent with the cosmological parameter of the N-body simulation evaluated.

Parameters	Value
Matter density parameter	$\Omega_{\mathrm{M}} = 0.2711$
Λ density parameter	$\Omega_{\Lambda} = 0.7289$
Hubble constant	$H_0 = 100\ h^{-1}$ km sec^{-1} Mpc^{-1}
	$h = 0.703$
Adimensional parameter in state equation	$w = -1$

Table 4.1: Cosmological parameters used to set the initial conditions in WL-MOKA.

4.3 The cosmological simulation

To test the limits and fine tune our code, we used the halo catalogues obtained from the ΛCDM set of the COupled Dark Energy Cosmological Simulations (CoDECS), performed by Baldi (2012b). They were obtained using the parallel TreePM-SPH N-body code GADGET (Springel, 2005), modified in order to take into account all the additional physical effects that characterize coupled dark energy models. The suite is a huge numerical initiative featuring a direct interaction between the dark energy (DE) scalar field, responsible for the observed cosmic acceleration, and the cold dark matter (CDM) fluid.

They performed different realizations considering different models of the interacting DE. Their results provided the first realistic determination of the effects of coupling DE on cosmological growth histories fully compatible with the latest cosmic microwave background data.
In this section we describe some characteristics of the simulations and we refer to the original papers for further details.

4.3.1 Simulation parameters

In the simulations were produced different scenarios, following different flat cosmological models, implemented with the same amplitude of density perturbations at the redshift of the last scattering surface, $z \sim 1100$. The realizations include CDM, baryons, radiation and a classical DE scalar field. For all the models the cosmological parameters at present time, $z = 0$, are the same. In table 4.2 we can read the values of the parameters.

Parameters	Value
CDM density parameter	$\Omega_{\mathrm{CDM}} = 0.226$
DE density parameter	$\Omega_{\mathrm{DE}} = 0.729$
Baryons density parameter	$\Omega_{0\mathrm{b}} = 0.0451$
Hubble constant	$H_0 = 100\ h^{-1}$ km sec^{-1} Mpc^{-1} $h = 0.703$
Primordial spectral index	$n_s = 0.966$
Normalization of the scalar perturbations	$A_s = 2.42 \times 10^{-9}$

Table 4.2: In table we listed the cosmological parameters used in the CoDECS suite.

These values have been chosen consistently with data coming from WMAP-7 (Komatsu et al., 2009).

The initial conditions are generated with Code for Anisotropies in the Microwave Background (CAMB, Lewis et al., 2000) at $z = 99$.

The boundary conditions are periodic and in the volume of the simulations there is the same number of dark matter and gas particles distributed in the volume with identical random phases adopted for the generation of the initial conditions.

The simulations follow the evolution of 2×1024^3 particles of dark matter and gas, with a resolution in mass equal to $M_{\mathrm{CDM}} \simeq 5.84 \times 10^{10}\ h^{-1}\ M_{\odot}$ for CDM and $M_b \simeq 1.17 \times 10^{10}\ h^{-1}\ M_{\odot}$ for baryons, in a volume with dimensions $L_{box} = 1\ h^{-1}$ comoving Gpc.

As we said, in the CoDECS suite several simulations with different models of DE are available: the standard ΛCDM model, a model with exponential potential (Wetterich, 1988) and the bouncing SUGRA coupled DE potential model (Brax and Martin, 1999, Baldi, 2012a).

In our work we analysed only the realization corresponding to the ΛCDM model.

4.4 Method

Starting from the outputs of the numerical simulation catalogues, we constructed mock light cones populated with dark matter halos. The light cone consists of a sequence of planes at a different redshifts. The background sources are on the source planes. We computed convergence maps on each plane and we analyzed the convergence probability distribution function, PDF, and power spectra, $P_\kappa(\ell)$. Finally, we derived the covariance and the cross-correlation coefficient matrices.

In this section we describe in detail the different steps of our procedure.

4.4.1 Construction of the light cones

The set we analysed consists of 25 different realizations of the ΛCDM Universe. The realizations are in the form of catalogues listing masses and positions of the halos at each redshift. In table 4.3 we summarize the properties of the boxes used to create the light cones.

Id^a	z^b	d$_{c,i}$^{c}	d$_{c,f}$^{d}	Snapshot^e	z$_{snap}$^{f}
1	0.0140562	0	84.0064	92	0
2	0.0570376	84.0064	259.557	86	0.05754
3	0.121306	259.557	446.037	81	0.1202
4	0.159115	446.037	644.73	76	0.1589
5	0.26525	644.73	856.648	71	0.2648
6	0.334292	856.648	1000	66	0.3492
7	0.377627	1000	1083.47	66	0.3492
8	0.445096	1083.47	1327.27	61	0.4442
9	0.554193	1327.27	1590.23	56	0.5523
10	0.677651	1590.23	1875.02	51	0.6771
11	0.777313	1875.02	2000	46	0.8238
12	0.857121	2000	2186.66	46	0.8238
13	1.01217	2186.66	2560.1	41	1
14	1.26029	2560.1	3000	38	1.25982
15	1.41511	3000	3014.24	38	1.25982
16	1.5977	3014.24	3491.74	35	1.6095
17	1.99956	3491.74	3947.12	32	2.01329
18	2.25461	3947.12	4000	29	2.47956
19	2.49439	4000	4377.61	29	2.47956
20	2.99726	4377.61	4782.82	26	3.01798
21	3.47647	4782.82	5000	23	3.63972
22	3.82671	5000	5179.52	23	3.63972

Table 4.3: In table we listed ^{a} id of the planes; ^{b} redshift of the lens; ^{c} initial comoving distance of the box [h^{-1} Mpc]; ^{d} final comoving distance of the box [h^{-1} Mpc]; ^{e} snapshot; ^{f} redshift of the snapshot.

To simulate the light cones we stacked the volumes derived from the simulation one behind the other up to the requested redshift. During the stacking process the boxes are shifted and rotated, to avoid the repetition of the same structures along the line-of-sight, (Roncarelli et al., 2012). In figure 4.2 we show a schematic picture of a light cone, identified with the red lines, in which we can see the lens planes (in green) and the boundaries of each box (in blue).

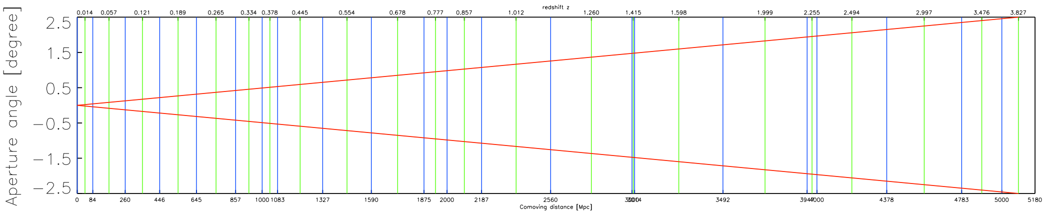

Figure 4.2: Cartoon of a light cone. The Field-of-view is shown in red. The cone was obtained by stacking all the twenty-two boxes up to $z_S = 4$. The green vertical lines indicate the lens planes and the blue lines are the boundaries of each box.

The background galaxies are assumed to be on the source planes and we considered four different source redshifts, $z_S = [0.5, 1, 2, 4]$. The range of redshift $z_4 = [0, 4]$ corresponds to $d_c \sim 5179,77\ h^{-1}$ Mpc and it counts for 22 cubes; the range of redshift $z_3 = [0, 2]$ corresponds to $d_c \sim 3719.71\ h^{-1}$ Mpc and it counts for 17 cubes; the range of redshift $z_2 = [0, 1]$ corresponds to $d_c \sim 2353.5\ h^{-1}$ Mpc and it counts for 13 cubes and the range of redshift $z_1 = [0, 0.5]$ corresponds to $d_c \sim 1335.49\ h^{-1}$ Mpc and it counts for 9 cubes.

All the cones we designed have an angular aperture of 5 deg. The analysed catalogues are slightly bigger than the mock light cones, this means that we consider not only the halos whose center falls inside the light cone but also buffer halos. We made this choice because we would consider also halos out of the field of view, but still able to influence the lensing properties with their density fields.

4.4.2 Convergence maps

Once the three-dimensional spatial distribution of halos has been generated, we projected their three-dimensional density profile creating the convergence maps for all the lens planes. We divided the field of view into 2048^2 pixels and we calculated the convergence for each pixel due to the matter distribution within the cube by summing the contribution due to each halo.

The convergence κ is defined as the ratio between $\Sigma(x,y)$, that is the surface matter density which totally describes the halo, and Σ_{cr}, the critical density (equation 3.34) which contains all the information about the lensing system, by the equation 3.33. The surface matter density $\Sigma(x,y)$ is obtained by projecting the three-dimensional density profile ρ_{NFW}, equation 2.14, on the lens plane with an integration along the line of sight:

$$\Sigma(x,y) = \int dz\, \rho_{NFW}(x,y,z). \tag{4.3}$$

Contrary to the procedure indicated in Bartelmann (1996) and discussed in sub-section 3.6.1, in order to not consider the contribution to the convergence field due to the extra-mass distributed out of the halo, we decided to not extend the integral in the previous equation 4.3 to infinity, but, considering as a first approximation the halos like spheres with a variable radius equal to aR_{vir}, to truncate the integration of the density profile:

$$\begin{aligned} \Sigma(c_{vir},\delta) &= \rho_s r_s \eta(c_{vir},\delta) \qquad (4.4)\\ &= \rho_s r_s 2 \int_0^{\sqrt{a^2 c_{vir}^2-\delta^2}} \frac{dt}{\sqrt{t^2+\delta^2}(1+\sqrt{t^2+\delta^2})^2}, \end{aligned}$$

where the factor 2 depends on the symmetry of the sphere, $\delta = \sqrt{x^2+y^2}/r_s$ is the dimensionless distance of a given pixel on the map from the center of the halo, $t = z/r_s$ is the dimensionless variable of integration, and a is a factor which defines the truncation radius in units of the virial radius, see figure 4.3.

In figure 4.4 we show the comparison among the convergence maps of a single halo with mass $M = 3.14 \times 10^{13}\, M_\odot$, a virial concentration $c_{vir} = 4.58$ at redshift $z_L = 0.05$ with sources at $z_S = 1$, in which the integration of the density profile has been extended from 1 up to 8 virial radii and to infinity; the angular dimension of the maps is 5 deg and it contains 2048^2 pixels.

In these maps it is possible to see that, in the case of truncated halos, the convergence is zero outside the edge of the halo, identified with the yellow

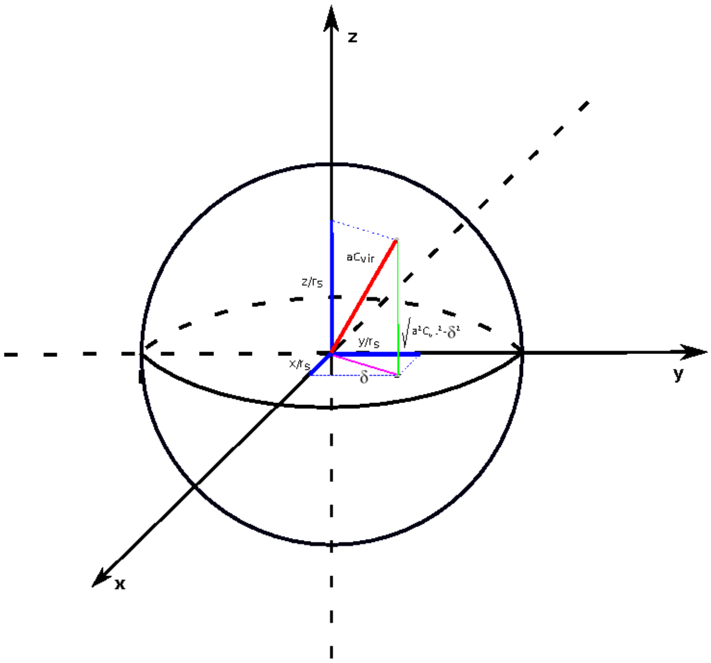

Figure 4.3: Geometry of a spherical halo considered during the integration in order to calculate the surface density. The blue vectors x/r_s, y/r_s and z/r_s represent the coordinates in unit of the scale radius of the the surface element, in gray on the sphere, that is the top face of the density column that we would project on the corresponding pixel, in gray on the two-dimensional map. The red vector ac_{vir} is the radius of the halo in unit of the scale radius. The pink vector δ is the distance of the pixel from the center of the halo. The green vector $\sqrt{a^2c_{vir}^2 - \delta^2}$ is the the distance of the surface element of the sphere from the plane.

circles, while in the case of smooth halo in which the profile is not truncated the convergence slowly decreases covering the entire map.

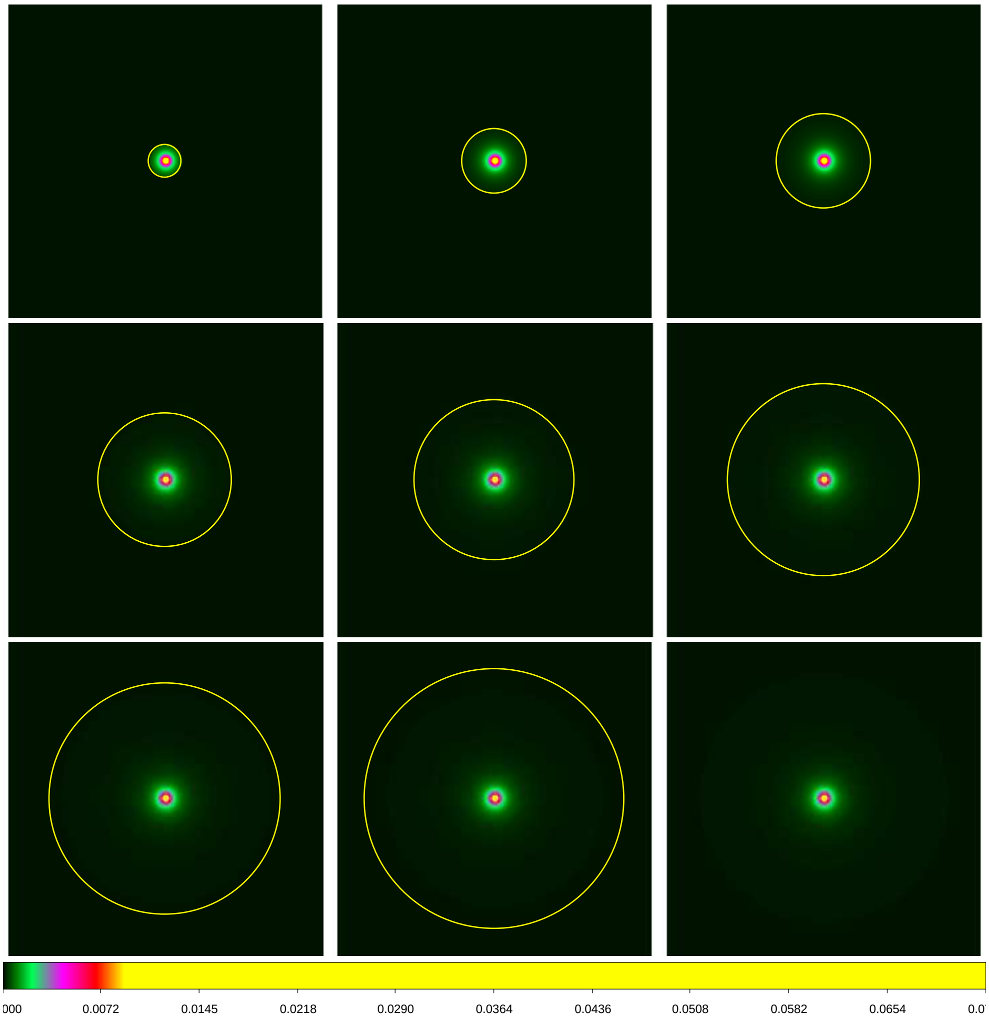

Figure 4.4: Comparison among the convergence maps of a single halo. The first 8 panels, from the top, show density profiles integrated from 1 up to 8 R_{vir}, while in the last one the integration has been extended up to infinity. The yellow circles represent the edge of the halo.

To better underline the differences among the integrated density profile, it is useful to see figure 4.5, and in particular the zoom shown in the right panel, related to the zone where the profiles are truncated. We can observe that the integration up to infinity produce a higher convergence, indicated with the red curve, respect to the truncated integration.

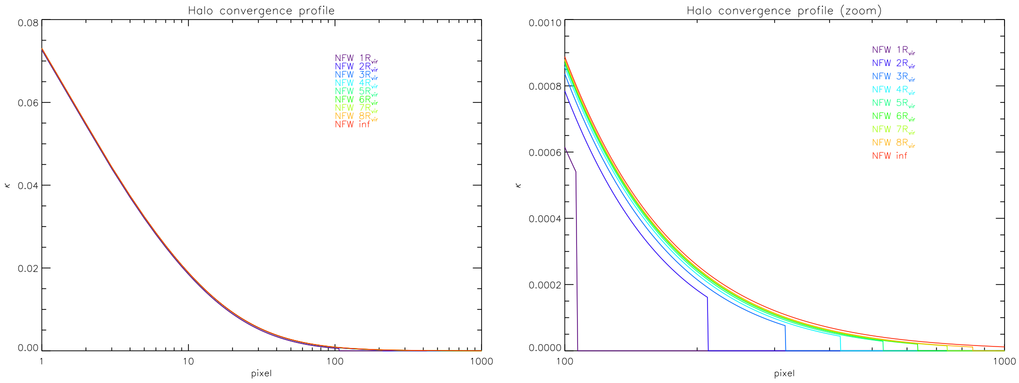

Figure 4.5: On the left panel we plot the convergence profiles from the center of the halo up to the end of the map, taken from the convergence maps shown in figure 4.4. On the left panel there is a zoom of the zone in which the profiles are truncated. The red curve belongs to a not truncated halo, while the others refer to halos which change their dimension from 1 up to 8 R_{vir}.

In order to identify the best choice for a, we performed several tests, by varying the value of this parameter in the range $[1, 8]$. Our goal was to select the value which best reproduce the convergence power spectrum of the numerical simulation. In figure 4.6 we show two examples of the convergence maps generated with WL-MOKA; in the left panel the light cones has been populated with halos truncated at the virial radius, while in the right panel the halos are truncated at 8 virial radii. For both light cones the source redshift is $z_S = 4$.

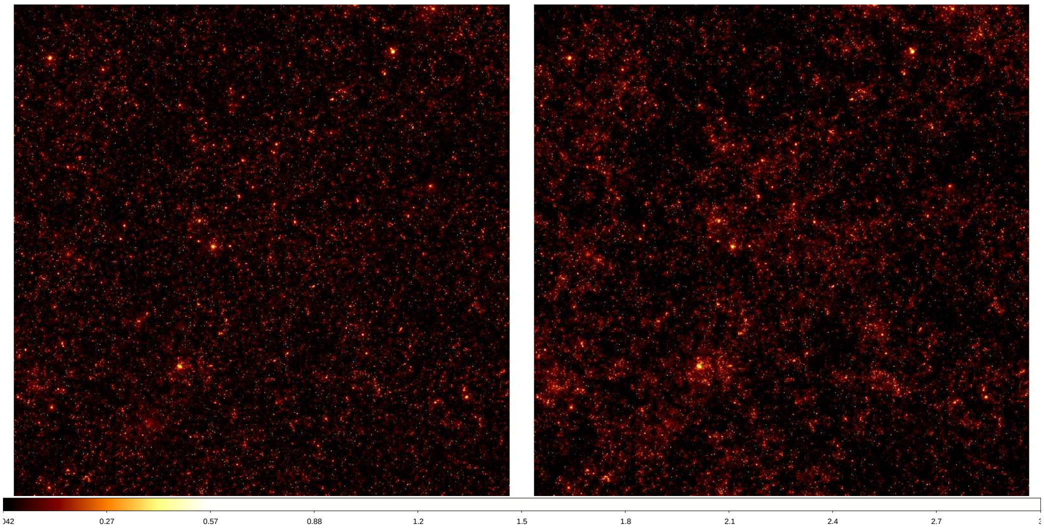

Figure 4.6: Convergence maps of two light cones populated with halos truncated at $1\,R_{vir}$ on the left panel and at $8\,R_{vir}$ on the right panel. The halos are obtained from the same catalogue. The source redshift is $z_S = 4$.

In addition to this, we also considered the possibility that the halos could have different density profiles outside the virial radius with respect to the NFW profile.

In particular, we assume a power law $\rho_{out} \propto r^{-\beta}$. and we investigate how the power spectra change by varying the slope β in the range $[3.5, 6]$. The total profile has the form:

$$\rho(r) = \begin{cases} \rho_{in} = \rho_{NFW} & r \leq R_{vir} \\ \rho_{out} = \frac{\rho_s c_{vir}^{\beta}}{c_{vir}(1+c_{vir})^2} \left(\frac{r}{r_s}\right)^{-\beta} & r > R_{vir} \end{cases} . \tag{4.5}$$

In figure 4.7 we show two examples of the convergence maps of a single halo with mass $M = 3.14 \times 10^{13}\, M_{\odot}$, a virial concentration $c_{vir} = 4.58$ at redshift $z_L = 0.05$ with sources at $z_S = 1$, modeled with the profile 4.5 and truncated at 5 virial radii; the angular dimension of the maps is 5 deg and it contains 2048^2 pixels. The yellow circles represent the edge of the halo.

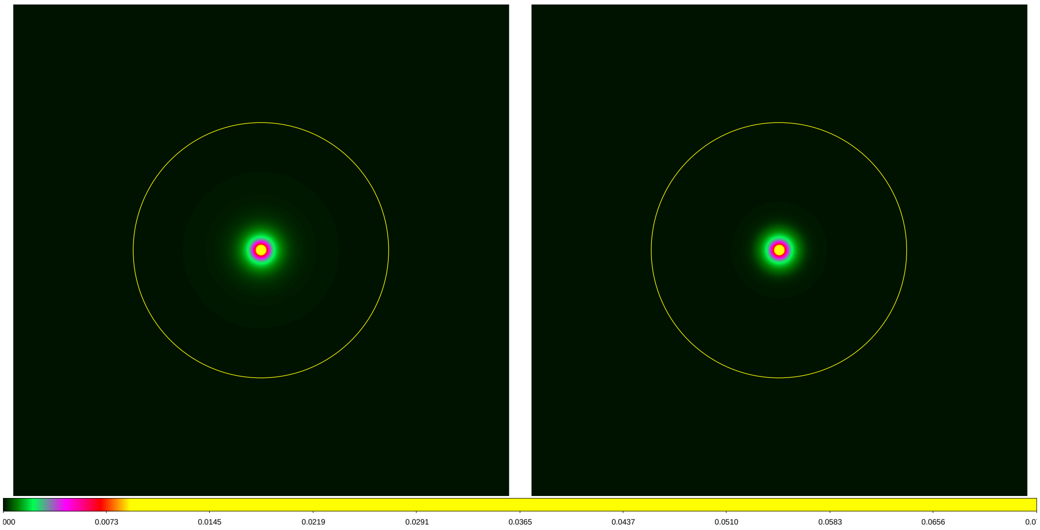

Figure 4.7: Comparison among the convergence maps of a single halo modeled with a NFW profile up to the virial radius and with a power law up to $5\, R_{vir}$. In the left panel the external slope β is 4, in the right panel $\beta = 6$. The yellow circles represent the edge of the halo.

We can note that the two halos have the same dimension, but the convergence is higher in the case the bigger external slope. In figure 4.8, in particular in the zoom shown in the right panel, it is possible to note the difference between the convergence profiles indicated in different color for the different value of β and compared with the convergence profile of a halo modeled by the NFW profile and truncated at 5 virial radii.

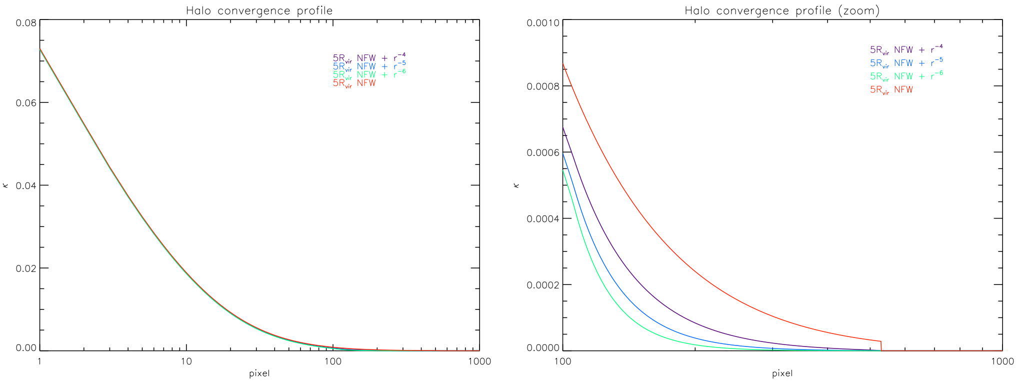

Figure 4.8: On the left panel we plot the convergence profiles from the center of the halo up to the end of the map, taken from the convergence maps of isolated halos modeled with a NFW profile up to the virial radius and with a power law up to $5\,R_{vir}$ for different values of β, green for $\beta = 6$, blue for $\beta = 5$ and violet for $\beta = 4$, compared with the convergence profile of a halo modeled with NFW up to $5\,R_{vir}$, in red. On the right panel we show a zoom of the profiles.

In figure 4.9 we show on the left panel the convergence map of a light cone populated with halos modeled with NFW profile up to the virial radius and with $\rho \propto r^{-4}$ up to 5 virial radii, compared with the convergence map obtained from a light cone filled with halos modeled with NFW profile and truncated at 5 virial radii, shown in the right panel. Both light cones are generated with WL-MOKA and the source redshift is $z_S = 4$.

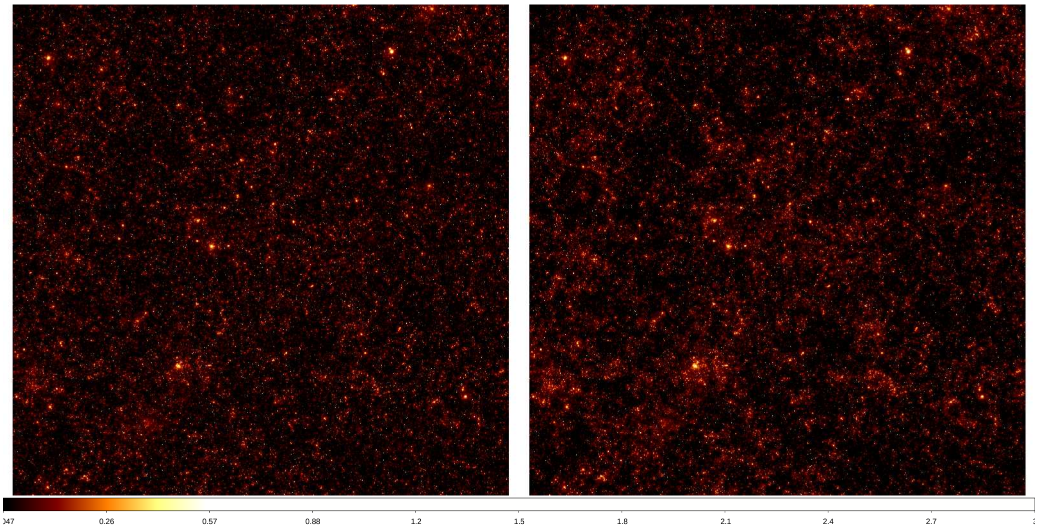

Figure 4.9: Convergence maps of two light cones populated with halos modeled with NFWprofile up to $1\,R_{vir}$ and with $\rho \propto r^{-4}$ up to $5\,R_{vir}$ on the left panel and halos modeled with NFW profile and truncated at $5\,R_{vir}$ on the right panel. The halos are obtained from the same catalogue. The source redshift is $z_S = 4$.

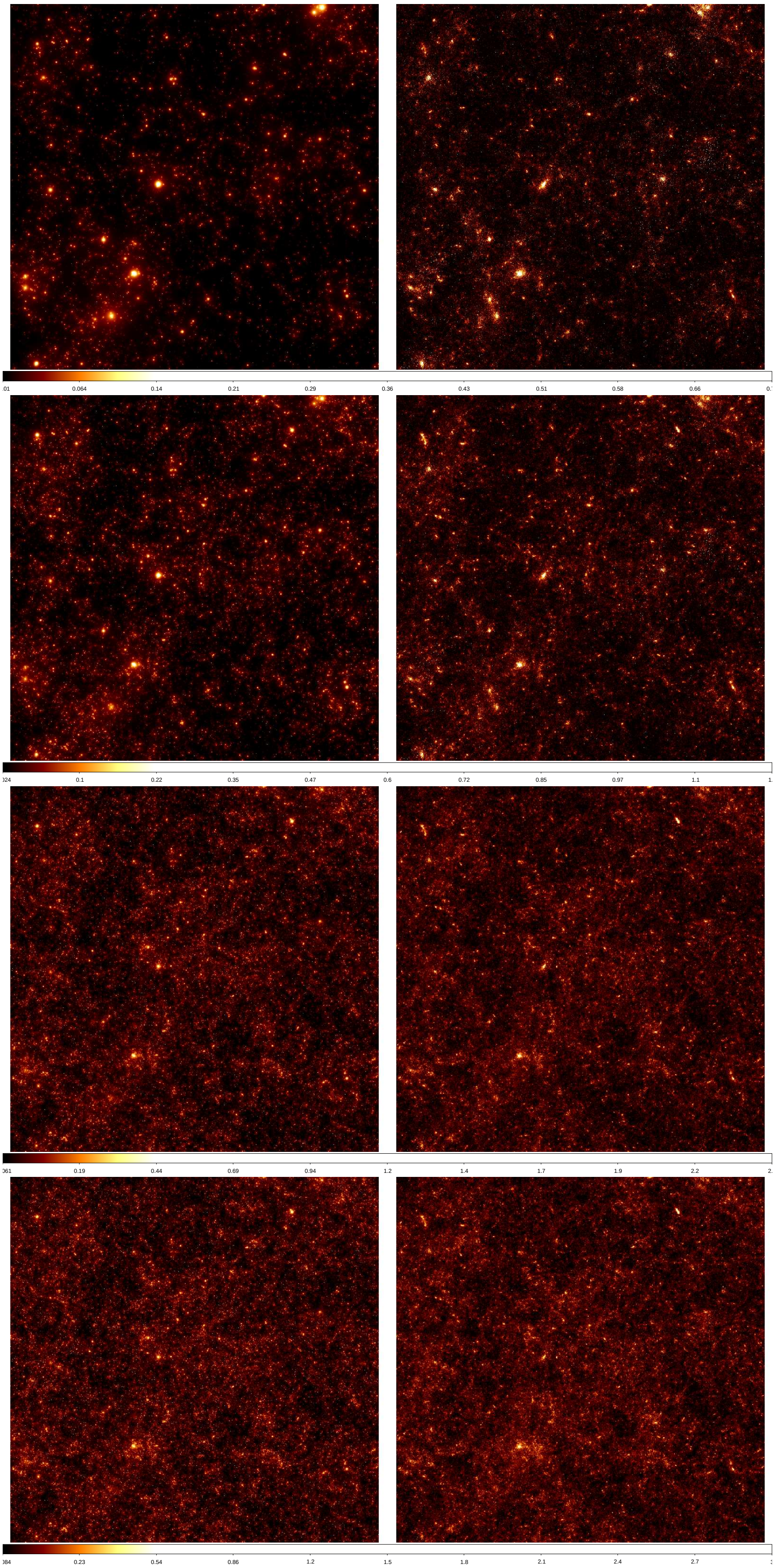

Figure 4.10: Comparison between the total convergence map derived from mock light cones populated by dark matter halos extended up to $5\,R_{vir}$, on the left, and the total convergence map derived from mock light cones populated by particles, on the right. The background galaxies are from the top: in the first panel at $z_S = 0.5$, in the second panel at $z_S = 1$, in the third panel at $z_S = 2$ and in the fourth panel at $z_S = 4$.

The convergence map for each lens plane is given by the sum of the convergence in each pixel due to every halo on the lens plane. At least the total convergence map of the light cone is calculated by summing the convergence maps, coming from each lens plane, with zero average, in order to consider only the contribution due to perturbations.

In figure 4.10 we show, for example, the comparison between the total convergence maps extracted from light cones populated with halos truncated at 5 virial radii generated with WL-MOKA, in the left panels, and the total convergence maps extracted from light cones populated by particles with the simulation, in the right panels. The maps are shown for four different source redshifts. From the comparison it is evident that the maps are similar, we can recognize the same structures, even if in the convergence maps extracted from the simulation the filaments are present. In figure 4.11 we show a zoom of both the maps produced with WL-MOKA and with the simulation for $z_S = 4$, where it is better to visualize the same peaks of density.

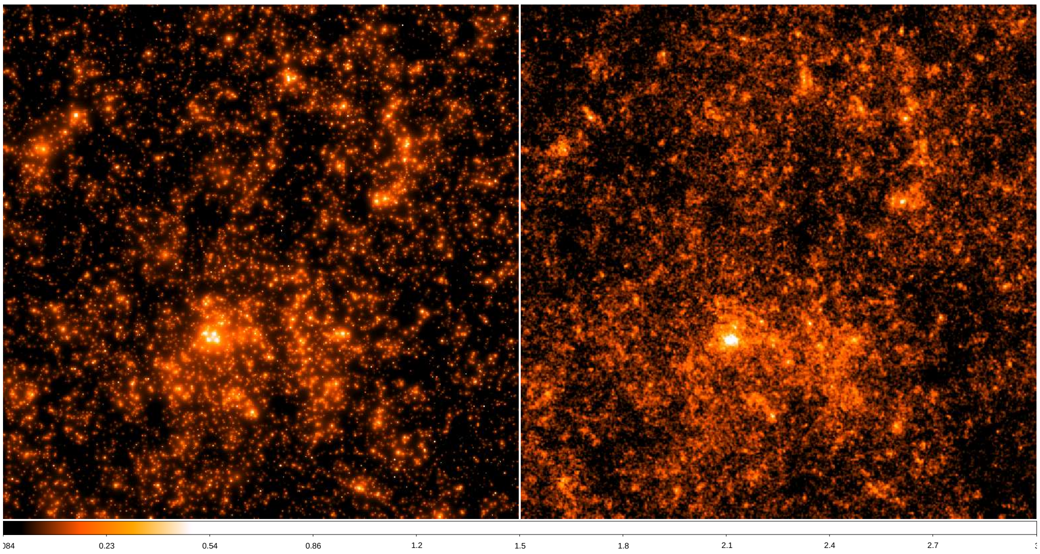

Figure 4.11: Zoom of the comparison between the total convergence map derived from mock light cones populated by dark matter halos extended up to $5\,R_{vir}$, on the left, and the total convergence map derived from mock light cones populated by particles, on the right. The background galaxies are at $z_S = 4$.

From the total convergence maps we extract the probability distribution function and the power spectrum for each light cone.

4.5 Testing WL-MOKA

In this section we report on some tests of our algorithm to create mock light cones. In particular, we focused on how the results are affected by the choice of the truncation of the halos. Our metrics are the convergence PDF and the convergence power spectrum. We consistently derive these quantities from the light cones obtained with WL-MOKA and from the CoDECS simulation and quantify the differences.

4.5.1 Probability distribution function

Given a convergence map with a total number of pixel equal to N_κ, we can define the probability distribution function of κ as:

$$PDF_{wl}(\bar{\kappa}_i, z_s)\Delta_i \sim \frac{N_{\kappa,i}}{N_\kappa}, \tag{4.6}$$

here $N_{\kappa,i}$ is the number of pixel whose κ value is falling in the bin Δ_i centered around the mean value $\bar{\kappa}_i$. To produce the PDFs we divided the range of convergence for each total map in 32 linear bin. Then we counted how many pixels fall inside each bin and we normalized it.

In figure 4.12 we plotted the PDFs extracted from several light cones. The different panels refer to four source redshifts, namely $z_S = 0.5, 1, 2, 4$. In each panel, we showed in black the PDF obtained from the light cone constructed with the CoDECS simulation. We also showed, with different, colors the PDFs from the light cones constructed with WL-MOKA, assuming various values of the halo truncation radius in the range $[1, 8]$ virial radii.

We can see that all the PDFs produced by our code are well described by a log-normal function as we expected from theory and there is an agreement with the result of the simulation, an agreement that ameliorates with the increasing of the dimension of the halos.

We also note that the PDFs are broader when the size of the truncation radius is chosen to be larger.

The steepness of the PDF obtained from the numerical simulation can be explained by the lower spatial resolution of the simulation, compared to those produced with WL-MOKA.

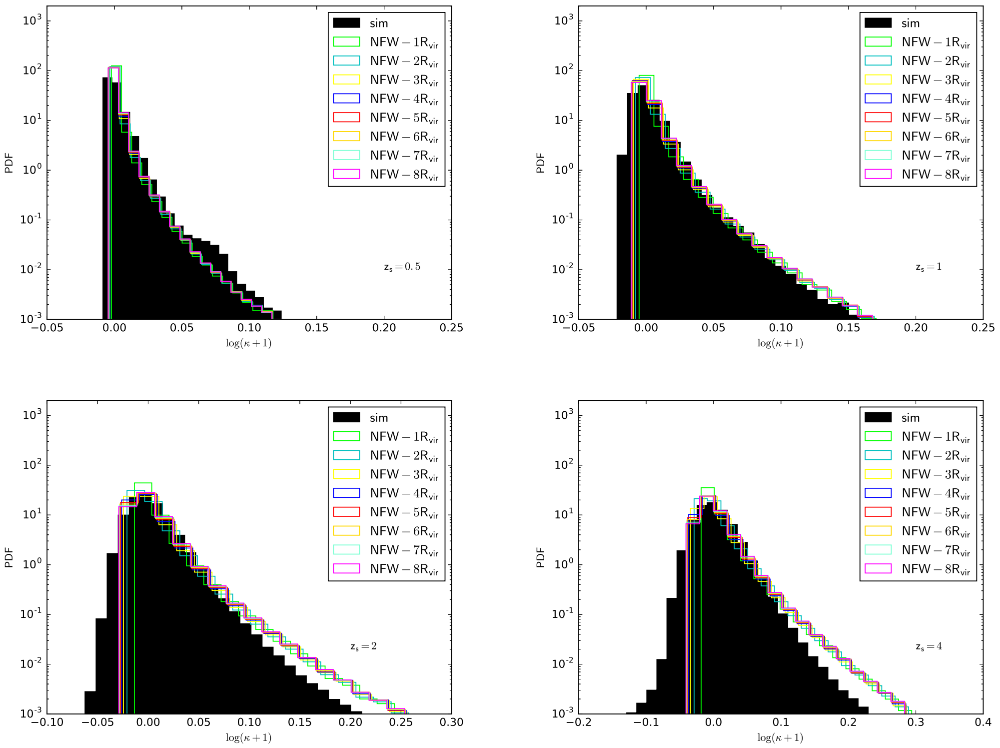

Figure 4.12: Comparison among the PDFs extracted from eight light cones produced with WL-MOKA, shown in different colors. The halos are modeled with the NFW profile extended from $1\,R_{vir}$ up to $8\,R_{vir}$ and come from the same ΛCDM catalogue. The PDFs coming from the light cones produced with the simulation are shown in black. The different panels refer to different source redshifts: top-left $z_S = 0.5$, top-right $z_S = 1$, bottom-left $z_S = 2$ and bottom-right $z_S = 4$.

In figure 4.13 we plotted the PDFs obtained from three light cones in which the halos are truncated at 5, 6 and 7 virial radii, and where the external slope of the density profile 4.5 is $\beta = 4$; in figure 4.14 we plotted the PDFs obtained from three light cones in which the halos extend up to 5 virial radii, and where the external slope of the density profile 4.5 changes among $\beta = 4, 5, 6$; finally in figure 4.15 we plotted the PDFs obtained from two light cones in which the halos are extended up to 6 virial radii, and where the external slope β of the density profile 4.5 varies between 3.5 and 4; in all these plots the sources are at $z_S = 4$ and we compared the PDFs with that obtained from the light cone with halos truncated at the virial radius (in green) and with that derived from the simulation (in black).

Increasing of the value of the external slope β from 3.5 to 6 produces PDFs more and more similar to that derived from the light cone populated with halos truncated at the virial radius. This suggests that it is important to have a good model able to describe not only the density profile of the halo, but also the profile of the environment of the halo, in order to predict a reasonable distribution of the matter and to better understand how the large scale structure arises from the over-position of the density field at different z.

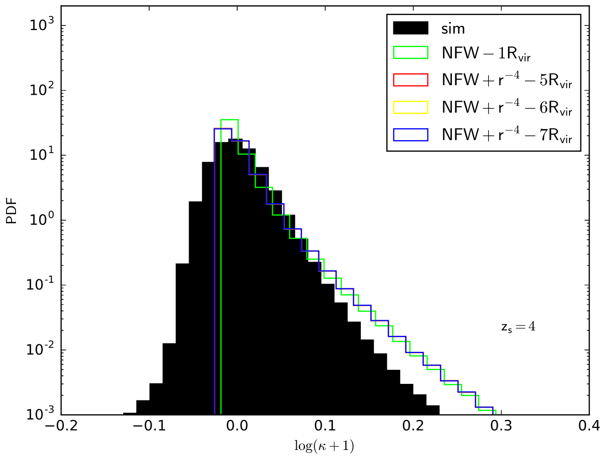

Figure 4.13: Comparison between the PDFs extracted from four light cones with sources at $z_S = 4$, populated with halos from the same ΛCDM catalogue. Halos are modeled with the NFW profile up to $1\,R_{vir}$ (green histogram). The red, yellow and blue histograms show the PDFs when the halo profile are described with a power law $\rho \propto r^{-4}$ from $1\,R_{vir}$ up to 5, 6 and $7\,R_{vir}$, respectively. The black histogram shows the PDF obtained from the CoDECS simulation.

In fact, as we can see in all the PDFs in figures 4.12, 4.13, 4.14, 4.15 and in particular in 4.16, in which we show the comparison between the simulation and the model with halos modeled with NFW profile and truncation radius equal to 5 virial radii, all the PDFs extracted from the light cones in which

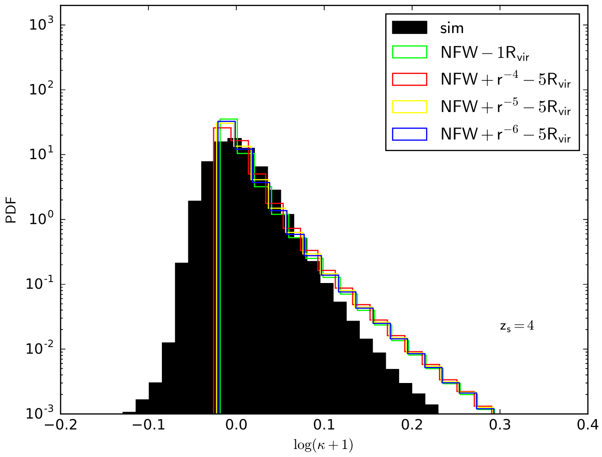

Figure 4.14: Comparison between the PDFs extracted from four light cones with sources at $z_S = 4$, populated with halos from the same ΛCDM catalogue. Halos are modeled with the NFW profile up to $1\,R_{vir}$ (green histogram). The red, yellow and blue histograms show the PDFs when the halos are truncated at $5\,R_{vir}$, and the slope β of the power law profile outside the virial radius assumes the values of 4, 5 and 6, respectively. The black histogram shows the PDF obtained from the CoDECS simulation.

Figure 4.15: Comparison among the PDFs extracted from three light cones with sources at $z_S = 4$, populated with halos from the same ΛCDM catalogue. Halos are modeled with the NFW profile up to $1\,R_{vir}$ (green histogram). The red and yellow histograms show the PDFs when the halos are truncated at $6\,R_{vir}$, and the slope β of the power law profile outside the virial radius assumes the values of 3.5 and 4, respectively. The black histogram shows the PDF obtained from the CoDECS simulation.

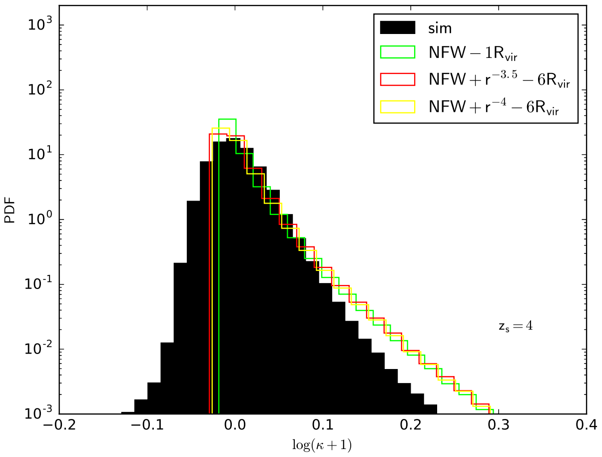

the halos, created with our code, are truncated at a given radius, are peaked, while the PDFs coming from light cones populated by particles are smoother. This is due to the fact that the latest have a pattern of convergence more homogeneous.

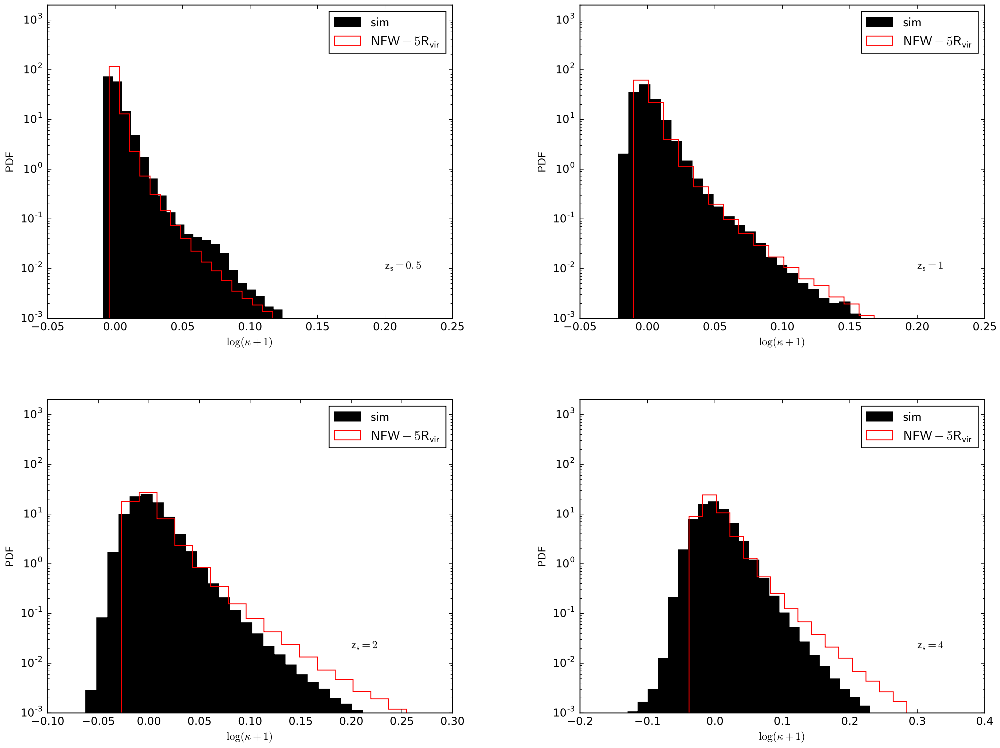

Figure 4.16: Probability distribution functions extracted from four light cones populated with halos from the same ΛCDM catalogue and sources at $z_S = 0.5$ (top-left), $z_S = 1$ (top-right), $z_S = 2$ (bottom-left) and $z_S = 4$ (bottom-right). The halos are modeled with the NFW profile extended up to $5\,R_{vir}$. The black histograms are the probability distribution functions extracted from the total convergence maps light cones derived from the simulation.

Based on this we can conclude that extending the halos to bigger radius produces PDFs smoother and smoother, due to the fact that the probability that the convergence field of an halo overlap the field of one another increases with the extension of the halo itself, producing on the maps a more and more homogeneous pattern of convergence.

4.5.2 Power spectrum

The power spectra obtained from the light cones generated with WL-MOKA whose halos are truncated at radii in the range $[1, 8]$ virial radii are shown with different colors in figure 4.17. The different panels refer to increasingly high source redshifts $z_S = 0.5, 1, 2, 4$, respectively. The solid blue line shows the result obtained from the CoDECS simulation.

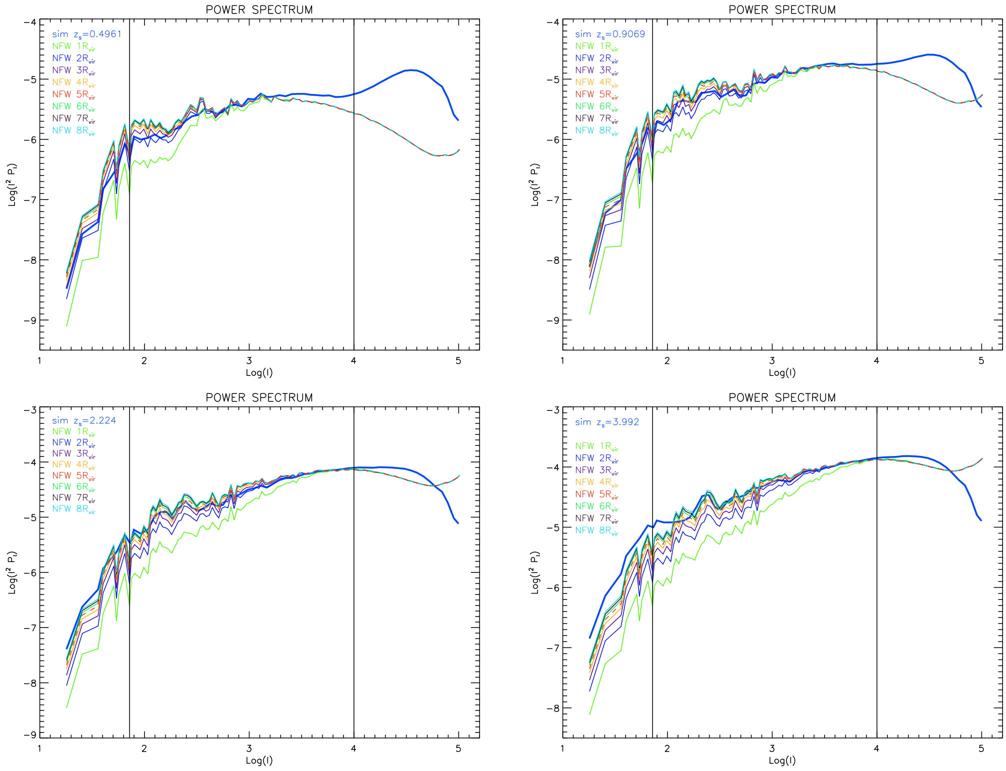

Figure 4.17: Comparison among the power spectra extracted from eight light cones populated with halos from the same ΛCDM catalogue and sources at $z_S = 0.5$ (top-left), $z_S = 1$ (top-right), $z_S = 2$ (bottom-left) and $z_S = 4$ (bottom-right). The halos are modeled with the NFW profile extended from $1\,R_{vir}$ up to $8\,R_{vir}$. The blue curve is the power spectrum extracted from a light cone populated by particles. The vertical lines refer to $\ell \sim 72$ which represents the limit of our map ($\theta = 5°$) and to $\ell = 10^4$.

The excess of power that we can observe at $\ell > 10^4$, indicated with a vertical black lines in all the panels, in the power spectra obtained from the light cones produced with the CoDECS simulation is due to particle noise, it affects all N-body simulations and it is due to the finite particle number, (Vale and White, 2003). The particle noise dominates at low redshift and decreases at higher ones. Instead, the power spectra derived from light cones filled with halos are shot-noise free, (Giocoli et al., 2015a). Furthermore, our maps have a limited aperture of $\theta = 5°$ and this is responsible for a lack of power at scales $\ell < 72$, we indicated the limit with a vertical black line in all the power spectrum plots. This effect is due to the fact that the dimension of the field of view fixes the minimum ℓ that it is possible to sample in the Fourier space. In addition to this, we noticed that truncating halos at the virial radius, light green curve in all the plots, produces a lack of power at scales $\ell < 10^4$ for all the considered source redshifts.

Also the power spectra obtained from light cones populated with halos modeled with the profile 4.5 predict less power with respect to the power spectra obtained from light cones produced with the simulation, at low ℓ (since for $\ell < 10^3$). For noticing this, see the figure 4.18 where we show the power spectra obtained from three light cones generated with WL-MOKA, in which the halos are truncated at 5, 6 and 7 virial radii, and where the slope of the external density profile is $\beta = 4$; the figure 4.19 in which we show the power spectra obtained from three light cones generated with WL-MOKA, with halos truncated at 5 virial radii, and where the slope of the external density profile changes in the range $\beta = 4, 6$; and the figure 4.20 where we plotted the power spectra obtained from two light cones generated with WL-MOKA, in which halos are truncated at 6 virial radii, and where the slope of the external density profile changes between 3.5 and 4. All these spectra are compared with the power spectra (in green) obtained from a light cone filled with halos modeled with the NFW profile up to the virial radius and with the power spectra (in blue) obtained from light cones produced by the simulation. The source redshift in these three plots is 4.
All these power spectra produced with WL-MOKA, are very different from those obtained form the simulation. In particular, we can observe that changing the extension of such halos does not affect the shape of the curve of the power spectrum, as it is possible to see in figure 4.18, while decreasing β in the slope of the power law in the external density profile produces an increasing of the power spectrum for $\ell < 10^4$, but not enough to reproduce the power spectrum of the simulation.

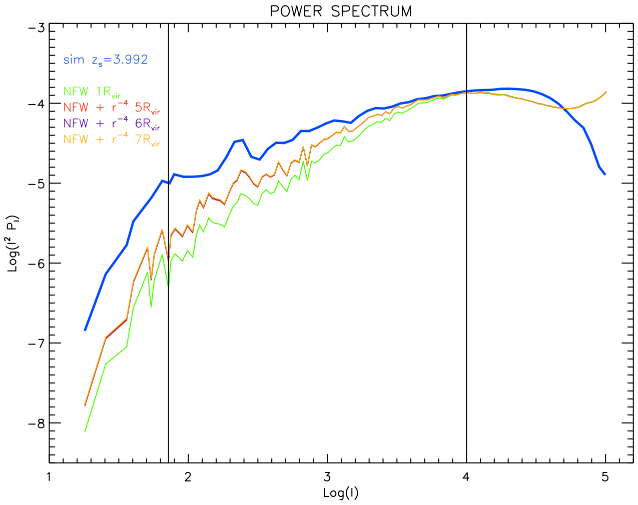

Figure 4.18: Comparison between the power spectra extracted from four light cones with sources at $z_S = 4$, populated with halos from the same ΛCDM catalogue. Halos are modeled with the NFW profile up to $1\,R_{vir}$ (green curve). The red, violet and orange curves show the power spectra when the halo profile are described with a power law $\rho \propto r^{-4}$ from $1\,R_{vir}$ up to 5, 6 and $7\,R_{vir}$, respectively. The blue line shows the power spectrum obtained from the CoDECS simulation.

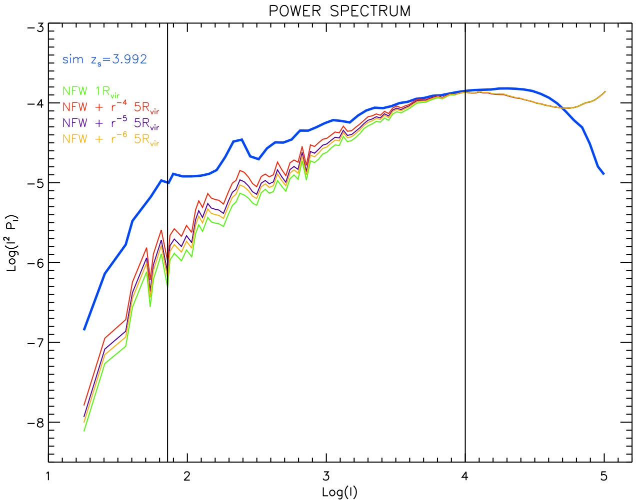

Figure 4.19: Comparison between the power spectra extracted from four light cones with sources at $z_S = 4$, populated with halos from the same ΛCDM catalogue. Halos are modeled with the NFW profile up to $1\,R_{vir}$ (green curve). The red, violet and orange curves show the power spectra when the halos are truncated at $5\,R_{vir}$, and the slope β of the power law profile outside the virial radius assumes the values of 4, 5 and 6, respectively. The blue line shows the power spectrum obtained from the CoDECS simulation.

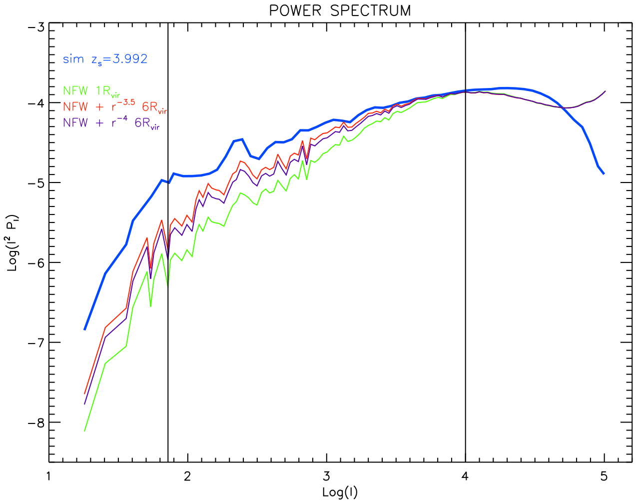

Figure 4.20: Comparison among the power spectra extracted from three light cones with sources at $z_S = 4$, populated with halos from the same ΛCDM catalogue. Halos are modeled with the NFW profile up to $1\,R_{vir}$ (green curve). The red and violet curves show the power spectra when the halos are truncated at $6\,R_{vir}$, and the slope β of the power law profile outside the virial radius assumes the values of 3.5 and 4, respectively. The blue curve shows the power spectrum derived from the CoDECS simulation.

This confirm what we said in section 4.5.1 about the importance of a model able to describe the density profile inside and outside the virial radius. Truncating halos at the virial radius or assuming that the density profile outside the virial radius is described by a power law predict not enough mass and underestimates the power spectrum since $\ell < 10^3$, in particular for very small ℓ that are related to big scales and so to large scale structure.

The best match with simulation results, in the range $72 < \ell < 10^4$, is for the spectra obtained from light cones populated with halos modeled only with the NFW profile, see e.g. the figure 4.21, in which we show the residual of the power spectra plotted in the bottom-right panel of the figure 4.17 ($z_S = 4$).

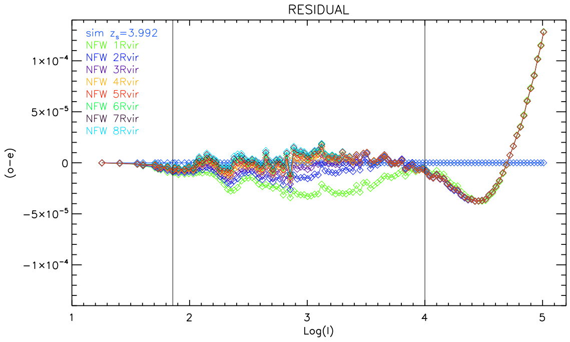

Figure 4.21: Residual of the power spectra plotted in the bottom-right panel of the figure 4.17 ($z_S = 4$). The horizontal blue curve is the referral power spectrum. The vertical lines refer to $\ell \sim 72$ which represents the limit of our map ($\theta = 5°$) and to $\ell = 10^4$.

Changing the extension of halos from 2 up to 8 virial radii produces differences among the power spectra obtained from light cones produced with WL-MOKAfor $\ell < 10^3$, which correspond to angular scales $\theta \gtrsim 21.5$ arcmin. For truncation radii up to 4 virial radii the power spectrum is still underestimated respect to that of the numerical simulation.

Analysing the ratios between the power spectra extracted from light cones populated with halos truncated at 5 and 6 virial radii and at 5 and 7 virial radii, shown in figure 4.22, we see that the P_ℓ extracted from the light cone populated with halos truncated at 6 virial radii is higher on the average, by $\sim [9-13]\%$ for $\ell \lesssim 316$ and by $\sim [0-9]\%$ for $316 < \ell \lesssim 3162$ with respect to that obtained from light cones filled with halos truncated at 5 virial radii; the differences with the P_ℓ obtained from the light cone with halos truncated at 7 virial radii is even higher: $\sim [17-25]\%$ for $\ell \lesssim 316$ and $\sim [0-17]\%$ for $316 < \ell \lesssim 3162$; for $\ell > 3162$ it is evident that the dimension of the halos does not influence significantly the power spectrum.

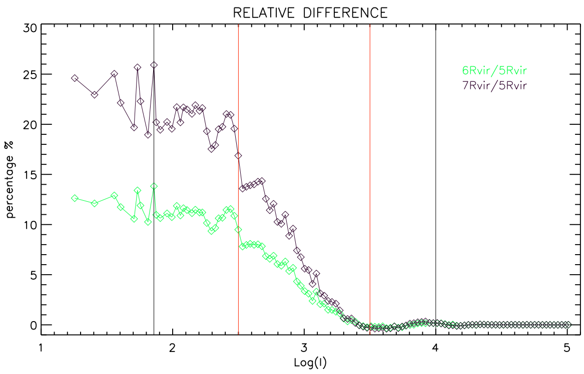

Figure 4.22: Relative differences calculated between the power spectra coming from light cones with halos extended up to 6 and $7\,R_{vir}$ and the power spectrum of the light cone with halos extended up to $5\,R_{vir}$. The vertical black lines refer to $\ell \sim 72$ (the limit of our map $\theta = 5°$) and to $\ell = 10^4$, while the red lines refer to $\ell \sim 316$ and $\ell \sim 3162$, where the ratios change significantly their slopes.

Given these results, the best trade-off is given by halos modeled with a NFW profile and truncated at 5 virial radii.

In figure 4.23 we show the comparison between the power spectra coming from the light cones realized wit WL-MOKA following the best match model and the power spectra coming from the light cones filled by particles with the simulation, the different panels refer to different source redshifts, namely $z_S = [0.5, 1, 2, 4]$.

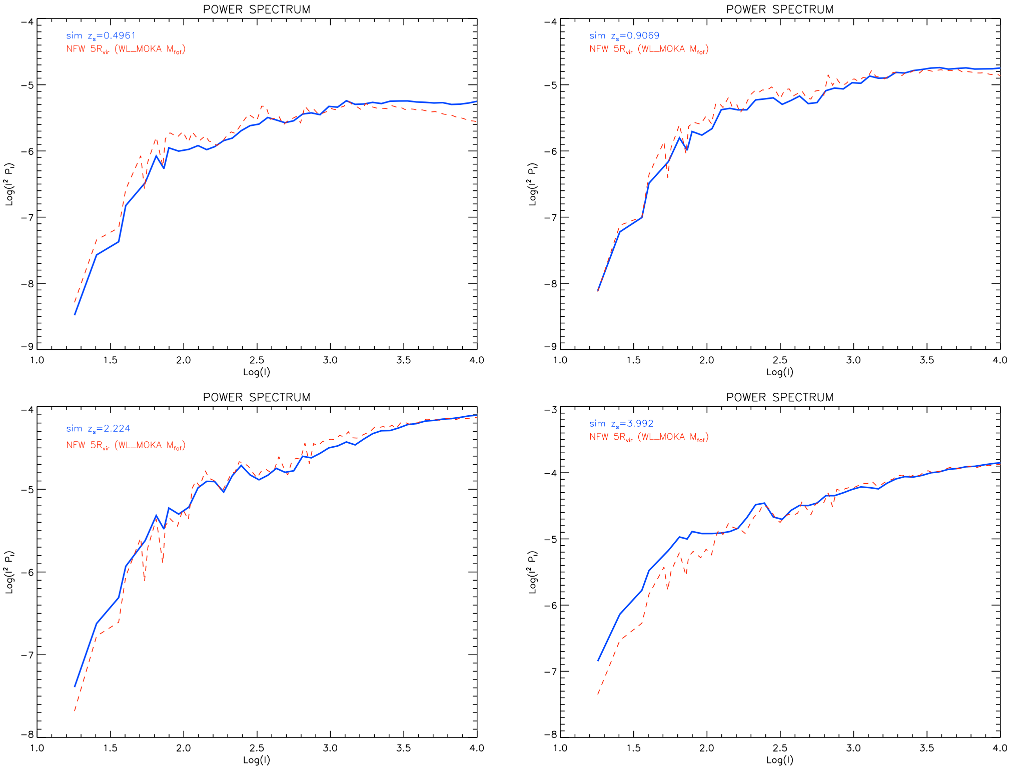

Figure 4.23: Power spectra (red dashed curves) extracted from four light cones populated with halos from the same ΛCDM catalogue and sources at $z_S = 0.5$ (top-left), $z_S = 1$ (top-right), $z_S = 2$ (bottom-left) and $z_S = 4$ (bottom-right). The halos are modeled with the NFW profile truncated at $5\,R_{vir}$. The blue curves are the power spectra extracted from the maps obtained from light cones produced with the CoDECS simulation.

4.6 Statistical analysis

Once we have performed all the tests necessary to fix our procedure and to find the best match model, we set up the required ingredients and quantities. Thus, we considered a sample of $N = 25$ different light cones of ΛCDM simulation and we applied the previous recipe to the different halo catalogues in order to produce several light cones and to extract the convergence total maps for each given source redshift.

We obtained the power spectra from the convergence maps, in figure 4.24 we show the mean power spectra (violet curves) ot the ΛCDM sample and the standard deviation (blue curves) for different source redshifts $z_S = [0.5, 1, 2, 4]$.

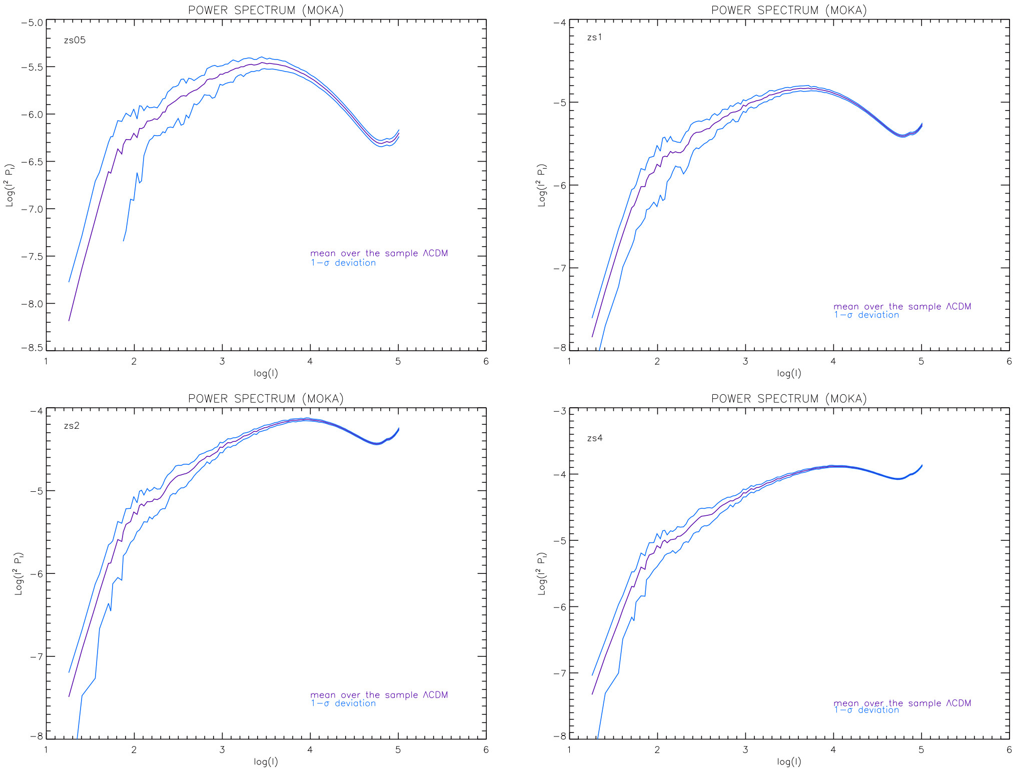

Figure 4.24: Mean of the power spectra produced by WL-MOKA on the ΛCDM sample. The different panels refer to different sources redshifts: $z_S = 0.5$ (top-left), $z_S = 1$ (top-right), $z_S = 2$ (bottom-left) and $z_S = 4$ (bottom-right). The blue curves represent the standard deviation of the sample from the average (violet curve) at 1-σ.

Then, we calculate the power spectrum covariance matrix, σ_{P_κ}, applying the definition 4.1 that we discussed in the sub-section 4.1.3, in the following way:

$$\sigma_{P_\kappa}(\ell,\ell') = \frac{1}{N}\sum_{h=1}^{N}(P_{\kappa,h}(\ell) - \bar{P}_\kappa(\ell))(P_{\kappa,h}(\ell') - \bar{P}_\kappa(\ell')), \tag{4.7}$$

where $P_{\kappa,h}(\ell)$ is the value of the h^{th} convergence power spectrum at a scale ℓ and $\bar{P}_\kappa(\ell)$ is the power spectrum mean value for a given ℓ. This matrix gives us the variation of each spectrum respect to the others. By definition σ_{P_κ} is symmetric and it has on the main diagonal the variance of the power spectrum for each scale, while out of diagonal we can read the covariance among the different scales.

In figure 4.25 we plot the variances of the power spectra sample produced by WL-MOKA, with different colors referring to the four different sources redshifts.

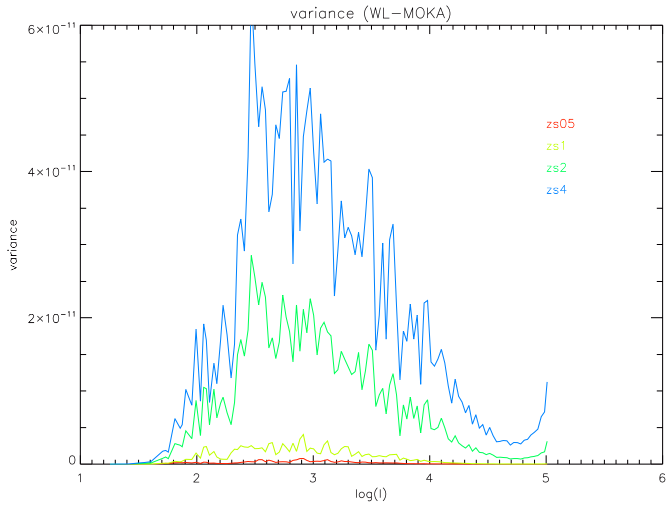

Figure 4.25: Variance in the power spectra sample produced by WL-MOKA for different source redshifts: red for $z_S = 0.5$, light green for $z_S = 1$, green for $z_S = 2$ and blue for $z_S = 4$.

In figure 4.26 we show the covariance matrices derived for four different source redshifts, $z_S = [0.5, 1, 2, 4]$.

We calculated that for $z_S = 0.5$ the 89.52 % of the pixels has a positive value, for $z_S = 1$ the percentage of positive pixels goes to 79.36 %, for $z_S = 2$ this value is 71.6 % and for $z_S = 4$ it is 71.06 %; in none of them there are pixels with zero covariance.

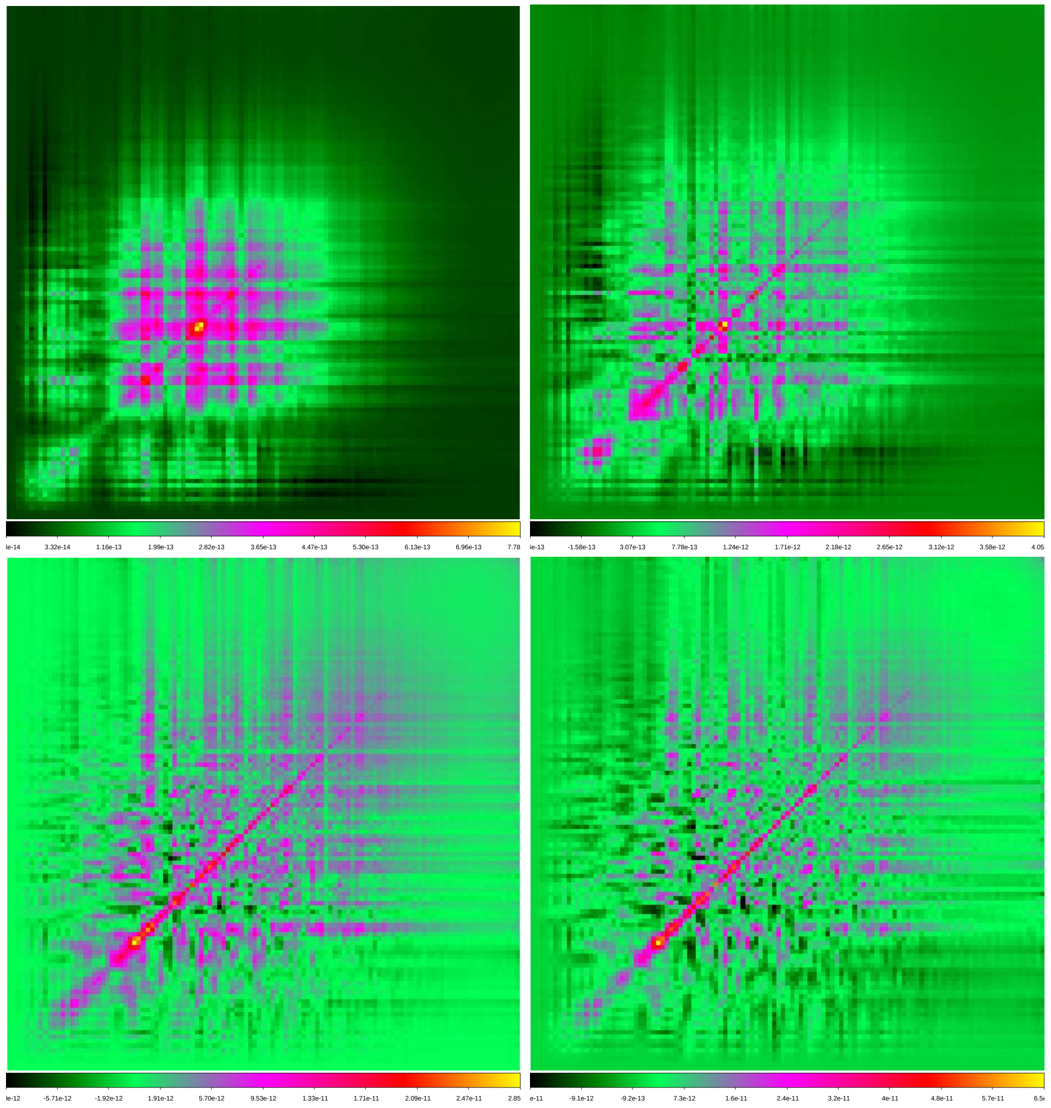

Figure 4.26: Covariance matrices derived from mock light cones generated with WL-MOKA, populated with dark matter halos from the ΛCDM catalogues, replicated for four different redshifts: top-right panel $z_S = 0.5$, top-left panel $z_S = 1$, bottom-right panel $z_S = 2$, bottom-left panel $z_S = 4$.

To make a comparison we calculated the power spectrum covariance matrix for the power spectra extracted from the convergence maps of the light cones produced by the simulation.

The mean power spectra (violet curves) of the sample produced with the simulation and the standard deviation (blue curves) are shown in figure 4.27 for different source redshifts $z_S = [0.5, 1, 2, 4]$,.

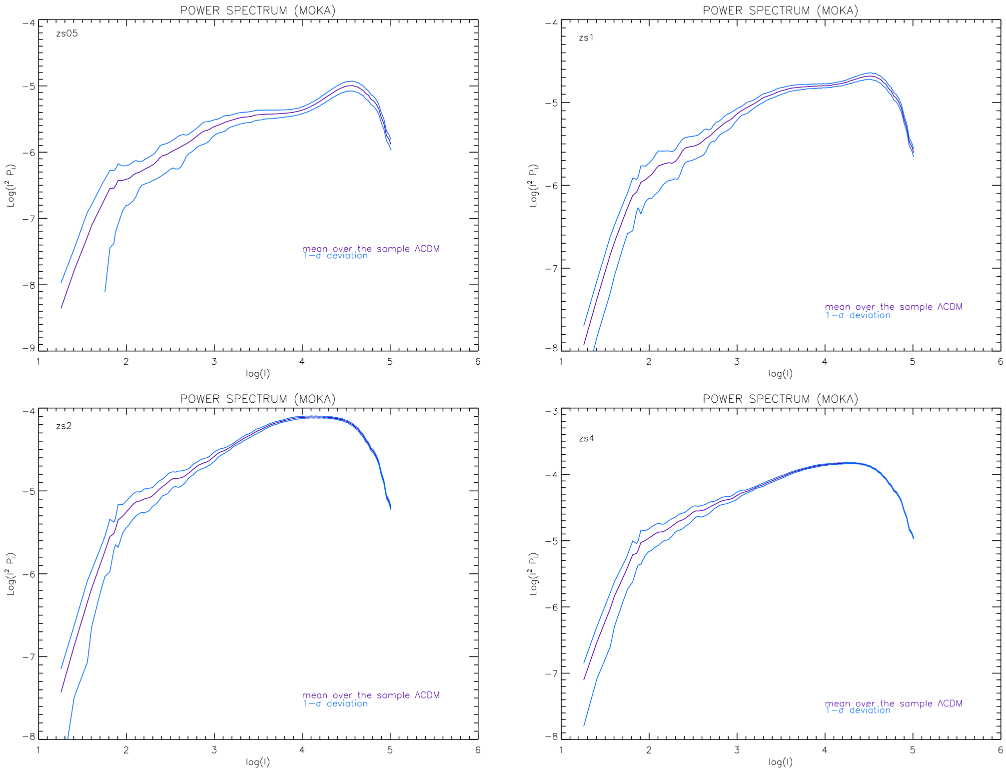

Figure 4.27: Mean of the power spectra produced by the simulation on the ΛCDM sample. The different panels refers to different sources redshifts: $z_S = 0.5$ (top-left), $z_S = 1$ (top-right), $z_S = 2$ (bottom-left) and $z_S = 4$ (bottom-right). The blue curves represent the standard deviation of the sample from the average (violet curve) at 1-σ.

In figure 4.28 we show the covariance matrices, derived from the simulation, calculated for four different source redshifts, $z_S = [0.5, 1, 2, 4]$. We counted that for $z_S = 0.5$ the 96.08 % of the pixels has a positive value, for $z_S = 1$ the percentage of positive pixels goes to 86.40 %, for $z_S = 2$ this value is 75.35 % and for $z_S = 4$ it is 70.56 %; in none of them there are pixels with zero covariance.

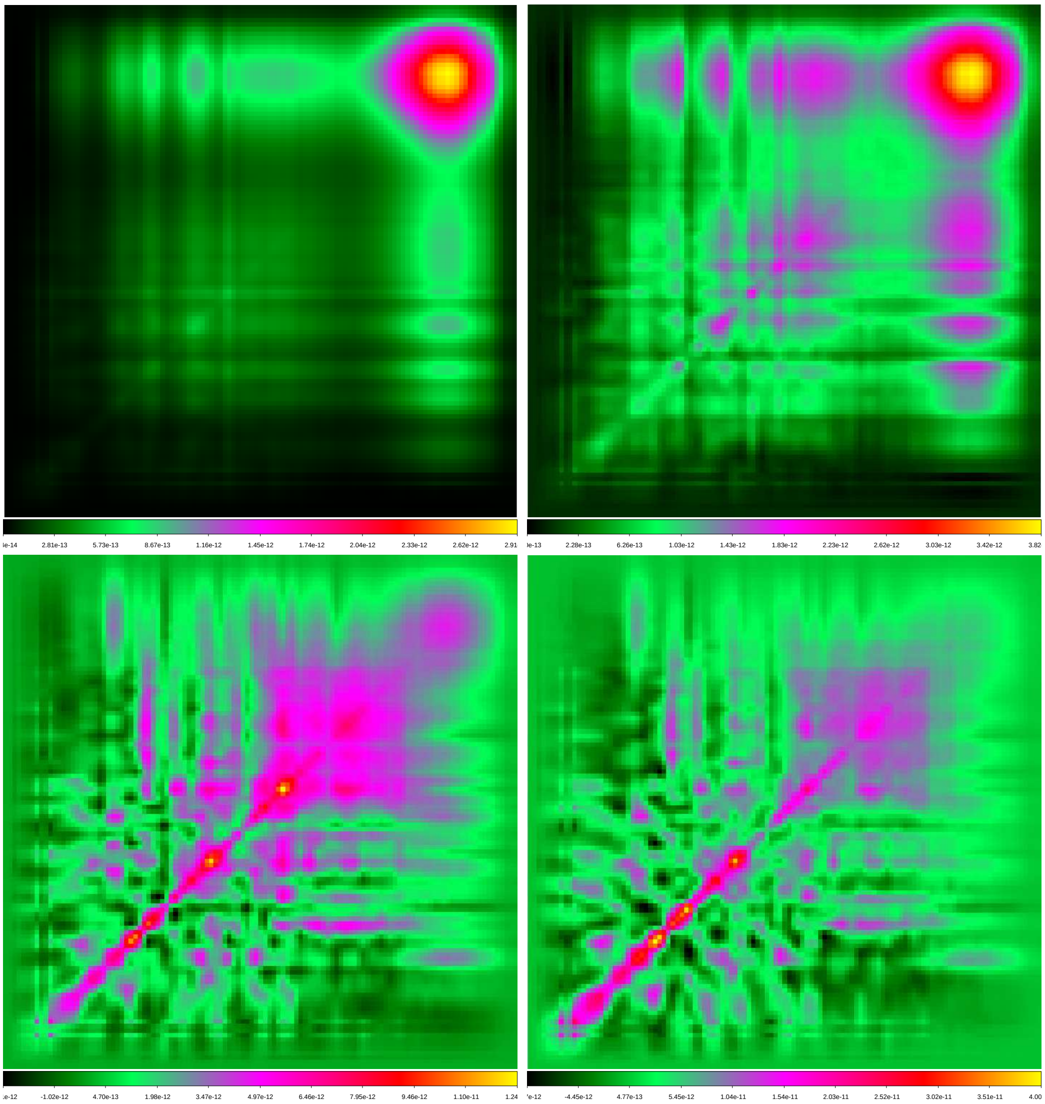

Figure 4.28: Covariance matrices derived from mock light cones produced by the CoDECS simulation, replicated for four different redshifts: top-right panel $z_S = 0.5$, top-left panel $z_S = 1$, bottom-right panel $z_S = 2$, bottom-left panel $z_S = 4$.

In figure 4.29 we show the variances in the sample of power spectra produced by the simulation, for the four different source redshifts, indicated with different colors.

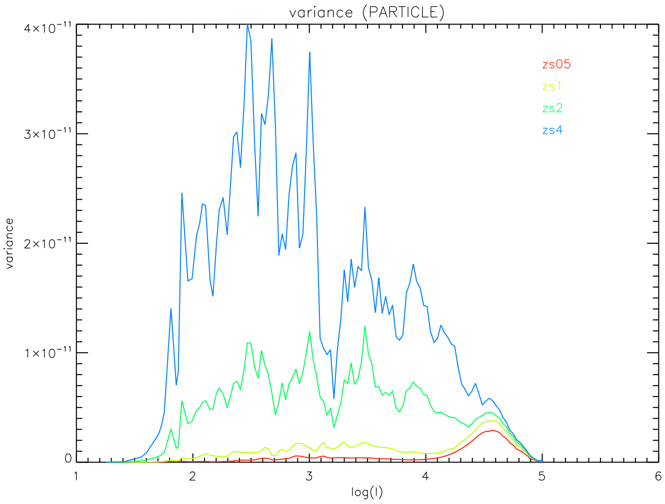

Figure 4.29: Variance in the power spectra sample produced by the CoDECS simulation, for different source redshifts: red for $z_S = 0.5$, light green for $z_S = 1$, green for $z_S = 2$ and blue for $z_S = 4$.

In order to better visualize the covariance between different scales, we calculated the cross-correlation coefficient matrix, ρ_{P_κ}, adapting the definition 4.2 explained in the sub-section 4.1.4 in the case of power spectra:

$$\rho_{P_\kappa}(\ell,\ell') = \frac{\sigma_{P_\kappa}(\ell,\ell')}{\sqrt{\sigma_{P_\kappa}(\ell,\ell)\sigma_{P_\kappa}(\ell',\ell')}}. \tag{4.8}$$

The matrix 4.8 states a possible relation of linearity between the terms, but it does not contain information about the variances.

We compared in figure 4.30 the ρ_{P_κ} derived from the covariance matrices (left panels) shown in figure 4.26 and those derived from the matrices in figure 4.28 (right panels), at different sources redshifts, $z_S = [0.5, 1, 2, 4]$ respectively.

In the case of the power spectra sample derived from light cones created with WL-MOKA, we refer to the left panels in figure 4.30, we observe that there is an increasing of the number of scales which are in strong correlation with the decreasing of the source redshift. This means that at low redshift the correlation arises at bigger and bigger scales (lower and lower ℓ) than at higher redshift. In the case of the sample produced with the simulation, shown in the right panels of the same figure, we noticed a similar trend.

In particular, we have that in the case of the WL-MOKA sample, the cross-correlation coefficient matrix for $z_S = 0.5$ shows a strong direct correlation for

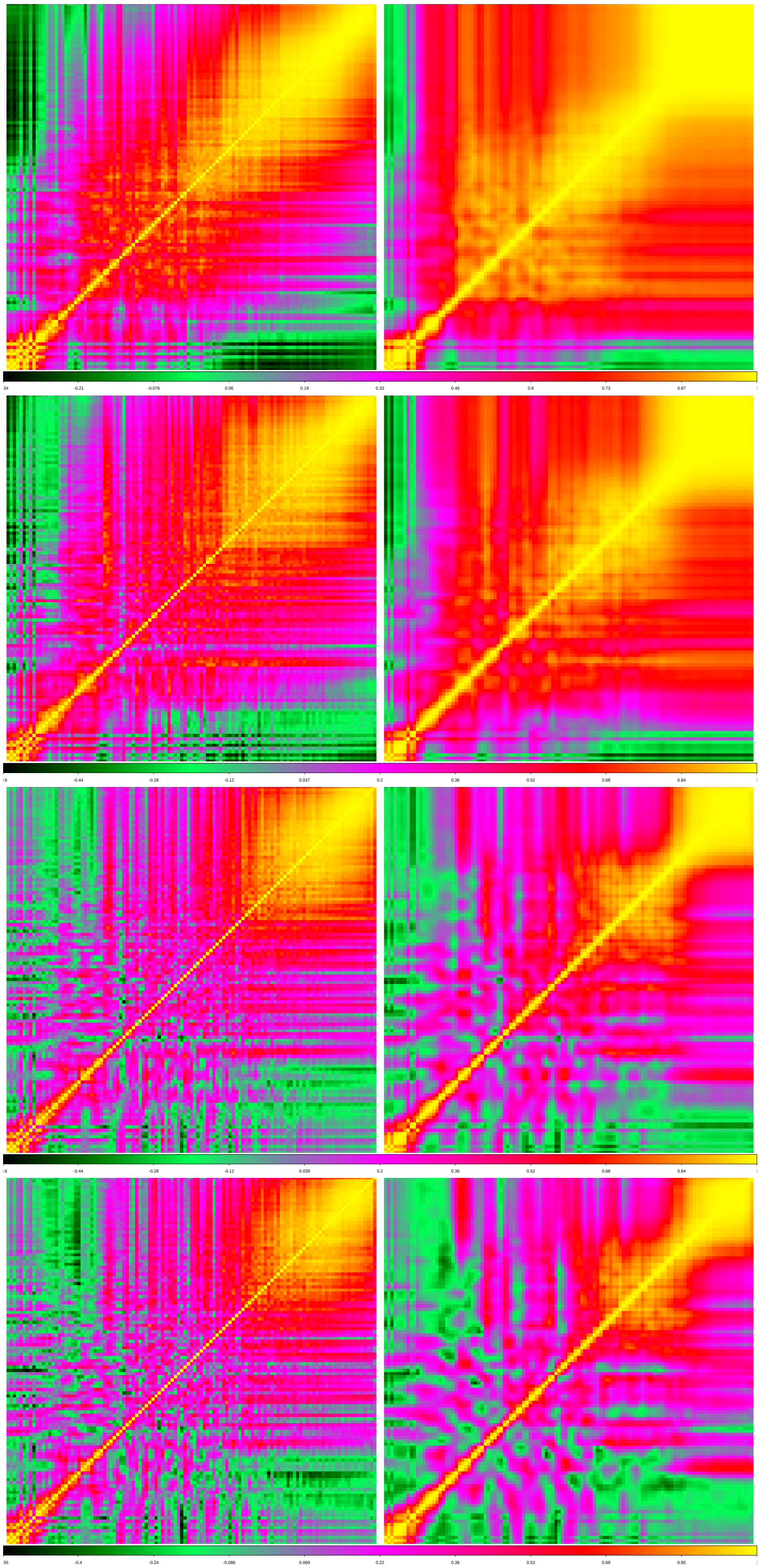

Figure 4.30: Cross-correlation coefficient matrices derived from mock light cones populated by dark matter halos, on the left, compared with those derived from the simulation. The source redshifts are, from the top, $z_S = [0.5, 1, 2, 4]$, respectively.

the 31.85 % of the pixels; for $z_S = 1$ the percentage is 20.49 %; for $z_S = 2$ it is 12.77 % and finally for $z_S = 4$ the 11.21 % of ℓ are strongly correlated.
Instead, in the simulation sample the cross-correlation coefficient matrix for $z_S = 0.5$ shows a strong direct correlation for the 61.87 % of the pixels; for $z_S = 1$ the percentage is 36.08 %; for $z_S = 2$ it is 13.49 % and finally for $z_S = 4$ the 11.64 % of ℓ are strongly correlated. The percentages of the pixels belonging to every type of correlation are listed in table 4.4, while the trends of the percentages for each source redshifts for both the case of WL-MOKA and the simulation can be better visualized in figure 4.31.

	WL-MOKA	sim	WL-MOKA	sim
	$z_S = 0.5$		$z_S = 1$	
strong	31.85 %	61.87 %	20.49 %	36.08 %
moderate	37.47 %	23.94 %	37, 74 %	40.64 %
weak	20.20 %	10.18 %	21.13 %	12.68 %
	$z_S = 2$		$z_S = 4$	
strong	12.77 %	13.49 %	11.21 %	11.64 %
moderate	25.45 %	33.18 %	24.94 %	27.80 %
weak	33.39 %	28.68 %	34.91 %	31.12 %

Table 4.4: List of the percentages of pixels in the cross-correlation coefficient matrices derived from WL-MOKA and from the simulation, of each kind of correlation among the scales for each redshift of interests.

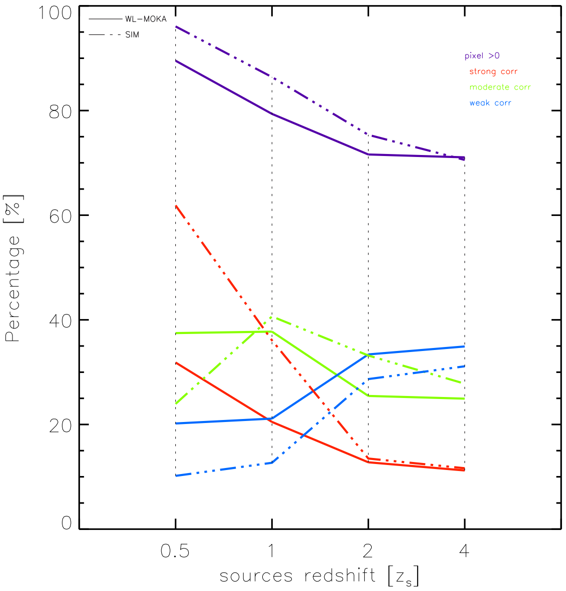

Figure 4.31: Trends of percentages of the pixels in the cross-correlation coefficient matrices for each kind of correlation with respect to the source redshift. The dash-dotted lines refer to the simulation, the solid lines refer to WL-MOKA; the violet lines refer to the percentage of correlated pixels, the red lines identify strong correlation, the green lines refer to moderate correlations and the blue lines are for the weak correlations.

We note that the cross-correlation coefficient matrices are almost diagonal for low ℓ (large scales) and the measures become strongly correlated for high ℓ (smaller scales) in both cases; in particular we note that the ℓ on which the strong correlation arises is higher and higher with the increasing of the source redshift, in particular for the power spectra sample produced by WL-MOKA we have $\ell \sim 10^3$ for $z_S = 0.5$ up to $\ell \sim 10^4$ for $z_S = 4$, while in the other case the correlation arises at very big scales $z_S = 0.5$ and at slightly bigger scales with respect to the sample produced with WL-MOKA for $z_S = 4$.
The strong correlation that we observe at low redshift is due to the intrinsic variance of the halos, in fact we are sampling the inner region of the clusters that are self similar, but at high redshift the intrinsic variance of the halos is still dominating, because the sample we considered is too small.

4.7 Second sample

We proceeded in our work by analysing a different simulation, called ΛCDM-HS8. It consists of 25 different catalogues with the same cosmological parameters of the ΛCDM simulation and with a higher value of $\sigma_8 = 0.987$.

Applying the previous recipe, we generated 25 mock light cones, with source distributed on several redshifts, $z_S = [0.5, 1, 2, 4]$. From these light cones we extracted the convergence maps. An example of the total convergence maps, obtained from four different light cones populated with halos modeled with NFW profile and with a truncation radius equal to 5 virial radii, performed starting from the same catalogue for four different source redshifts, is shown in figure 4.32 on the left panels, compared with the convergence maps, on the right panels, obtained from four light cones produced by the simulation, with the same z_S.

As pointed out during the ΛCDM sample analysis, see sub-section 4.4.2, with our treatment of the LSS as an ensemble of dark matter clumps, we are not able to describe the filaments, but we can reproduce the signal of the large scale structure as the super-position of the convergence fields due to each halos, in fact looking at the compared maps we can recognize the same structures at all redshifts.

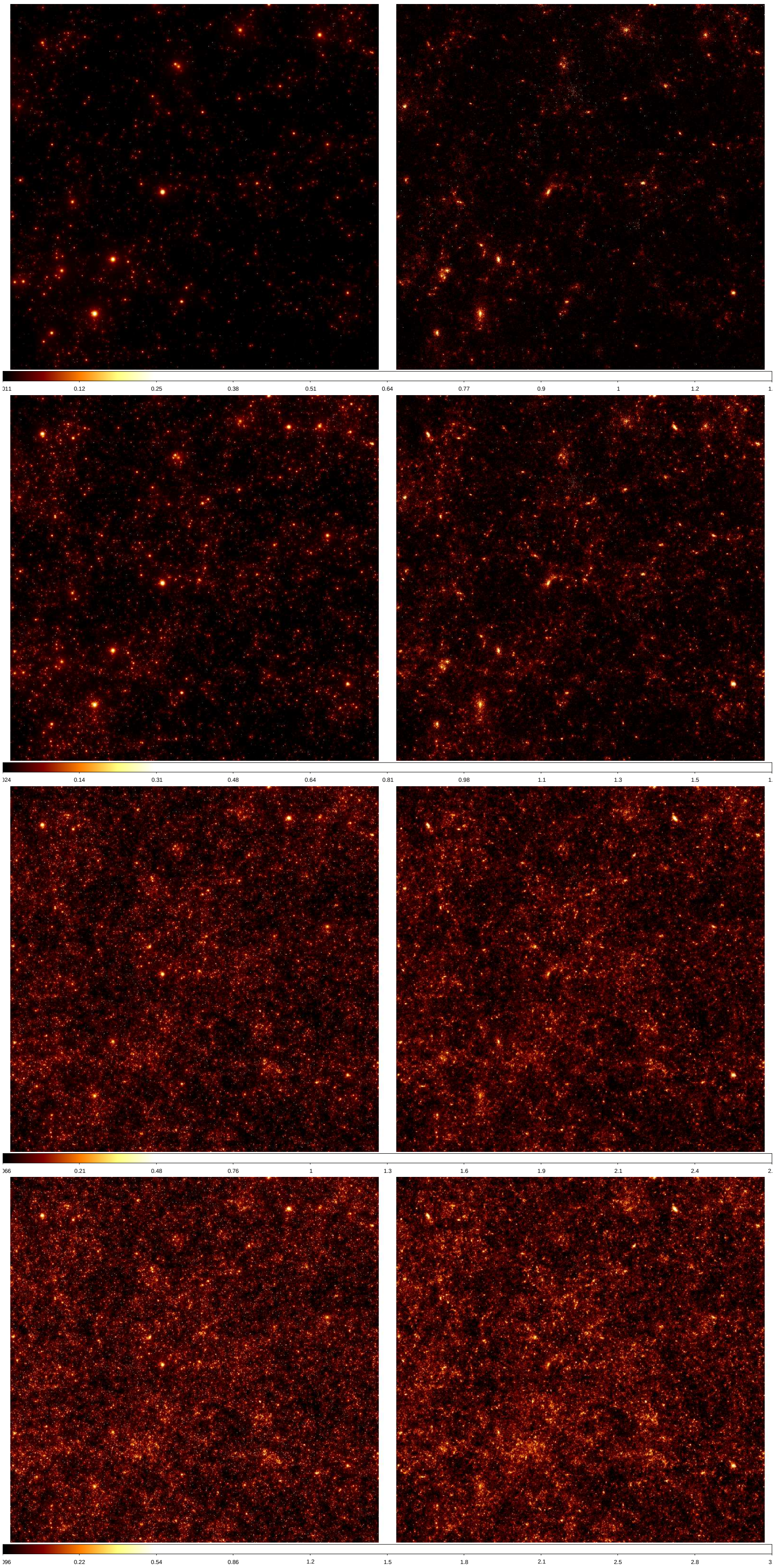

Figure 4.32: Convergence maps derived from mock light cones populated by dark matter halos produced with WL-MOKA, on the left panel, and produced by the simulation, on the right panels. The catalogue is the same and come from the ΛCDM-HS8 simulation. The source redshifts, from the top, are: $z_S = 0.5$, $z_S = 1$, $z_S = 2$ and $z_S = 4$.

From each map we extracted the power spectrum of the convergence. In figure 4.33 we show the average spectrum (violet curve) for each source redshift, with the standard deviation (blue curves) at 1-σ of the entire power spectra sample derived from the convergence maps of the light cones filled with dark matter halos produced with WL-MOKA.

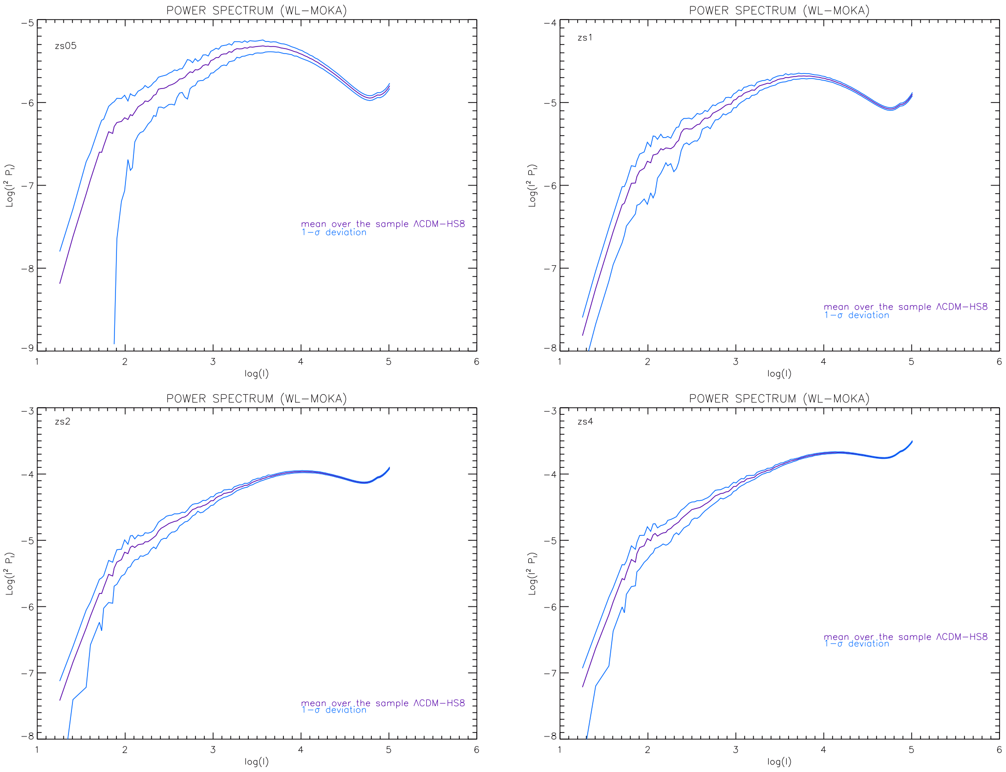

Figure 4.33: Mean (violet curve) of the power spectra produced by WL-MOKA on the ΛCDM-HS8 sample. The sources redshifts are: top-right panel $z_S = 0.5$, top-left panel $z_S = 1$, bottom-right panel $z_S = 2$, bottom-left panel $z_S = 4$. The blue curves represent the standard deviation of the sample from the average at 1-σ.

From the power spectra shown in figures 4.33, we extracted the power spectrum covariance matrix, σ_{P_κ}, by calculating the equation 4.7 with the new sample. The covariance matrices in figure 4.34 have been calculated for four different source redshifts. The percentages of positive pixels, meaning a direct correlation among the correspondent scales, are the 92.13 % for $z_S = 0.5$, the 84.38 % for $z_S = 1$, the 73.30 % for $z_S = 2$ and for $z_S = 4$ it is the 70.91 %; pixels with zero covariance are not present in any matrix.

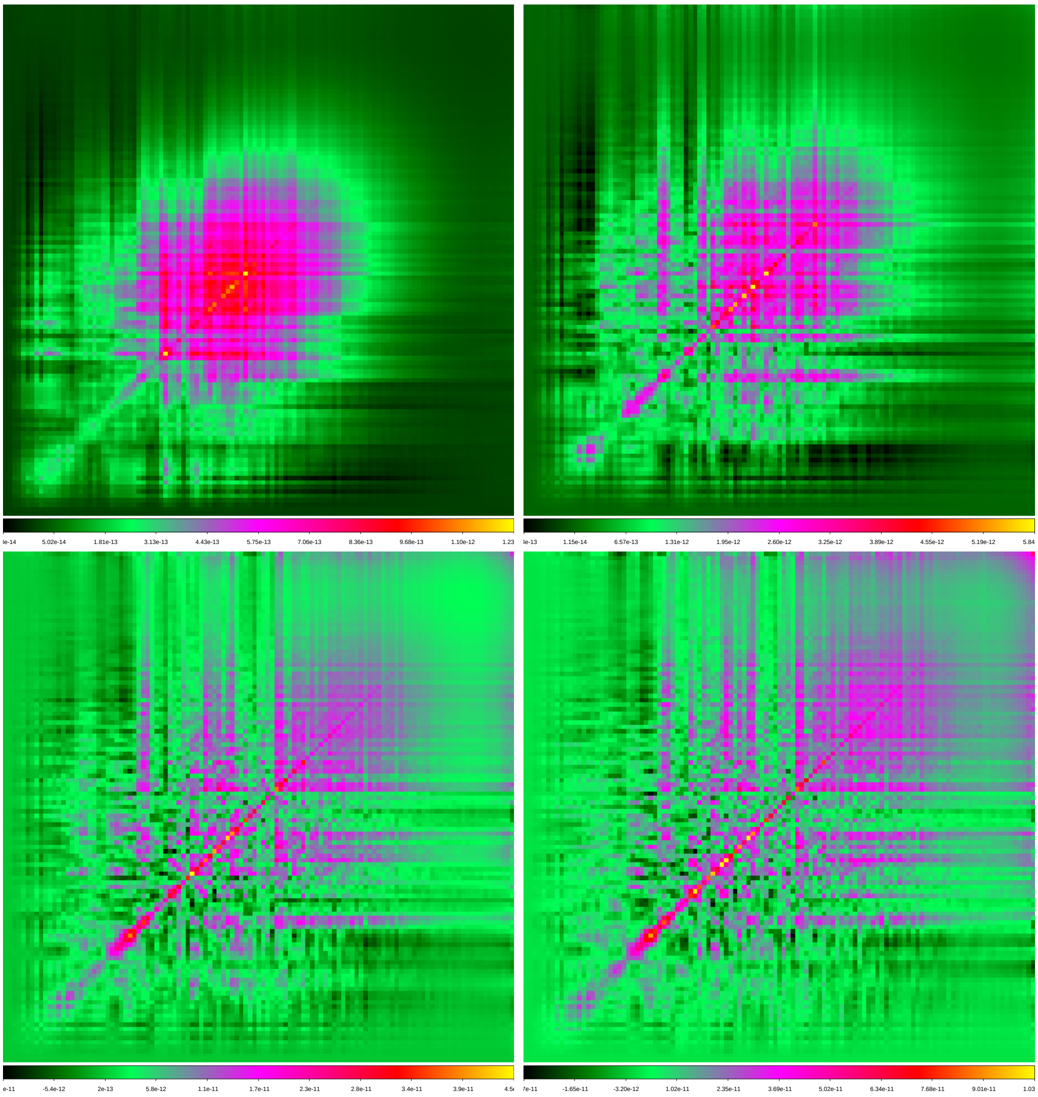

Figure 4.34: Covariance matrices derived from mock light cones populated with dark matter halos generated with WL-MOKA, in which the catalogues come from the ΛCDM-HS8 set, replicated for four different redshifts: top-right panel $z_S = 0.5$, top-left panel $z_S = 1$, bottom-right panel $z_S = 2$, bottom-left panel $z_S = 4$.

In figure 4.35 we plot the variances of the power spectra of the ΛCDM-HS8 sample produced by WL-MOKA, different sources redshifts are indicated with different colors.

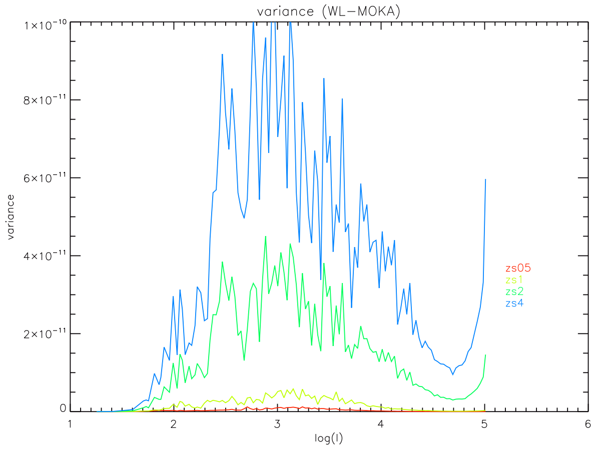

Figure 4.35: Variance in the power spectra of the ΛCDM-HS8 sample produced by WL-MOKA for different source redshifts: red for $z_S = 0.5$, light green for $z_S = 1$, green for $z_S = 2$ and blue for $z_S = 4$.

To make a comparison we calculated the power spectrum covariance matrices with the power spectra extracted from the convergence maps of the light cones produced by the ΛCDM-HS8 simulation. In figure 4.36 we plot the average power spectra (violet curve) of the ΛCDM-HS8 sample produced by the simulation with the standard deviation at 1-σ (blue curves), the different panels refer to different source redshifts.

We can note in figure 4.36 the presence of the bump in the power spectrum at very big ℓ, that we explained in sub-section 4.5.2 with the presence in simulation of the particle shot noise, which dominates at those scales.

In figure 4.37 we show the covariance matrices calculated for four different source redshifts, $z_S = [0.5, 1, 2, 4]$, for light cones generated by the simulation. We counted that for $z_S = 0.5$ the 99.41 % of the pixels has a positive value, for $z_S = 1$ the percentage of positive pixels is 89.95 %, for $z_S = 2$ this value goes to 75.91 % and for $z_S = 4$ it is 71.36 %; in none of them there are pixels with zero covariance.

In figure 4.38 we show the variances in the simulated power spectra sample, the different colors indicate the four different source redshifts.

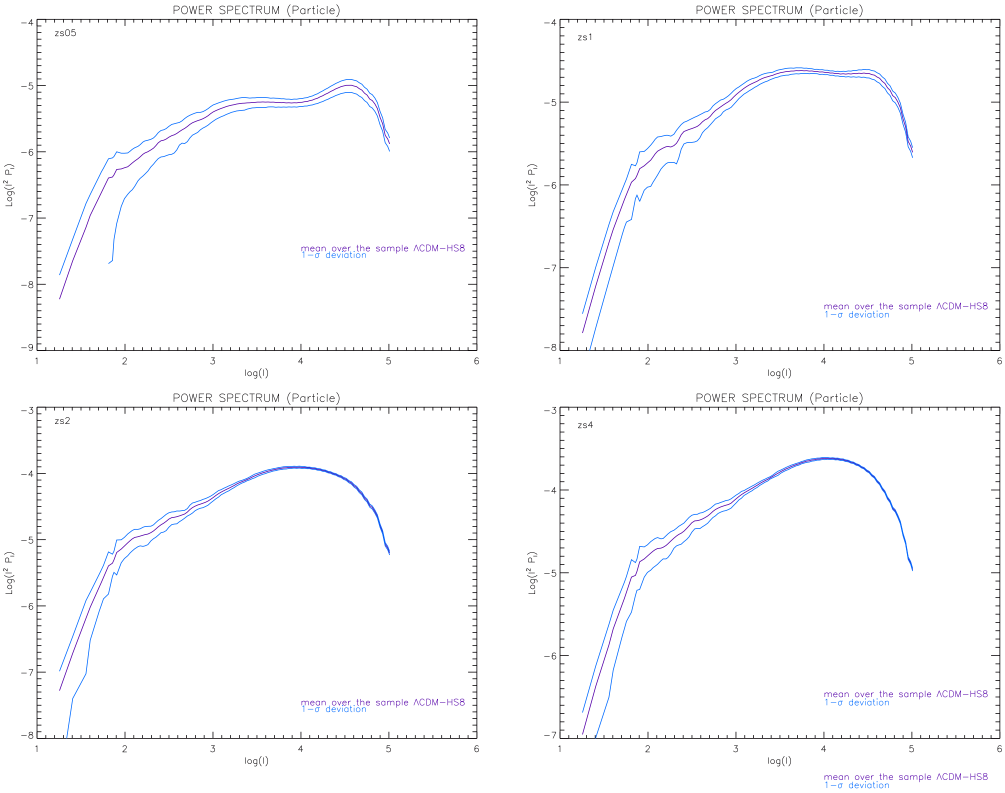

Figure 4.36: Mean (violet curve) of the power spectra obtained from light cones produced by the ΛCDM-HS8 simulation. The sources redshifts are: top-right panel $z_S = 0.5$, top-left panel $z_S = 1$, bottom-right panel $z_S = 2$, bottom-left panel $z_S = 4$. The blue curves represent the standard deviation of the sample from the average at 1-σ.

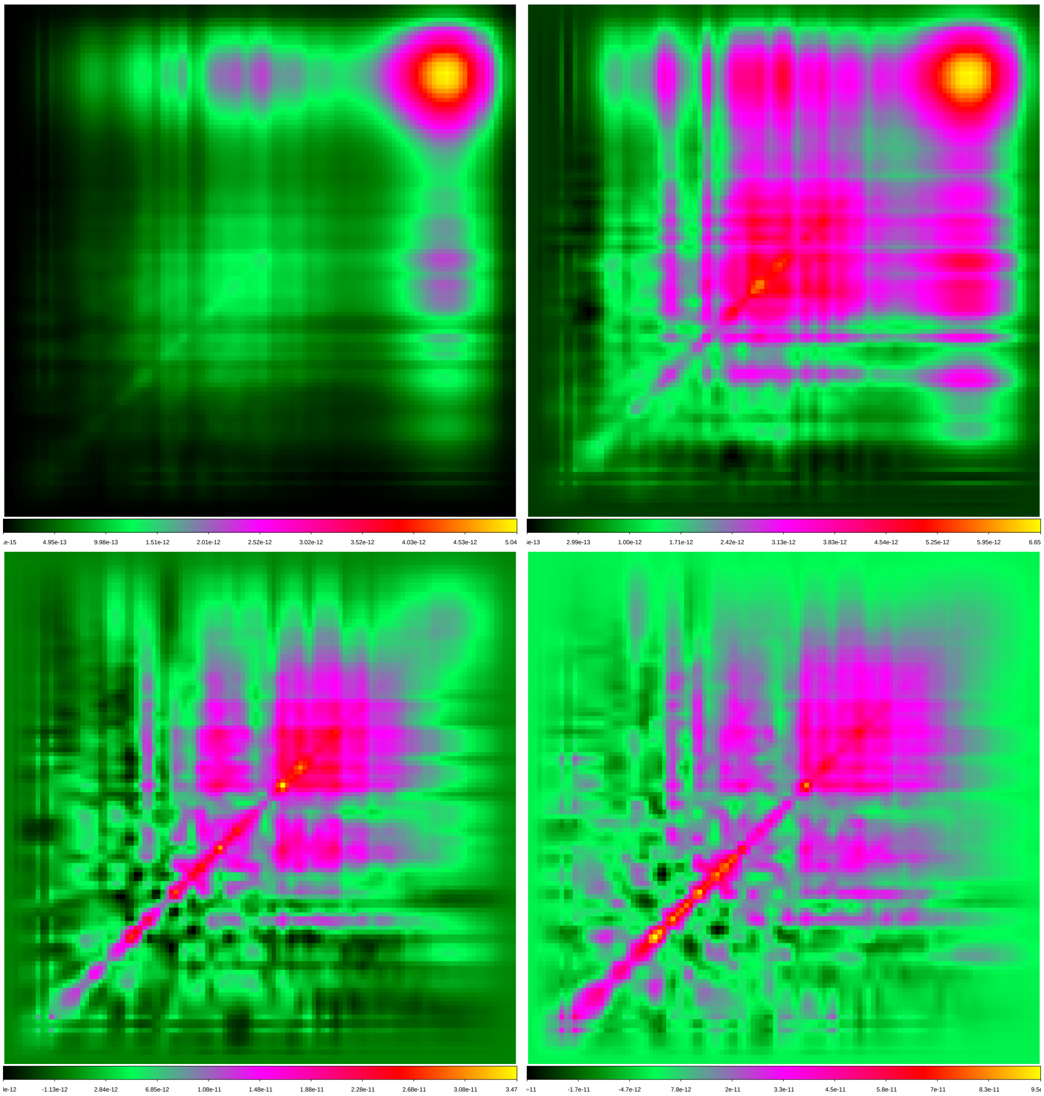

Figure 4.37: Covariance matrices calculated starting from the convergence power spectra derived from mock light cones produced by the simulation, from the ΛCDM-HS8 set, replicated for four different redshifts: top-right panel $z_S = 0.5$, top-left panel $z_S = 1$, bottom-right panel $z_S = 2$, bottom-left panel $z_S = 4$.

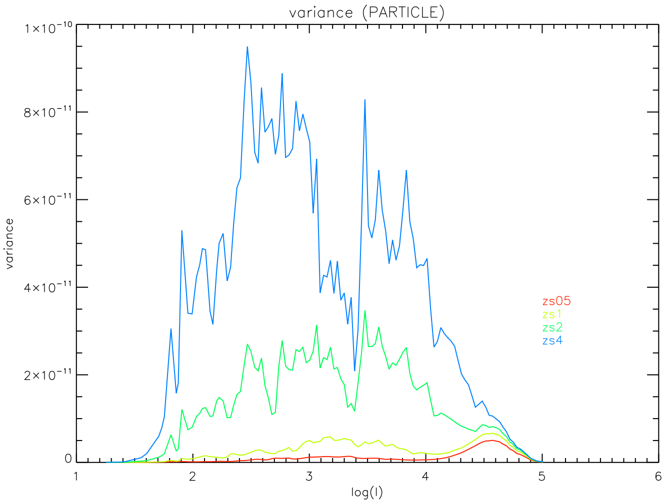

Figure 4.38: Variance in the power spectra of the ΛCDM-HS8 sample produced by the simulation, for different source redshifts: red for $z_S = 0.5$, light green for $z_S = 1$, green for $z_S = 2$ and blue for $z_S = 4$.

Then, we proceeded by calculating the cross-correlation coefficient matrices to underline the covariance between different scales. The matrices have been calculated by using the equation 4.8. The comparison between the ρ_{P_κ}, in the left panels, derived from the covariance matrices shown in figure 4.34, and those, in the right panels, derived from the matrices in figure 4.37, at different sources redshifts, $z_S = [0.5, 1, 2, 4]$, from the top respectively, is shown in figure 4.39 and confirms what we gathered during the analysis of the ΛCDM simulation.

In the case of the power spectra sample derived from light cones created with WL-MOKA, we refer to the left panels in figure 4.39 and we observe, as it happened in sub-section 4.6, an inverse relation between the number of strongly correlated scales and the source redshift, this means that at lower z_S the strong correlation involves a greater number of scales. And the same inverse relation is observed for the sample coming from the simulation, shown in the right panels of the same figure. As we said in the sub-section 4.6, this means that at lower redshift the correlation arises at bigger scales.

We can read the percentages of pixels of the cross-correlation coefficient matrices in which we have the strong correlation.
In the sample produced by WL-MOKA, at $z_S = 0.5$ we have that the 33.04 % of the pixels are strongly correlated; at $z_S = 1$ the percentage is 23.57 %; at $z_S = 2$ it is 14.13 % and finally at $z_S = 4$ we have that the strongly correlated ℓ are the 12.20 %.

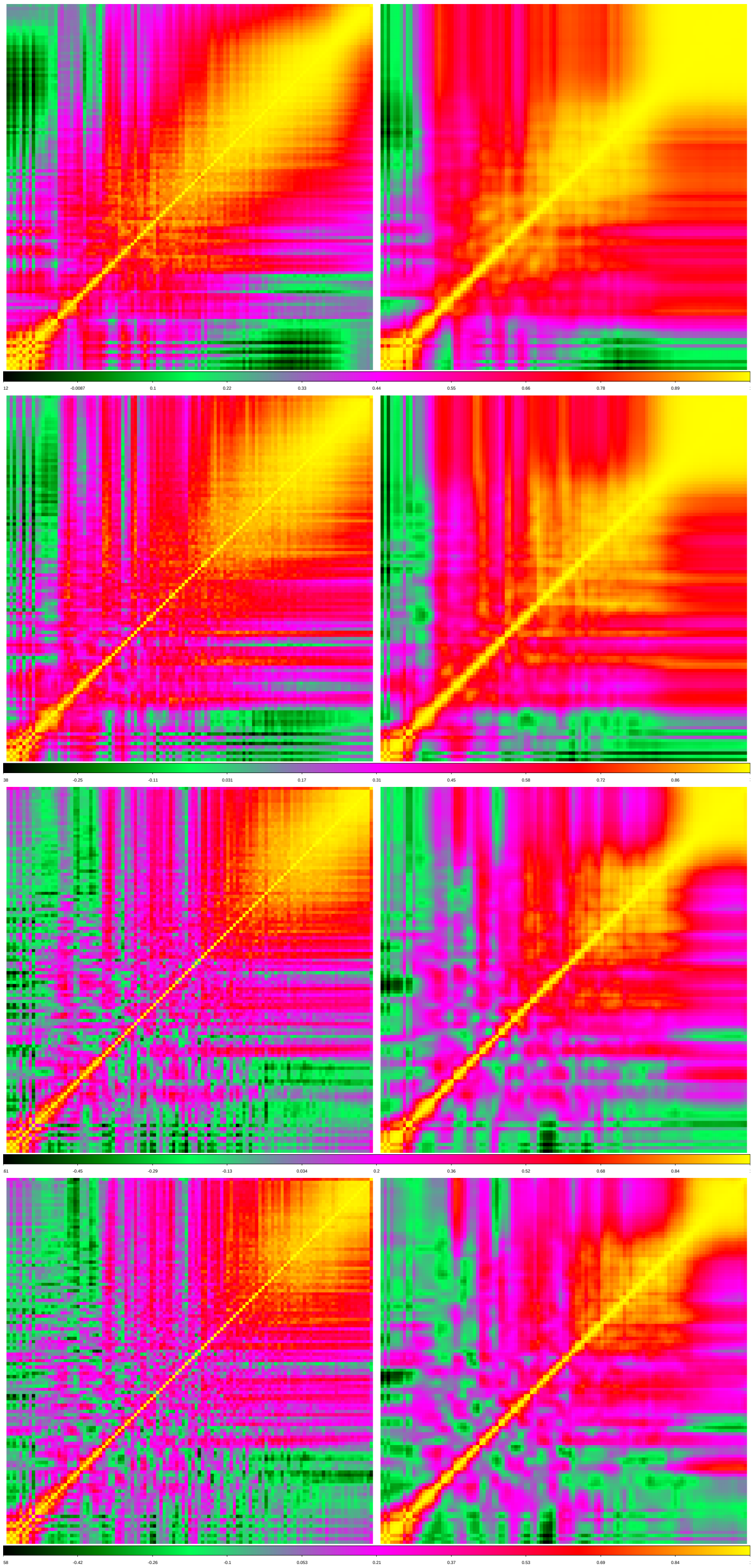

Figure 4.39: Cross-correlation coefficient matrix derived from mock light cones populated by dark matter halos generated with WL-MOKA, on the left, compared with one derived from the simulation, on the right. The source redshift, from the top, are: $z_S = 0.5$, $z_S = 1$, $z_S = 2$ and $z_S = 4$. The catalogues come from the ΛCDM-HS8 set.

Instead, in the sample created by the simulation, at $z_S = 0.5$ the cross-correlation coefficient matrix shows a strong direct correlation for the 54.57 % of the pixels; at $z_S = 1$ the percentage is 36.23 %; at $z_S = 2$ it is 14.99 % and at $z_S = 4$ the 12.94 % of ℓ are strongly correlated.

In table 4.5 we list the percentages of the pixels belonging to weak, moderate and strong correlation for all redshift, and the trends of the percentages for each source redshifts for both the case of WL-MOKA and the ΛCDM-HS8 simulation can be better visualized in figure 4.40.

	WL-MOKA	sim	WL-MOKA	sim
	$z_S = 0.5$		$z_S = 1$	
strong	33.04 %	54.57 %	23.57 %	36.23 %
moderate	38.66 %	33.94 %	39.92 %	40.67 %
weak	20.43 %	10.89 %	20.89 %	13.04 %
	$z_S = 2$		$z_S = 4$	
strong	14.13 %	14.99 %	12.20 %	12.94 %
moderate	26.56 %	31.98 %	23.95 %	28.73 %
weak	32.62 %	28.94 %	34.75 %	29.70 %

Table 4.5: List of the percentages of pixels in the cross-correlation coefficient matrices derived from WL-MOKA and from the simulation, of each kind of correlation among the scales for each redshift of interests, for the ΛCDM-HS8 sample.

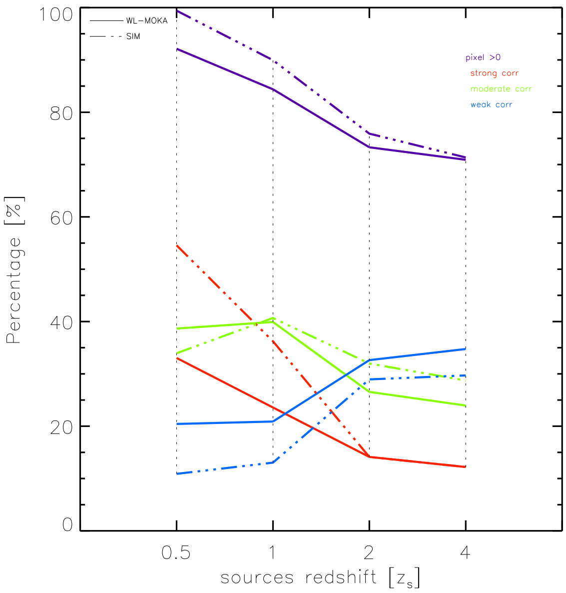

Figure 4.40: Trends of percentages of the pixels in the cross-correlation coefficient matrices for each kind of correlation with respect to the source redshift. The dash-dotted lines refer to the ΛCDM-HS8 simulation, the solid lines refer to WL-MOKA; the violet lines refer to the percentage of correlated pixels, the red lines identify strong correlation, the green lines refer to moderate correlations and the blue lines are for the weak correlations.

As in the case of the ΛCDM sample, the cross-correlation coefficient matrices are in general diagonal at large scales which correspond at low ℓ, while the smaller scales, high ℓ, are strongly correlated for both the sample produced by WL-MOKA and the one coming directly from the simulation; moreover, also for this sample there is a direct relation between the ℓ where the strong correlations arise and the source redshift, the greater is z_S and the greater is the ℓ. As we said before, we would stress that the presence of the strong correlation for low redshift sources is related to the fact that we are sampling the inner region of the halos, and so the measure is dominated by the intrinsic variance of the halos itself; while the fact that for at high redshift the strong correlation is still present is due to the smallness of the sample.

Epilogue

This thesis has the goal to understand how and how much the the matter distribution of the large scale structure infers on the weak lensing of the LSS itself. We decided to simulate the LSS by treating it as an ensemble of clumps of dark matter described by a given density profile and distributed in space in a cosmologically consistent way. This approach follows the halo-model (Cooray and Sheth, 2002), for which the properties of the structures on large scales can be described by the overposition of the gravitational fields of single halos.

To achieve this aim we developed WL-MOKA, a fast semi-analytical code based on MOKA (Giocoli et al., 2012a). This code is able, with a very simple recipe, to derive the convergence maps of mock light cones filled with halos.
To test the limits and fine tune the parameters of our code, we constructed light cones with a field of view of 25 deg^2 and we populated them with the dark matter halos catalogues provided by the ΛCDM simulation taken from the CoDECS suite performed by Baldi (2012b), and we compared our results with the simulation itself. We focused on the distribution of matter inside and outside the virial radius of the halos, on their dimensions and on the possible effects of these two parameters on the probability distribution function and the power spectrum of the convergence.
Once we found the best match with simulation results, we proceeded in our analysis by considering a sample of 25 different catalogues of the flat ΛCDM cosmology simulation of the CoDECS suite. We calculated the covariance matrices and the cross correlation coefficient matrices of the power spectrum, and we compared them with the simulation results again.
We also considered a second simulation, called ΛCDM-HS8, with the same cosmological parameters and a different value of σ_8 in order to make our consideration more solid.

Our results and critical points can be summarized as follows.

(i) We decided to not to follow what was prescribed in Bartelmann (1996) in the procedure to calculate the surface density of a halo, and we integrate the density profile up to the height of the halo itself on the plane. This choice allows us to be more precise in the description of the halos and their environment and to not consider the contribution of extra mass out of the halo.

(ii) The convergence fields extracted directly from the simulation show the presence of the filamentary structures among the clusters and seem to be more homogeneous than the convergence field produced by our codes, for all the considered source redshifts. In any case, in both cases the same structures are recognisable.

(iii) The PDFs from our code are compatible with the ones derived from the simulation. At higher sources redshifts our PDFs are broader than those coming from the simulation, this difference is due to the higher resolution of WL-MOKA, that is able to sample the inner regions of the halos and then higher value of κ.

(iv) We performed several light cones in which the halos are extended from 1 up to 8 virial radii. We find that the best match with the simulation results in the range $10^2 < \ell < 10^4$ is with light cones populated with halos truncated at 5 virial radii and modeled with the NFW density profile. For minor radii the power spectra extracted is underestimated, predicting a lack of power in the considered range of ℓ, while for bigger radii there is an excess.

(v) We also considered halos with a density profile outside the virial radius described by a power law density profile $\rho_{out} \propto r^{-\beta}$ and in which we variated the slope, $\beta = [3.5, 4, 5, 6]$. We observed that this kind of halos produce always a lack of power at $\ell < 10^4$ respect to the halos with a NFW density profile.

(vi) Our power spectra have a different behavior for $\ell > 10^4$ with respect to the spectra obtained with the simulation. This is explained by the fact

N-body simulation, due to the finite number of particle, are affected by the particle shot-noise, while our code is not.

(vii) The lack of power predicted by our power spectra for all the source redshifts at $\ell < 10^2$ is due to our limited field of view; in fact, the limit of our maps is $\ell \approx 72$.

(viii) The covariance matrices calculated starting from our power spectra sample show that at different redshifts the percentage of scales in direct correlation is between $\approx 78 - 90$ %, while in the case of the simulation sample the percentage is slightly higher.

(ix) In our cross-correlation coefficient matrices, the percentage of strongly correlated scales are similar with the values coming from the cones filled with particles with the simulation, for both the source redshifts $z_s = [2, 4]$, while in the other two cases the values are quite low with respect to the the simulation. The correlation in the case of light cones produced with the simulation arises for for slightly bigger scales (lower ℓ) than in the case of our cones. The existence in any case of strong correlation at very small scales is due to limitation of the sample, so the intrinsic variance of the halos dominates also at higher redshifts.

We can conclude that WL-MOKA, at a first analysis, is a very fast and user friendly tool for weak lensing study of the LSS, that can be generalized to every cosmological context. It has a very good behavior in the range of $10^2 < \ell < 10^4$ in simulating the LSS. Our future perspectives are to enhance the skills of the code, in order to overcome the critical point previously underlined.

- We plan to extend the range of validity of WL-MOKA, by creating mock light cones with a bigger aperture angle.
- We have to analyse bigger samples in order to avoid the arising of strong correlation at small scales.
- We can add more ingredients to our recipe, as the error on the estimate of the measure in the background galaxies or increase the complexity of the halo to make a model that is more realistic.

Bibliography

Allen, S. W., Schmidt, R. W., and Fabian, A. C.: 2002, *MNRAS* **334**, L11

Bacon, D. J., Refregier, A. R., and Ellis, R. S.: 2000, *MNRAS* **318**, 625

Bahcall, J. N. and Sarazin, C. L.: 1977, *ApJ* **213**, L99

Baldi, M.: 2012a, *MNRAS* **420**, 430

Baldi, M.: 2012b, *MNRAS* **422**, 1028

Bartelmann, M.: 1996, *A&A* **313**, 697

Bartelmann, M. and Schneider, P.: 2001, *Phys. Rep.* **340**, 291

Becker, M. R., Troxel, M. A., MacCrann, N., Krause, E., Eifler, T. F., Friedrich, O., Nicola, A., Refregier, A., Amara, A., Bacon, D., Bernstein, G. M., Bonnett, C., Bridle, S. L., Busha, M. T., Chang, C., Dodelson, S., Erickson, B., Evrard, A. E., Frieman, J., Gaztanaga, E., Gruen, D., Hartley, W., Jain, B., Jarvis, M., Kacprzak, T., Kirk, D., Kravtsov, A., Leistedt, B., Peiris, H. V., Rykoff, E. S., Sabiu, C., Sánchez, C., Seo, H., Sheldon, E., Wechsler, R. H., Zuntz, J., Abbott, T., Abdalla, F. B., Allam, S., Armstrong, R., Banerji, M., Bauer, A. H., Benoit-Lévy, A., Bertin, E., Brooks, D., Buckley-Geer, E., Burke, D. L., Capozzi, D., Carnero Rosell, A., Carrasco Kind, M., Carretero, J., Castander, F. J., Crocce, M., Cunha, C. E., D'Andrea, C. B., da Costa, L. N., DePoy, D. L., Desai, S., Diehl, H. T., Dietrich, J. P., Doel, P., Fausti Neto, A., Fernandez, E., Finley, D. A., Flaugher, B., Fosalba, P., Gerdes, D. W., Gruendl, R. A., Gutierrez, G., Honscheid, K., James, D. J., Kuehn, K., Kuropatkin, N., Lahav, O., Li, T. S., Lima, M., Maia, M. A. G., March, M., Martini, P., Melchior, P., Miller, C. J., Miquel, R., Mohr, J. J., Nichol, R. C., Nord, B., Ogando, R., Plazas, A. A., Reil, K., Romer, A. K., Roodman, A., Sako, M., Sanchez, E., Scarpine, V., Schubnell, M., Sevilla-Noarbe, I., Smith, R. C., Soares-Santos, M., Sobreira, F., Suchyta, E., Swanson, M. E. C., Tarle, G., Thaler, J., Thomas, D., Vikram, V., Walker, A. R., and Dark Energy Survey Collaboration: 2016, *Phys. Rev.* **94(2)**, 022002

Bernardeau, F., Colombi, S., Gaztañaga, E., and Scoccimarro, R.: 2002, *Phys. Rep.* **367**, 1

Bernardeau, F. and Valageas, P.: 2000, *A&A* **364**, 1

Bernardeau, F., van Waerbeke, L., and Mellier, Y.: 1997, *A&A* **322**, 1

Blake, C., Joudaki, S., Heymans, C., Choi, A., Erben, T., Harnois-Deraps, J., Hildebrandt, H., Joachimi, B., Nakajima, R., van Waerbeke, L., and Viola, M.: 2016, *MNRAS* **456**, 2806

Blumenthal, G. R., Faber, S. M., Flores, R., and Primack, J. R.: 1986, *ApJ* **301**, 27

Bozza, V.: 2010, *General Relativity and Gravitation* **42**, 2269

Bozza, V., Capozziello, S., Iovane, G., and Scarpetta, G.: 2001, *General Relativity and Gravitation* **33**, 1535

Brax, P. H. and Martin, J.: 1999, *Physics Letters B* **468**, 40

Bullock, J. S., Kolatt, T. S., Sigad, Y., Somerville, R. S., Kravtsov, A. V., Klypin, A. A., Primack, J. R., and Dekel, A.: 2001, *MNRAS* **321**, 559

Burkert, A.: 1993, *A&A* **278**, 23

Choi, J.-H., Weinberg, M. D., and Katz, N.: 2009, *MNRAS* **400**, 1247

Clowe, D., Bradač, M., Gonzalez, A. H., Markevitch, M., Randall, S. W., Jones, C., and Zaritsky, D.: 2006, *ApJ* **648**, L109

Clowe, D., Gonzalez, A., and Markevitch, M.: 2004, *ApJ* **604**, 596

Coil, A. L.: 2013, *The Large-Scale Structure of the Universe*, p. 387

Coles, P. and Lucchin, F.: 2002, *Cosmology: the origin and evolution of cosmic structure*, John Wiley & sons, ltd

Cooray, A. and Sheth, R.: 2002, *Phys. Rep.* **372**, 1

Davis, M., Efstathiou, G., Frenk, C. S., and White, S. D. M.: 1985, *ApJ* **292**, 371

de Jong, J. T. A., Verdoes Kleijn, G. A., Kuijken, K. H., and Valentijn, E. A.: 2013, *Experimental Astronomy* **35**, 25

de Vaucouleurs, G.: 1948, *Annales d'Astrophysique* **11**, 247

Einasto, J.: 2012, *International Journal of Modern Physics Conference Series* **12**, 100

Ellis, R. S.: 2010, *Philosophical Transactions of the Royal Society of London Series A* **368**, 967

Flaugher, B., Diehl, H. T., Honscheid, K., Abbott, T. M. C., Alvarez, O., Angstadt, R., Annis, J. T., Antonik, M., Ballester, O., Beaufore, L., Bernstein, G. M., Bernstein, R. A., Bigelow, B., Bonati, M., Boprie, D., Brooks, D., Buckley-Geer, E. J., Campa, J., Cardiel-Sas, L., Castander, F. J., Castilla, J., Cease, H., Cela-Ruiz, J. M., Chappa, S., Chi, E., Cooper, C., da Costa, L. N., Dede, E., Derylo, G., DePoy, D. L., de Vicente, J., Doel, P., Drlica-Wagner, A., Eiting, J., Elliott, A. E., Emes, J., Estrada, J., Fausti Neto, A., Finley, D. A., Flores, R., Frieman, J., Gerdes, D., Gladders, M. D., Gregory, B., Gutierrez, G. R., Hao, J., Holland, S. E., Holm, S., Huffman, D., Jackson, C., James, D. J., Jonas, M., Karcher, A., Karliner, I., Kent, S., Kessler, R., Kozlovsky, M., Kron, R. G., Kubik, D., Kuehn, K., Kuhlmann, S., Kuk, K., Lahav, O., Lathrop, A., Lee, J., Levi, M. E., Lewis, P., Li, T. S., Mandrichenko, I., Marshall, J. L., Martinez, G., Merritt, K. W., Miquel, R., Muñoz, F., Neilsen, E. H., Nichol, R. C., Nord, B., Ogando, R., Olsen, J., Palaio, N., Patton, K., Peoples, J., Plazas, A. A., Rauch, J., Reil, K., Rheault, J.-P., Roe, N. A., Rogers, H., Roodman, A., Sanchez, E., Scarpine, V., Schindler, R. H., Schmidt, R., Schmitt, R., Schubnell, M., Schultz, K., Schurter, P., Scott, L., Serrano, S., Shaw, T. M., Smith, R. C., Soares-Santos, M., Stefanik, A., Stuermer, W., Suchyta, E., Sypniewski, A., Tarle, G., Thaler, J., Tighe, R., Tran, C., Tucker, D., Walker, A. R., Wang, G., Watson, M., Weaverdyck, C., Wester, W., Woods, R., Yanny, B., and DES Collaboration: 2015, *AJ* **150**, 150

Fort, B. and Mellier, Y.: 1994, *A&A Rev.* **5**, 239

Freedman, W. L., Madore, B. F., Gibson, B. K., Ferrarese, L., Kelson, D. D., Sakai, S., Mould, J. R., Kennicutt, Jr., R. C., Ford, H. C., Graham, J. A., Huchra, J. P., Hughes, S. M. G., Illingworth, G. D., Macri, L. M., and Stetson, P. B.: 2001, *ApJ* **553**, 47

Freedman, W. L. and Turner, M. S.: 2003, *Reviews of Modern Physics* **75**, 1433

Gao, L., White, S. D. M., Jenkins, A., Stoehr, F., and Springel, V.: 2004, *MNRAS* **355**, 819

Gaudi, B. S.: 2010, *Microlensing by Exoplanets*, pp 79–110

Geller, M. J., Diaferio, A., Rines, K. J., and Serra, A. L.: 2013, *ApJ* **764**, 58

Ghigna, S., Moore, B., Governato, F., Lake, G., Quinn, T., and Stadel, J.: 1999, in G. Giuricin, M. Mezzetti, and P. Salucci (eds.), *Observational Cosmology: The Development of Galaxy Systems*, Vol. 176 of *Astronomical Society of the Pacific Conference Series*, p. 140

Giocoli, C., Bonamigo, M., Limousin, M., Meneghetti, M., Moscardini, L., Angulo, R. E., Despali, G., and Jullo, E.: 2016a, *MNRAS* **462**, 167

Giocoli, C., Jullo, E., Metcalf, R. B., de la Torre, S., Yepes, G., Prada, F., Comparat, J., Goettlober, S., Kyplin, A., Kneib, J.-P., Petkova, M., Shan, H., and Tessore, N.: 2015a, *ArXiv e-prints*

Giocoli, C., Jullo, E., Metcalf, R. B., de la Torre, S., Yepes, G., Prada, F., Comparat, J., Göttlober, S., Kyplin, A., Kneib, J.-P., Petkova, M., Shan, H. Y., and Tessore, N.: 2016b, *MNRAS* **461**, 209

Giocoli, C., Meneghetti, M., Bartelmann, M., Moscardini, L., and Boldrin, M.: 2012a, *MNRAS* **421**, 3343

Giocoli, C., Meneghetti, M., Ettori, S., and Moscardini, L.: 2012b, *MNRAS* **426**, 1558

Giocoli, C., Meneghetti, M., Metcalf, R. B., Ettori, S., and Moscardini, L.: 2014, *MNRAS* **440**, 1899

Giocoli, C., Metcalf, R. B., Baldi, M., Meneghetti, M., Moscardini, L., and Petkova, M.: 2015b, *MNRAS* **452**, 2757

Giocoli, C., Tormen, G., Sheth, R. K., and van den Bosch, F. C.: 2010, *MNRAS* **404**, 502

Hamana, T., Oguri, M., Shirasaki, M., and Sato, M.: 2012, *MNRAS* **425**, 2287

Hamana, T., Sakurai, J., Koike, M., and Miller, L.: 2015, *PASJ* **67**, 34

Harnois-Déraps, J., Vafaei, S., and Van Waerbeke, L.: 2012, *MNRAS* **426**, 1262

Harnois-Déraps, J. and van Waerbeke, L.: 2015, *MNRAS* **450**, 2857

Hattori, M., Kneib, J., and Makino, N.: 1999, *Progress of Theoretical Physics Supplement* **133**, 1

Hernquist, L.: 1990, *ApJ* **356**, 359

Hoekstra, H., Bartelmann, M., Dahle, H., Israel, H., Limousin, M., and Meneghetti, M.: 2013, *ssr*

Hoekstra, H., Franx, M., and Kuijken, K.: 2000, *ApJ* **532**, 88

Hoekstra, H., Hartlap, J., Hilbert, S., and van Uitert, E.: 2011, *MNRAS* **412**, 2095

Hu, W.: 1999, *ApJ* **522**, L21

Hung, C.-L., Casey, C. M., Chiang, Y.-K., Capak, P., Cowley, M. J., Darvish, B., Kacprzak, G. G., Kovac, K., Lilly, S. J., Nanayakkara, T., Spitler, L. R., Tran, K.-V. H., and Yuan, T.: 2016, *ArXiv e-prints*

Jaffe, W.: 1983, *MNRAS* **202**, 995

Jain, B., Seljak, U., and White, S.: 2000, *ApJ* **530**, 547

Jarosik, N., Bennett, C. L., Dunkley, J., Gold, B., Greason, M. R., Halpern, M., Hill, R. S., Hinshaw, G., Kogut, A., Komatsu, E., Larson, D., Limon, M., Meyer, S. S., Nolta, M. R., Odegard, N., Page, L., Smith, K. M., Spergel, D. N., Tucker, G. S., Weiland, J. L., Wollack, E., and Wright, E. L.: 2011, *ApJS* **192**, 14

Jing, Y. P. and Suto, Y.: 2002, *ApJ* **574**, 538

Kayo, I., Taruya, A., and Suto, Y.: 2001, *ApJ* **561**, 22

Keeton, C. R.: 2001, *ApJ* **561**, 46

Keeton, C. R.: 2003, *ApJ* **584**, 664

Klimov, Y. G.: 1963, *Soviet Physics Doklady* **8**, 431

Kneib, J.-P. and Natarajan, P.: 2011, *A&A Rev.* **19**, 47

Kochanek, C. S.: 2006, in G. Meylan, P. Jetzer, P. North, P. Schneider, C. S. Kochanek, and J. Wambsganss (eds.), *Saas-Fee Advanced Course 33: Gravitational Lensing: Strong, Weak and Micro*, pp 91–268

Komatsu, E., Dunkley, J., Nolta, M. R., Bennett, C. L., Gold, B., Hinshaw, G., Jarosik, N., Larson, D., Limon, M., Page, L., Spergel, D. N., Halpern, M., Hill, R. S., Kogut, A., Meyer, S. S., Tucker, G. S., Weiland, J. L., Wollack, E., and Wright, E. L.: 2009, *ApJS* **180**, 330

Kormendy, J.: 1977, *ApJ* **218**, 333

Kuijken, K., Heymans, C., Hildebrandt, H., Nakajima, R., Erben, T., de Jong, J. T. A., Viola, M., Choi, A., Hoekstra, H., Miller, L., van Uitert, E., Amon, A., Blake, C., Brouwer, M., Buddendiek, A., Conti, I. F., Eriksen, M., Grado, A., Harnois-Déraps, J., Helmich, E., Herbonnet, R., Irisarri, N., Kitching, T., Klaes, D., La Barbera, F., Napolitano, N., Radovich, M., Schneider, P., Sifón, C., Sikkema, G., Simon, P., Tudorica, A., Valentijn, E., Verdoes Kleijn, G., and van Waerbeke, L.: 2015, *MNRAS* **454**, 3500

Kunz, M., Nesseris, S., and Sawicki, I.: 2016, *ArXiv e-prints*

Laureijs, R.: 2009, *ArXiv e-prints*

Laureijs, R., Amiaux, J., Arduini, S., Auguères, J. ., Brinchmann, J., Cole, R., Cropper, M., Dabin, C., Duvet, L., Ealet, A., and et al.: 2011, *ArXiv e-prints*

Lewis, A., Challinor, A., and Lasenby, A.: 2000, *ApJ* **538**, 473

Liebes, S.: 1964, *Physical Review* **133**, 835

Limber, D. N.: 1953, *ApJ* **117**, 134

Lin, C.-A. and Kilbinger, M.: 2015, *A&A* **576**, A24

LSST Science Collaboration, Abell, P. A., Allison, J., Anderson, S. F., Andrew, J. R., Angel, J. R. P., Armus, L., Arnett, D., Asztalos, S. J., Axelrod, T. S., and et al.: 2009, *ArXiv e-prints*

Markevitch, M.: 2006, in A. Wilson (ed.), *The X-ray Universe 2005*, Vol. 604 of *ESA Special Publication*, p. 723

Massey, R., Kitching, T., and Richard, J.: 2010, *Reports on Progress in Physics* **73(8)**, 086901

Mellier, Y.: 1999, *ARA&A* **37**, 127

Meneghetti, M., Bartelmann, M., and Moscardini, L.: 2003, *MNRAS* **346**, 67

Metcalf, R. B. and Petkova, M.: 2014, *MNRAS* **445**, 1942

Munari, E., Biviano, A., Borgani, S., Murante, G., and Fabjan, D.: 2013, *MNRAS* **430**, 2638

Munshi, D. and Jain, B.: 2000, *MNRAS* **318**, 109

Narayan, R. and Bartelmann, M.: 1996, *ArXiv Astrophysics e-prints*

Navarro, J. F., Frenk, C. S., and White, S. D. M.: 1996, *ApJ* **462**, 563

Neto, A. F., Gao, L., Bett, P., Cole, S., Navarro, J. F., Frenk, C. S., White, S. D. M., Springel, V., and Jenkins, A.: 2007, *MNRAS* **381**, 1450

Okabe, N., Takada, M., Umetsu, K., Futamase, T., and Smith, G. P.: 2010, *PASJ* **62**, 811

Petkova, M., Metcalf, R. B., and Giocoli, C.: 2014, *MNRAS* **445**, 1954

Planck Collaboration, Ade, P. A. R., Aghanim, N., Armitage-Caplan, C., Arnaud, M., Ashdown, M., Atrio-Barandela, F., Aumont, J., Baccigalupi, C., Banday, A. J., and et al.: 2014, *A&A* **571**, A17

Postman, M., Lauer, T. R., Donahue, M., Graves, G., Coe, D., Moustakas, J., Koekemoer, A., Bradley, L., Ford, H. C., Grillo, C., Zitrin, A., Lemze, D., Broadhurst, T., Moustakas, L., Ascaso, B., Medezinski, E., and Kelson, D.: 2012, *ApJ* **756**, 159

Radovich, M., Puddu, E., Romano, A., Grado, A., and Getman, F.: 2008, *A&A* **487**, 55

Reese, E. D.: 2004, *Measuring and Modeling the Universe* p. 138

Refregier, A.: 2003, *ARA&A* **41**, 645

Refregier, A., Amara, A., Kitching, T. D., Rassat, A., Scaramella, R., Weller, J., and Euclid Imaging Consortium, f. t.: 2010, *ArXiv e-prints*

Refsdal, S.: 1964, *MNRAS* **128**, 307

Riess, A. G., Filippenko, A. V., Challis, P., Clocchiatti, A., Diercks, A., Garnavich, P. M., Gilliland, R. L., Hogan, C. J., Jha, S., Kirshner, R. P., Leibundgut, B., Phillips, M. M., Reiss, D., Schmidt, B. P., Schommer, R. A., Smith, R. C., Spyromilio, J., Stubbs, C., Suntzeff, N. B., and Tonry, J.: 1998, *AJ* **116**, 1009

Romano, A., Fu, L., Giordano, F., Maoli, R., Martini, P., Radovich, M., Scaramella, R., Antonuccio-Delogu, V., Donnarumma, A., Ettori, S., Kuijken, K., Meneghetti, M., Moscardini, L., Paulin-Henriksson, S., Giallongo, E., Ragazzoni, R., Baruffolo, A., Dipaola, A., Diolaiti, E., Farinato, J., Fontana, A., Gallozzi, S., Grazian, A., Hill, J., Pedichini, F., Speziali, R., Smareglia, R., and Testa, V.: 2010, *A&A* **514**, A88

Roncarelli, M., Cappelluti, N., Borgani, S., Branchini, E., and Moscardini, L.: 2012, *ArXiv e-prints*

Salvador-Solé, E., Serra, S., and Manrique, A.: 2011, *ArXiv e-prints*

Sarazin, C. L.: 1986, *Reviews of Modern Physics* **58**, 1

Schechter, P.: 1976, *ApJ* **203**, 297

Schmidt, F.: 2016, *Phys. Rev.* **93(6)**, 063512

Schneider, P.: 2005, *ArXiv Astrophysics e-prints*

Seitz, C. and Schneider, P.: 1997, *A&A* **318**, 687

Seljak, U.: 1996, *ApJ* **463**, 1

Shapiro, I. I.: 1964, *Physical Review Letters* **13**, 789

Sheth, R. K. and Tormen, G.: 2002, *MNRAS* **329**, 61

Springel, V.: 2005, *MNRAS* **364**, 1105

Stoehr, F., White, S. D. M., Springel, V., Tormen, G., and Yoshida, N.: 2003, *MNRAS* **345**, 1313

Sunyaev, R. A. and Zeldovich, I. B.: 1980, *ARA&A* **18**, 537

Takada, M. and Jain, B.: 2002, *MNRAS* **337**, 875

Takahashi, R., Oguri, M., Sato, M., and Hamana, T.: 2011, *ApJ* **742**, 15

Treu, T.: 2010, *ARA&A* **48**, 87

Turner, M. S.: 1997, *ArXiv Astrophysics e-prints*

Umetsu, K.: 2010, *ArXiv e-prints*

Valageas, P.: 2000, *A&A* **356**, 771

Vale, C. and White, M.: 2003, *ApJ* **592**, 699

Virbhadra, K. S. and Ellis, G. F. R.: 2000, *Phys. Rev.* **62(8)**, 084003

Wambsganss, J.: 2006, *ArXiv Astrophysics e-prints*

Wang, L., Li, C., Kauffmann, G., and De Lucia, G.: 2006, *MNRAS* **371**, 537

Weinberg, S.: 2008, *Cosmology*, Oxford University Press

Wetterich, C.: 1988, *Nuclear Physics B* **302**, 668

Wright, C. O. and Brainerd, T. G.: 2000, *ApJ* **534**, 34

Wyrzykowski, L., Skowron, J., Kozłowski, S., Udalski, A., Szymański, M. K., Kubiak, M., Pietrzyński, G., Soszyński, I., Szewczyk, O., Ulaczyk, K., Poleski, R., and Tisserand, P.: 2011, *MNRAS* **416**, 2949

Zhao, D. H., Jing, Y. P., Mo, H. J., and Börner, G.: 2009, *ApJ* **707**, 354

Zwicky, F.: 1937, *ApJ* **86**, 217

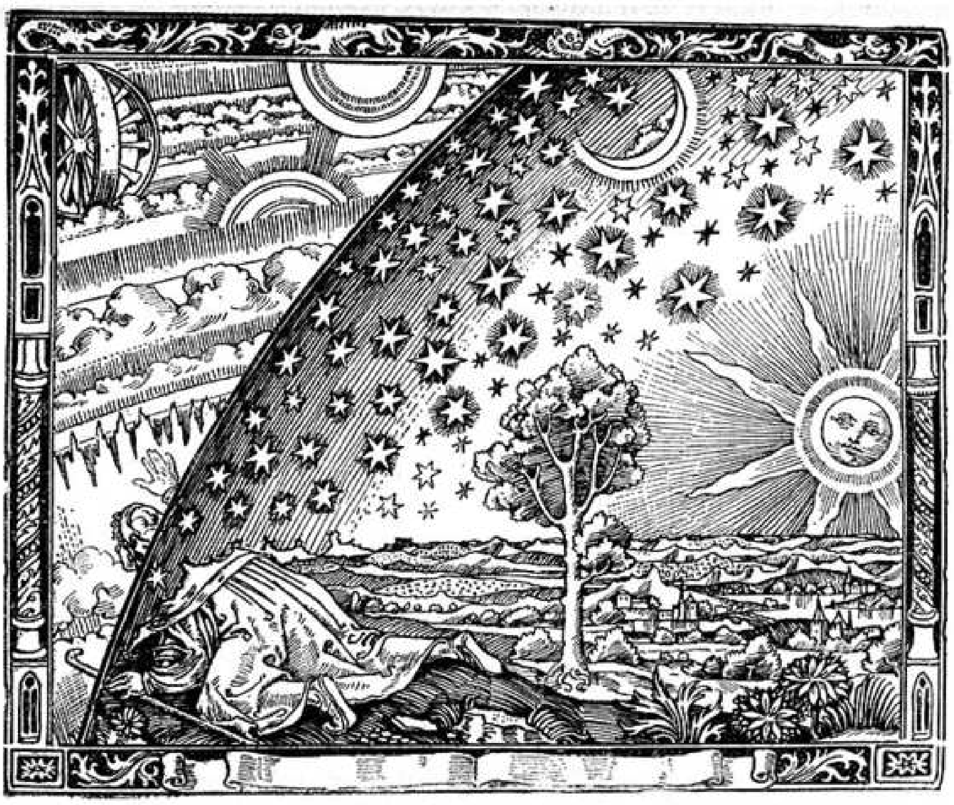

Un missionnaire du moyen âge raconte qu'il avait trouvé le point où le ciel et la Terre se touchent...

Universum, Camille Flammarium, Parigi 1888.